國立臺灣大學理學院地質科學所

博士論文

Department of Geosciences

College of Science

National Taiwan University

Ph.D. Dissertation

地質作用對台灣西南海域地熱構造的影響

Geological Processes Related to Seafloor Thermal Structures offshore SW Taiwan

陳麗雯

Liwen Chen

指導教授：盧佳遇 博士, 戚務正 博士、

Advisors: Chia-Yu, Lu, Ph.D., Wu-Cheng Chi Ph.D.

中華民國 103 年 6 月

Jun 2014

國立臺灣大學（碩）博士學位論文
口試委員會審定書

地質作用對台灣西南海域地熱構造的影響
Geological Processes Related to Seafloor Thermal Structures Offshore SW Taiwan

本論文係陳麗雯君（學號 D98224005）在國立臺灣大學地質科學系暨研究所完成之博士學位論文，於民國 103 年 5 月 12 日承下列考試委員審查通過及口試及格，特此證明

口試委員：盧佳遇　戚務正

（指導教授）

胡植慶　李元希

劉家瑄　王詠均

致謝

意外的博士生涯，在種種忙碌與壓力交織中悄然落幕。不是最優秀的人我，僅憑藉著小草般的韌性、以及微薄的幸運跌跌撞撞到今天，萬分感激我身後那些堅強的後盾們給我的一切，讓我能在跌入谷底時能有力量再支持下去。

我人生轉捩點，無非是踏入中研院認識我的老闆兼老師兼戰友－戚務正博士，謝謝您引領我、成就我，到一個我從沒想過的境界，just like the song sings: You raise me up… to more than I can be，謝謝您總能激發出我的潛力，尤其在許多 deadline 在即的時候；或許我始終粗心大意，但如果有一天，我可以成為更好的人，那麼您的功勞影響必不可沒。謝謝與我認識十年，在我碩士時期就為我埋下地物種子的劉家瑄教授，是您給我機會進入這個領域，在您的庇護下，有幸能夠成為您大家庭中的一份子，長時間以來種種的支持以及協助，我銘感在心；謝謝親愛的盧爺，雖遲遲缺乏機會向您認真學習您的阿達智慧，但跟您的緣份就彷彿是一種默契，深深地感謝您對我的默默付出與珍惜；謝謝胡植慶老師，在每次的交相詰問中，您總是用心備至，雖愧於達不到您的要求，但您的認真態度著實烙印我心，提醒我無論在什麼階段，都要學習您不斷地追求上進。

此外，在學業及工作忙碌之際，家人一直是我最甜蜜的負荷，為了你們我不敢安逸怠惰太多；謝謝你們在我最倦、最累時，始終守在那裡默默為我加油，哪怕我常忘了帶笑容回家。謝謝我親愛的 Hanny、HNY & 老朋友、Geothermal & SEL 同學、IES 同事、家教 families，沒有你們那些有形、無形的鼓勵及幫助，不會有今天的我，謝謝你們總是包容如此不完美的我、給我力量、為我打氣，除了感激還是感激，更謝謝 FB 讓我可以默默地關注你們的一動一舉，化千里於咫尺相依。

最後，謝謝過去的我自己，謝謝你沒有放棄，給現在的我一個新的成長契機。

摘要

地質作用之於熱流模式的影響是天然氣水合物能源探勘中相當重要的研究。但海域相較於陸地更難直接測量到地熱資料，因此我們將過去幾年台灣西南海域量測到的海床地熱資訊，結合震測調查顯示所得到的密集的海底仿擬反射(BSR)分布，運用天然氣水合物本身的物理特性，取得海床下數百米深的溫度場作為本研究之重要參考數據。本研究中，我們首先建構起兩種熱流模擬的相關技術，讓我們應用在區域性的溫度場上，進行一維流體速率以及二維剖面上、三維空間上溫度場差異的分析，以瞭解其與各項地質作用之間的關聯性。

首先，我們利用 BSR 深度轉換所得的溫度場，以及量測所得的海床溫度作佩克萊數（Péclet numbers） 的分析而推導出區域性的一維流體移棲模式。我們發現到研究區域內的垂直向上流體速率範圍為每年 6 到 43 公分，當中更不乏許多天然氣水合物的精查重點區域。本項研究的結果發現流體移棲速率由非主動板塊區域逐漸向主動板塊區域漸增，可能與增積岩體的脫水現象有關；而沿著海溝向北更可發現流速在前緣逆衝褶皺附上非主動大陸板塊時達最高。此外，考量到地形效應可能會對溫度場量測所造成的影響，我們採用與海床地形變化有關的BSR溫度場，去扣除我們熱傳導模型（finite element code; Pecube）所取得的差異溫度場，作為討論分析地質作用之於溫度場變化之依據。

因此，我們依照研究的結果提出了幾個可能影響差異溫度場分布的地質作用來討論：（1）我們發現到位於上部斜坡之下枋寮峽谷處的泥貫入體構造，較兩翼

的沉積構造高出 38%的熱效應；（2）相對地，在下部斜坡區的永安逆斷層處，我們認為其具有斷斷續續的熱流自斷層面向上供給影響區域溫度場；（3）而前緣海脊處，我們則是觀察到增積岩體前緣處的許多斷層裂隙處以及趾部受壓熱流上升的現象；（4）我們還提出了關於澎湖峽谷上游區的塊體滑移構造，其對於上坡處溫度場的影響是加溫；而對於下坡處則是降溫的解釋模型；（5）除此之外，我們發現在非主動板塊處的福爾摩沙海脊，擁有冷水吸入脊部加壓、以及脊部有通道向上洩壓的冷泉循環，並加以平行脊部方向的強烈擴散作用，方才導致今日我們所觀察到的許多降溫現象，或是冷泉生物存在的證明。

我們的研究乃為初次結合震測、地熱作為區域性的熱構造做模擬分析，將來有待於鑽井之後取得更精確的物理參數，讓我們原本定性的趨勢性研究成果，有機會可以推廣到定量而取得甲烷通量等十分重要的數據，藉時將有助於我們台灣西南海域的能源探勘研究。

關鍵字：地質作用、熱效應、地溫梯度、佩克萊數（Péclet numbers）、Pecube、海底仿擬反射、台灣西南海域

Abstract

Geological processes on thermal patterns are important for understanding the energy potential for hydrocarbon exploration; however, thermal patterns below the seafloor are always difficult to derive. So we combined the geophysical in-situ thermal measurements and the wide spreading bottom-simulating-reflectors (BSR; bottom of the gas hydrate stability zone identified from the seismic data) collected recent years, to model the temperature fields beneath the seafloor. Using the advantage of the physical property of gas hydrates, we proposed two methods for analyzing the regional thermal patterns offshore SW Taiwan, and successfully derived several geological processes related to seafloor thermal structures according to our study results.

First, we used BSR-based geothermal gradient patterns to derive vertical fluid flow models from Péclet Number analyses. We found the regional 1-D fluid flow rates are ranging from 6 cm/yr to 43 cm/yr, including several prospect sites for gas hydrate exploration. From passive margin to active margin, the increasing of fluid flow rate might be related to more active dewatering near the toe of the trench; in the active margin, there are higher fluid flow rates when the frontal thrust climbs onto the continental slope of the passive margin in the collision zone. Then, considering about the topography effect, we used temperature discrepancies between BSR-based and modeled temperatures, which are derived from the finite element code – Pecube, to

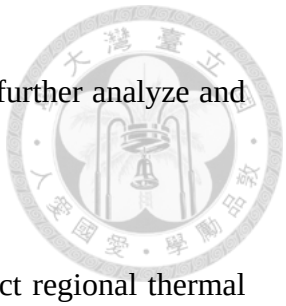

reflect the regional cooling and heating effects. Therefore we could further analyze and compare the regional geological processes based on our study results.

Finally, we proposed several geological processes that can affect regional thermal patterns: (1) From studying the 3-D cube in lower Fangliao Canyon of the upper slope domain, we discovered the regional heating effect from the diapir was reduced 38 % by recent sedimentation; (2) relatively, we found intermittent upward fluid migrations along the fault planes brought the heating effects in Yung-An Ridge of the lower slope domain; (3) as well as in Frontal Ridge, we found possible extensive fluid migration from the faulting pathways to cause heating effects at the toe of the accretionary wedge. (4) Related to the MTD (mass-transport deposits) effect occurred in upper reach of the Penghu Canyon, it caused the heating and cooling effects at the uphill and downhill respectively. (5) Beside, in the canyon incision region of Formosa Ridge, we found the cold seawater had been laterally siphoned into the ridge in the traverse direction, and diffused along the ridge strike to disturb the temperature fields. In this study, our contribution is developing the simulation methods for better using our current data to analyze thermal structures; in the future, we could improve our simulation results to get more quantifiable flux information for the energy research offshore SW Taiwan.

Keywords: geological process, thermal effects, geothermal gradients, Péclet Numbers, Pecube, bottom simulating reflector, offshore southwestern Taiwan.

Table of Contents

List of Figures

List of Tables

Chapter 1: Introduction

Fluid flow affects heat transport processes and perturbs crustal thermal structures. These thermal perturbations can be used to study fluid migration parameters, which are important geophysical parameters for regional tectonics, thermal energy research, and hydrocarbon reservoir simulations. Offshore southwestern (SW) Taiwan, heat flow data can be obtained by thermal probe measurements (Shyu et al., 2006) in very shallow sediments (< 6 m), however, it's difficult to infer temperature fields and fluid flow patterns at depths greater than hundreds of meters under the seafloor. Drilling operations can provide ground truth information, but the costs are high. Using in-situ geothermal measurements and temperature fields derived from a Bottom Simulating Reflector (BSR), we examined conductive and convective heat transfer models, with and without the fluid involved, to study regional fluid flow patterns in shallow marine sediments.

The relationships between pressure and temperature of the gas hydrate phase change and the depth of BSR have been used to calculate geothermal gradients and heat flow (Shipley, 1979; Yamano et al., 1982; Davis et al., 1990; Hyndman and Davis, 1992; Kaul et al., 2000; Hornbach et al., 2012). There are wide-spread BSR in offshore SW Taiwan (Chi et al., 1998; Liu et al., 2006). The BSR are used to derive heat flows to

investigate crustal thermal structure (Shyu et al., 2006; Chi and Reed, 2008). In many cases, the general agreement between thermal probe data and BSR-derived heat flow suggests that it is possible to study thermal structures using BSR (Schnürle and Liu, 2011).Therefore we applied the BSR-derived temperatures to study the difference in thermal structures between active margin and passive margin in offshore SW Taiwan to better understand the petroleum system of gas hydrate. Followings are introduces of each chapter:

Chapter 2: First of all, we introduced the geological background and the regional structure features offshore SW Taiwan from previous studies. And we mentioned about how to measure the geothermal data and the properties of gas hydrates, in additional, there are several classical applications papers studying on thermal models from BSR as our references. Then we were ready for using the BSR-based temperatures as the important approaches to study the temperature fields in our target regions.

Chapter 3: Since we relied on the BSR-based temperatures very much, we have to discuss the uncertainties at the beginning of this chapter. Then we estimated the vertical fluid flow rate by analyzing the Péclet Number for regional geothermal gradient curves. For the regions in the deformation front, active and passive margin, we successfully derived the vertical fluid rates on two directions, and on several prospecting sites with longer coring sediments information.

Chapter 4: Furthermore, we used the Finite Element Method (FEM) to calculate the heat-transport equation from the software of Pecube. After simulating the conductive thermal patterns in steady state, we could derive the model temperature fields at the depth of BSR. As a result, we regarded the temperature discrepancies as the BSR-based temperature fields subtract to the model temperatures. Then we obtained some regional thermal effects from 3-D or 2-D temperature patterns in the deformation front, active and passive margin, respectively.

Chapter 5: After that, from studying the correlations between the feature structures with the temperature discrepancies from our study results, we compiled and addressed several regional geological processes which may cause these temperature perturbations, including the topographic effect, fluid flow and faulting effects, sedimentation and erosion and MTD effect, as well as the canyon incision.

Chapter 6: We summarized our contribution in modeling methods and the discoveries on regional geological processes which are affecting the thermal structures in shallow sediments offshore SW Taiwan. We then proposed some probable developments as our possible future works.

Chapter 2: Background

2.1 Background setting and prospect region in this study

Taiwan is situated on the plate boundary separating the Eurasian plate to the west from the Philippine Sea plate to the east. Offshore SW Taiwan, the Manila subduction system (20°30' N) transforms into an incipient arc-continent collision (20°30'N ~ 21°15' N), and transforms into collision system (21°15' N) (Reed et al., 1992; Hirtzel et al., 2009) (Fig. 2-1). The overriding collision/accretionary complex and the underthrusting Eurasian lithosphere is separated by the Manila trench and deformation front (Huang et al., 1997). A series of west-vergent and imbricated folds and emergent thrusts are predominant tectonic features of the accretionary wedge (Fig. 2-2). Both the convergent submarine Taiwan accretionary wedge and the passive China continental slope are dominated by ridges and submarine canyons. However, the ridges are formed by very different mechanisms. In the accretionary wedge province to the east of the deformation front, the ridges were densely formed mostly by fold-bend faults and diapirism (Liu et al., 1997; Lin et al., 2008). On the other hand, many ridges on the China continental slopes are formed by submarine erosional processes.

Previews study propose that the accretionary wedge off SW Taiwan consists of upper-slope and lower-slope domains, which are separated by a significant morphologic

break, probably related to the onset of multiple “out-of-sequence thrusts” (OOSTs) or “splay faults” (Figs. 2-1 & 2-2, Reed et al., 1992; Liu et al., 1997; Huang et al., 2004; Lin et al. 2009). In the upper slope domain, a series of mud diapirs with some gas seeps are found in the upper-slope domain near the coast of SW Taiwan (Fig. 2-1, Sun and Liu, 1993; Chiang et al., 2004; Chuang, 2006; Chen, 2013), and some of them could be traced to adjacent onshore structures in the fold-and-thrust belts which indicates the active fluid expulsion in the accretionary wedge (Yang et al., 2004). In the lower-slope domain, each fold-and-thrust corresponds to a system of an elongated submarine ridge. Lin et al. (2008) further divided the lower-slope domain into frontal and rear segments, respectively (Fig. 2-2), with frontal segment dominated by folds cored by blind thrusts, and rear segment by thrusts breaching the seafloor.

Due to Taiwan’s unique tectonic settings, it provides a unique situation to study the both tectonic settings over a short distance. This also allows us to compare patterns in hydrology in several different tectonic settings using a wide spread BSR, which we use to trace the temperature with fluid involved. So we picked several regions to compare the different temperature fields in offshore SW Taiwan.

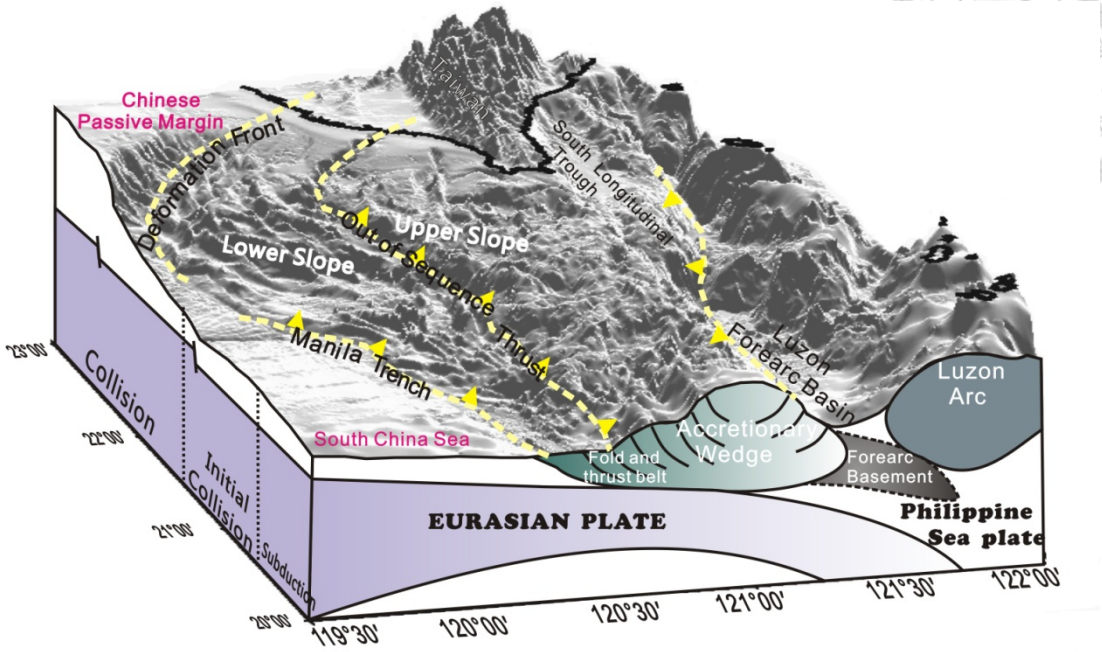

Figure 2-1 Geotectonic features offshore southwest of Taiwan. The oceanic lithosphere of the South China Sea is subducting eastward beneath the Philippine Sea plate along the Manila Trench. To the north, the thicker and more buoyant Chinese passive margin enters into to convergent boundary. From south to north, the tectonic evolution develops from subduction to collision. The western flank of the accretionary wedge contains a lower and an upper slope domain (Reed et al., 1992).

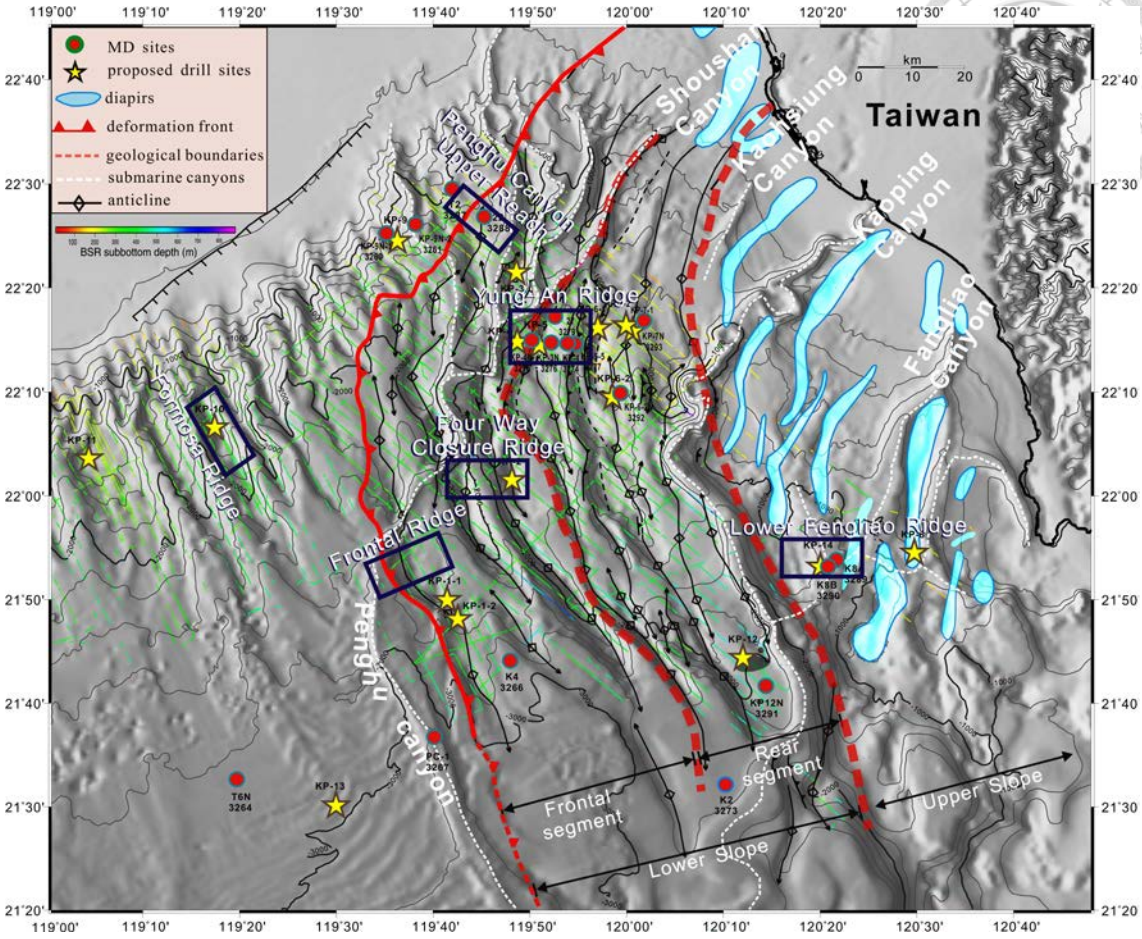

Figure 2-2 Bathymetric map and tectonic features off southwest Taiwan. Geological boundaries and structures (diapir, anticlines, and submarine canyons) and deformation front of compressive structures (barbed red line) are distinguished from the marine seismic profiles. Red circles show the site locations of the Marine Dufresne (MD) cruise in 2010, which derive much longer cores to provide lots geological evidences for studying gas hydrate. On the other hand, the yellow stars display the possible drilling sites for gas hydrate prospection in the future. Note that the blue squares are marked our simulation and study zones with more dense seismic data inside.

2.1.1 Deformation Front vicinity - Penghu Canyon & Frontal Ridge

The deformation front begins from the northern Manila Trench near 21°N and continues northward along the course of the Penghu Submarine Canyon in a nearly N-S direction north of 21°N then changes direction sharply to the northeast. And it connects to the Chungchou thrust fault or the Tainan anticline in the coast of Taiwan (Fig. 2-2, Yu et al., 2004). It divides the Penghu submarine canyon into two geological domains based of its structural and topographic characteristics: the South China Sea (SCS) continental slope domain, and the frontal segments of the accretionary prism.

Owing to the psudo-3D seismic data in the upper reach of the Penghu Submarine Canyon, there are wide distributed of BSR, paleo-channels and faulting imaged in the 2-D profiles (Fig. 2-3; Liu et al., 2006, Han et al., 2012). Besides, some geochemical and geological evidences of high methane flux and sedimentation rate are derived here (Yang, 2011; Horng, 2013). Such unique geological setting attracts us to study the evolution of the temperature fields just across the deformation front.

The frontal fold locates at the toe of the accretionary wedge and at the end of a dipping décollement surface, a major fluid conduit in accretionary wedges (Minshull and White, 1989; Shipley et al., 1994). Naturally, the frontal fold is likely to serve as a terminal structural trap for deep-seated hydrocarbons/fluids charging especially through the décollement surface. A widespread occurrence of BSR has been recognized from

seismic images beneath the frontal fold, suggesting a prevalent existence of gas hydrates in the study area (Lin et al., 2009). A few gas indicators such as enhanced reflectors, push-down reflectors, and flat-spots shown on seismic sections also indicate a substantial quantity of free gas is likely to present beneath the gas hydrate stability zone. The flat spot is a horizontal and enhanced reflector, cutting across a few dipping reflectors, interpreted as a gas–water contact (GWC) (Lin et al., 2013) (Fig. 2-4), in addition, the fluctuating range of the temperature above and below BSR is very violent (Lin et al., 2012a) (Fig. 2-5). As a result, we want to know more about the fluid patterns at the toe of the accretionary wedge.

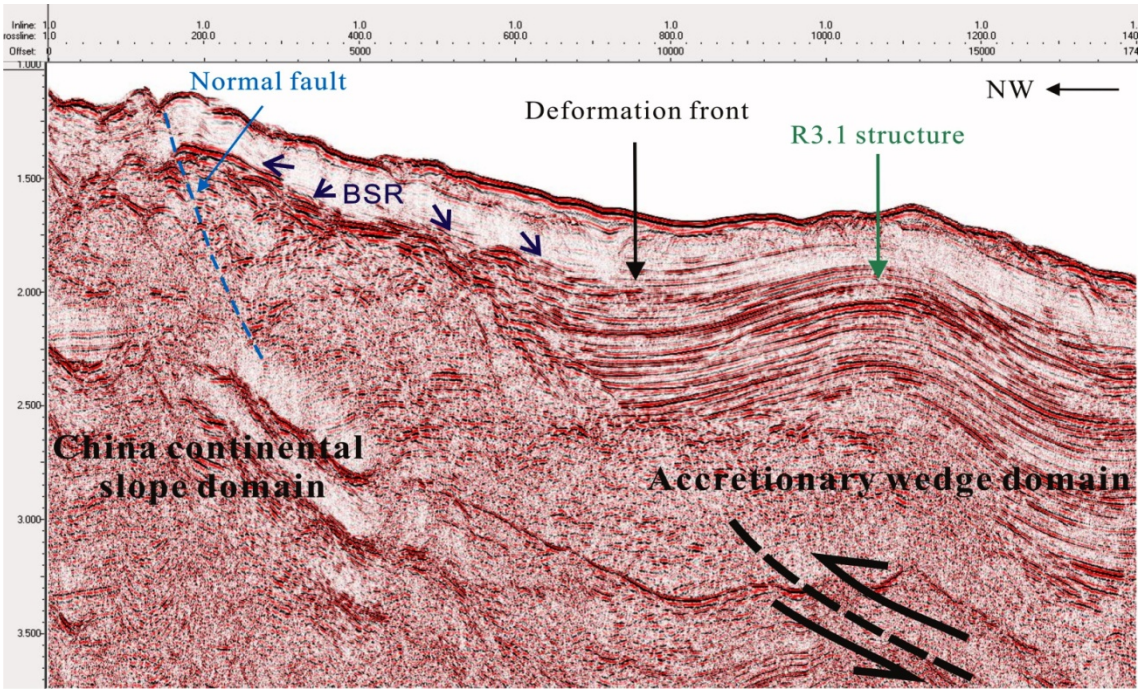

Figure 2-3 In the upper reach of the Penghu submarine canyon, the distribution of BSR and faulting are discovered from the 2-D seismic profiles (Han et al., 2012).

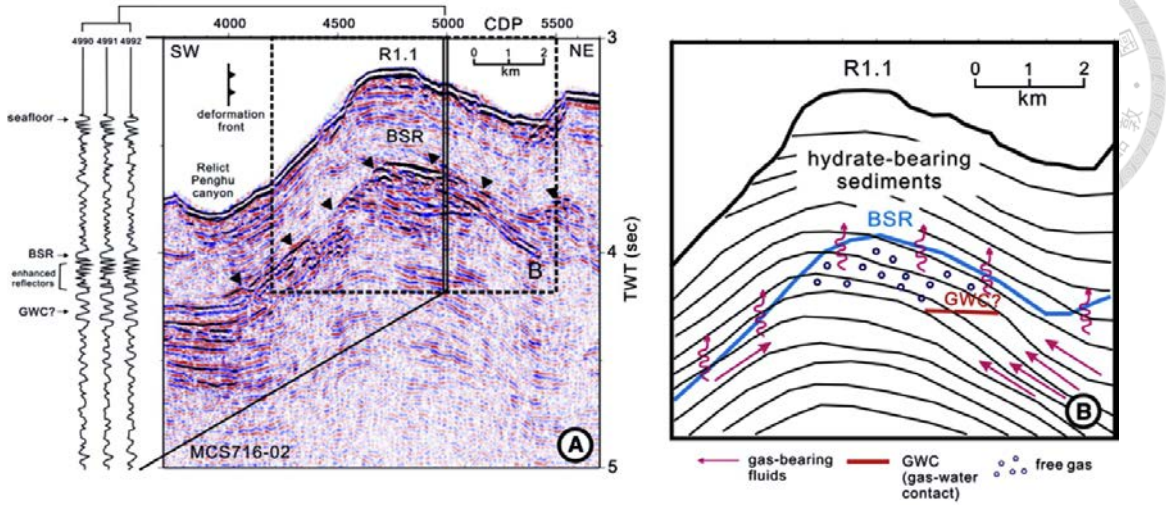

Figure 2-4 (a) Uninterpreted seismic profile; (b) interpreted profile, they both show the continuous BSR (blue line) and underlying flat spot in Frontal Ridge. Three seismic wavelets at CDPs 4990–4992 are displayed on the left of (a). Notice that the phase of BSR waveform is reversed to that of the seafloor and GWC. Straight and wiggled arrows indicate possible gas-charged fluid migration pathways by advection and diffusion processes, respectively (Lin et al., 2013).

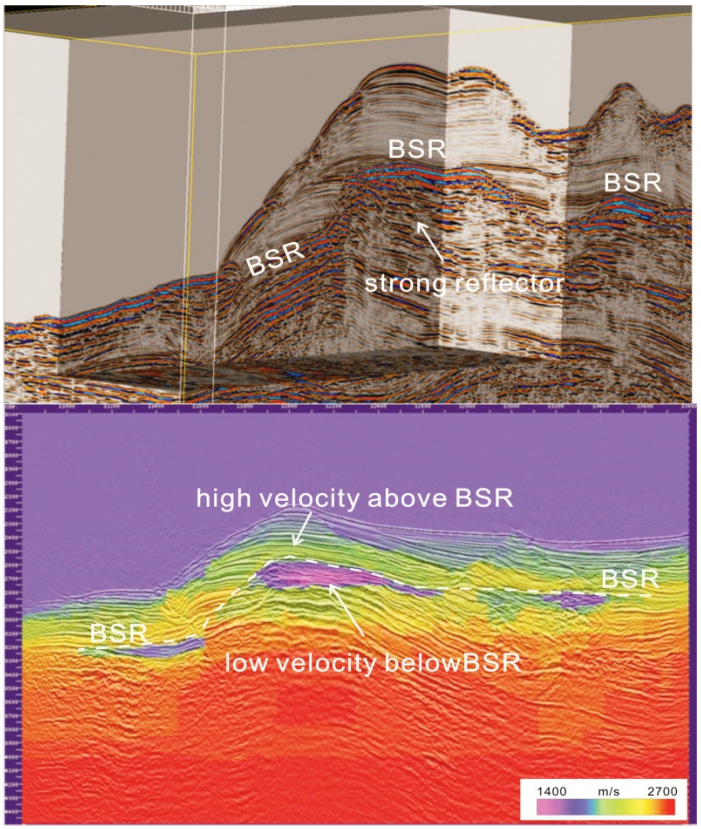

Figure 2-5 Strong reflectors are accumulated below the BSR in upper 3-D seismic image; and the velocity image (Lin et al., 2012a) depicts the same thing from their large differences.

2.1.2 Active Margin - Fangliao Basin & Yung-An Ridge

East of the deformation front, the accretionary wedge off SW Taiwan consists of upper-slope and lower-slope domains (Figs. 2-1, 2-2) (Reed et al., 1992). In the upper slope domain, thirteen submarine mud volcanoes were recognized from the multibeam bathymetry data; and some heat flow anomaly around this region correspond to the gas seeps and plumes detected by the sub-bottom profiler and EK 500 sonar image (Fig. 2-6) (Yang, 2012; Chen, 2013). In the lower Fangliao basin, there are several mud diapirs and anticlines. The rapid changes of depocenter and the course of the paleochannels have been interpreted as evidence of fluid migration (Fig. 2-7, Chen, 2013a).

In the rear segment of the lower slope domain, Yung-An Ridge is a structural high located in the offshore tectonic wedge. High concentrations of biogenic methane may originate at depth and migrate through the homoclinal ridge (Lin et al., 2008) and contribute to the methane oxidizing archaea (ANME) based ecosystem (Lai et al., 2009). There are dense strong BSR, high methane fluxes, and other geological evidence which indicate the presence of gas hydrate (Fig. 2-8, Lin, 2012). Peng (2012) analyzed the in-situ heat flows in Yung-An Ridge, and she found the highest values are observed near fault outcrops at east edge of the slope basin, these results lead us to study deeper fluid migration patterns in this region (Fig. 2-9).

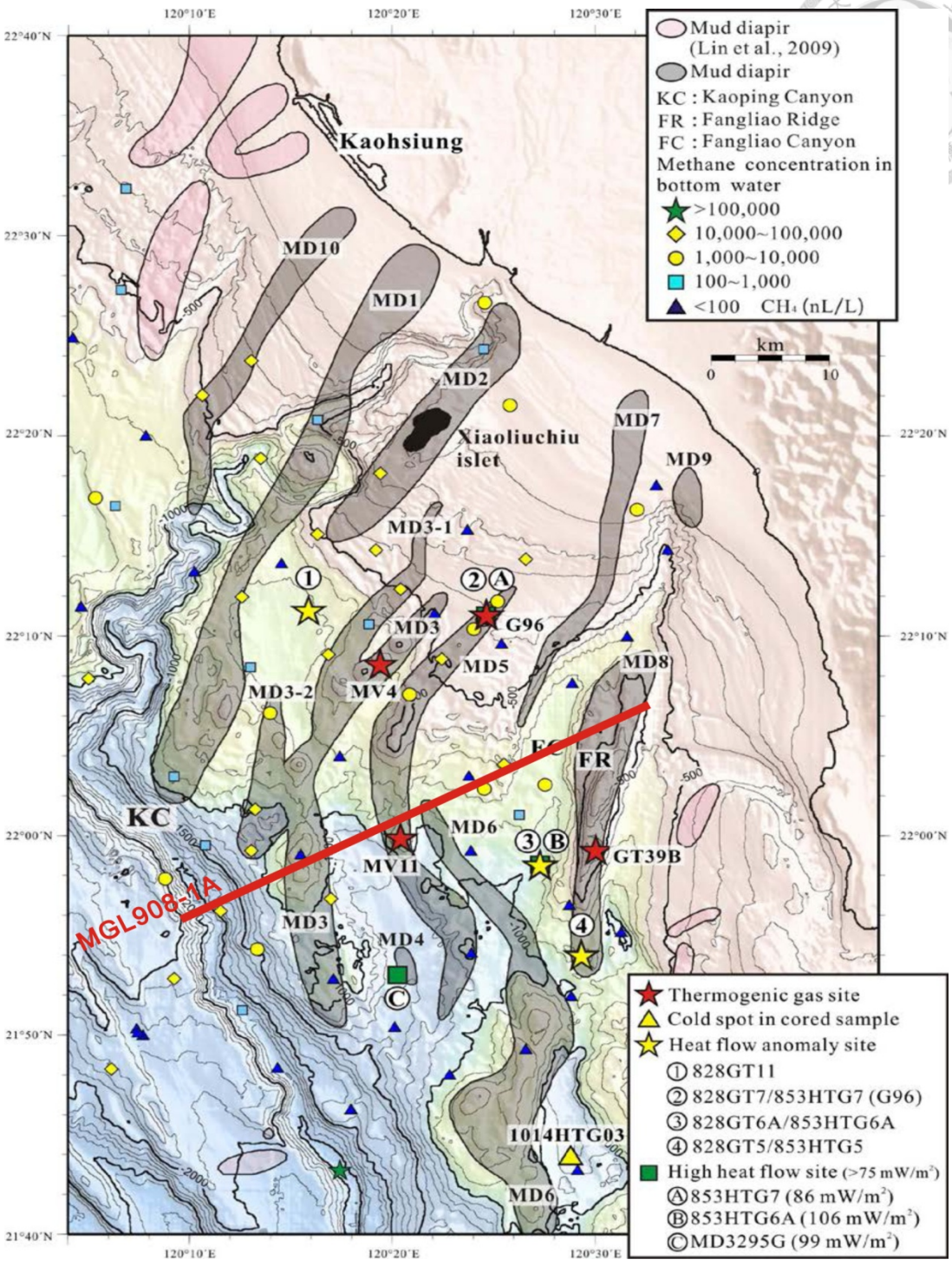

Figure 2-6 According to the geophysical and geochemistry survey off southwest Taiwan, Chen, 2013 compiled the distribution of the heat flow anomaly, methane concentration sites, and possible thermogenic sites on the bathymetry with geological structures around upper Kaoping slope.

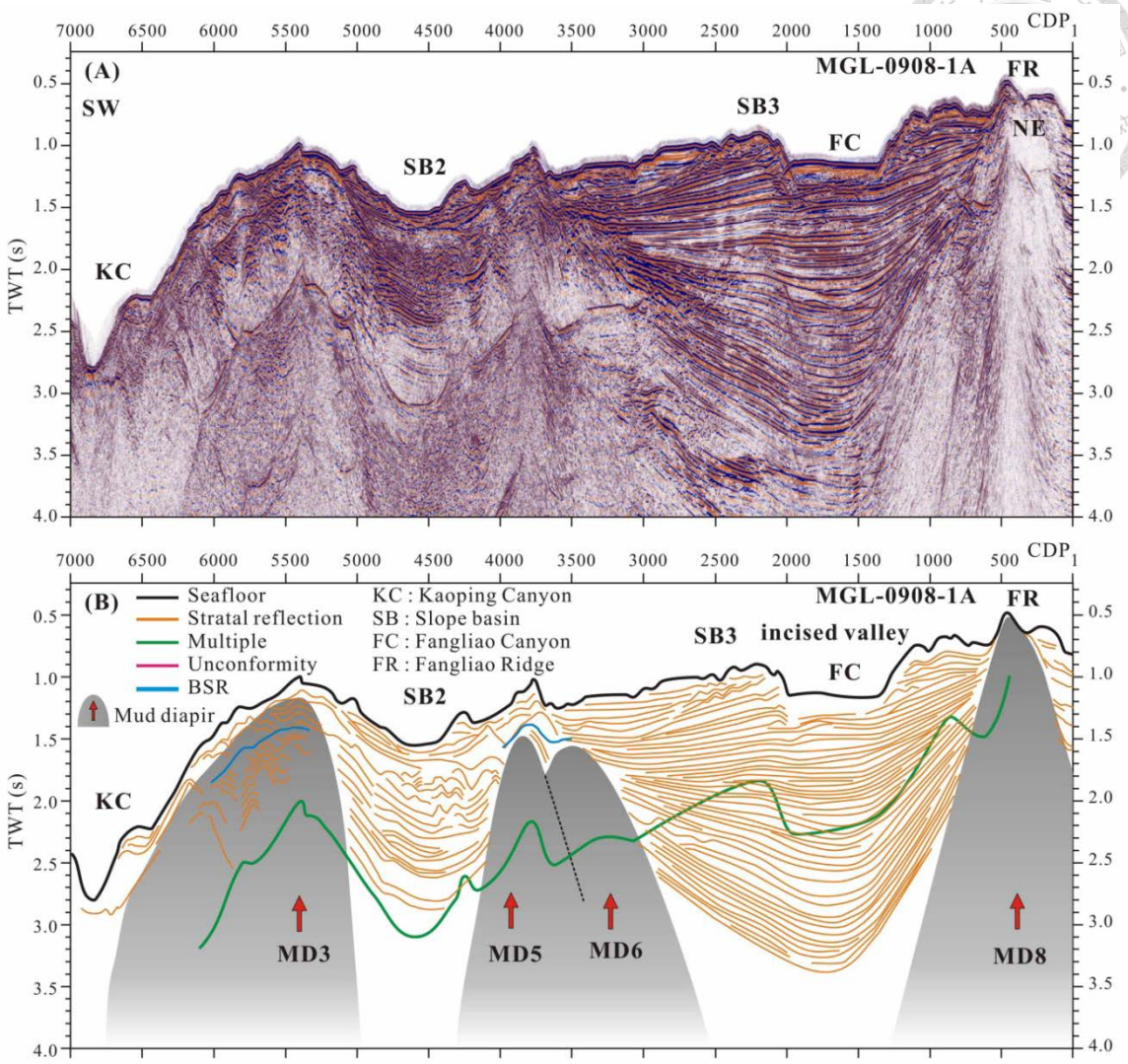

Figure 2-7 Uninterpreted (A) and interpreted (B) seismic reflection profile (MGL0908-1A, located in the red line of fig. 2.6) showed the structure features and BSR (marked in green of B) distributions in the continental slope across the Kaoping and Fangliao Canyons offshore SW Taiwan. (Chen, 2013a). There are four mud diapirs along this profile. MD8 has reached to the seafloor and MD3 is covered by a layer of thin sediments.

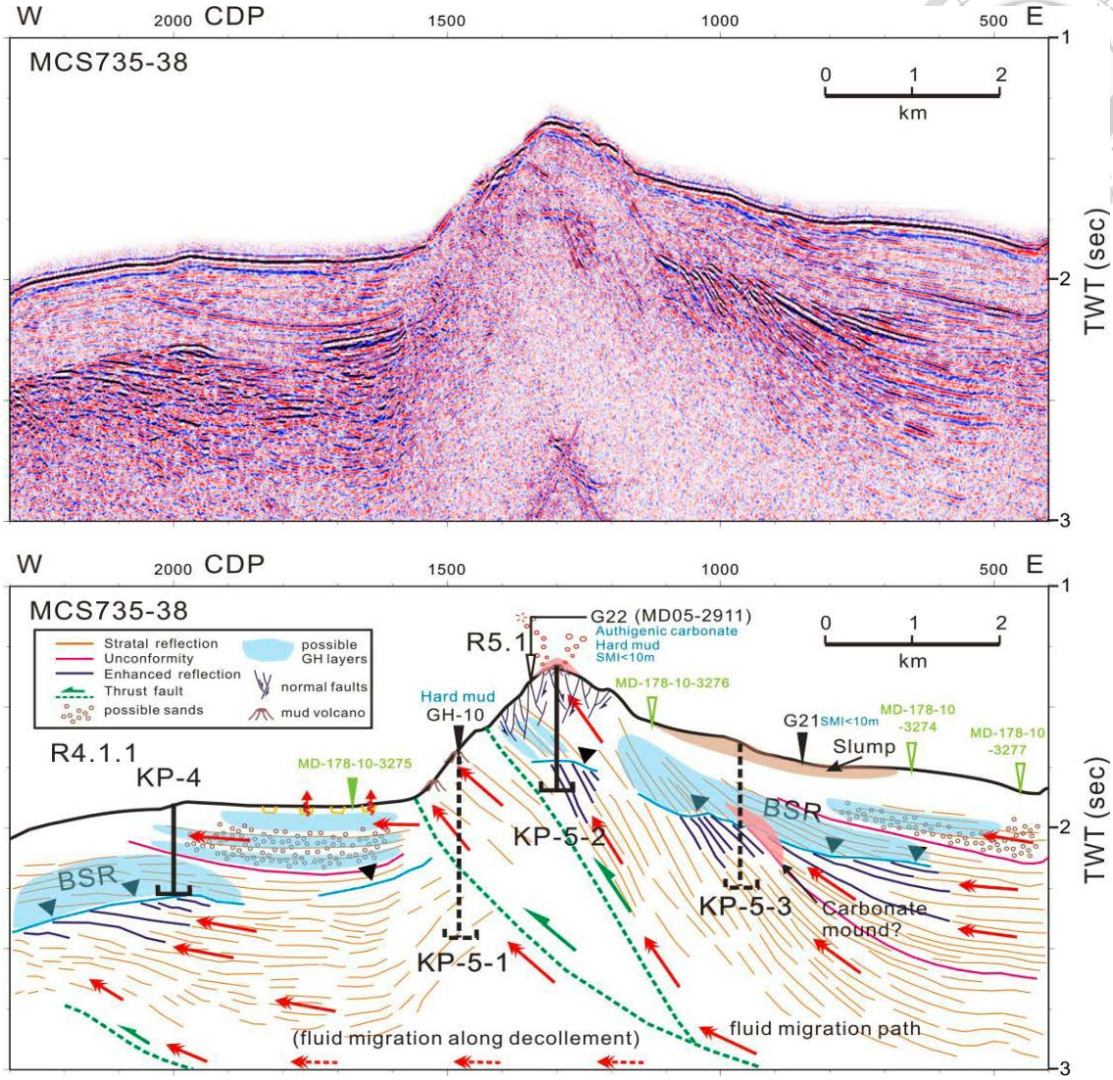

Figure 2-8 Uninterpreted and interpreted seismic reflection profile across the Yung-An Ridge. The black solid invented triangles on the seafloor represent the sample site of near surface sediment. The black open triangle indicates the sample site projected from adjacent areas. The green solid and hollow triangles show MD178 sample sites projected from adjacent areas, respectively. Note that the anomalous features of sediment sample analysis are marked as blue word. (Lin, 2012)

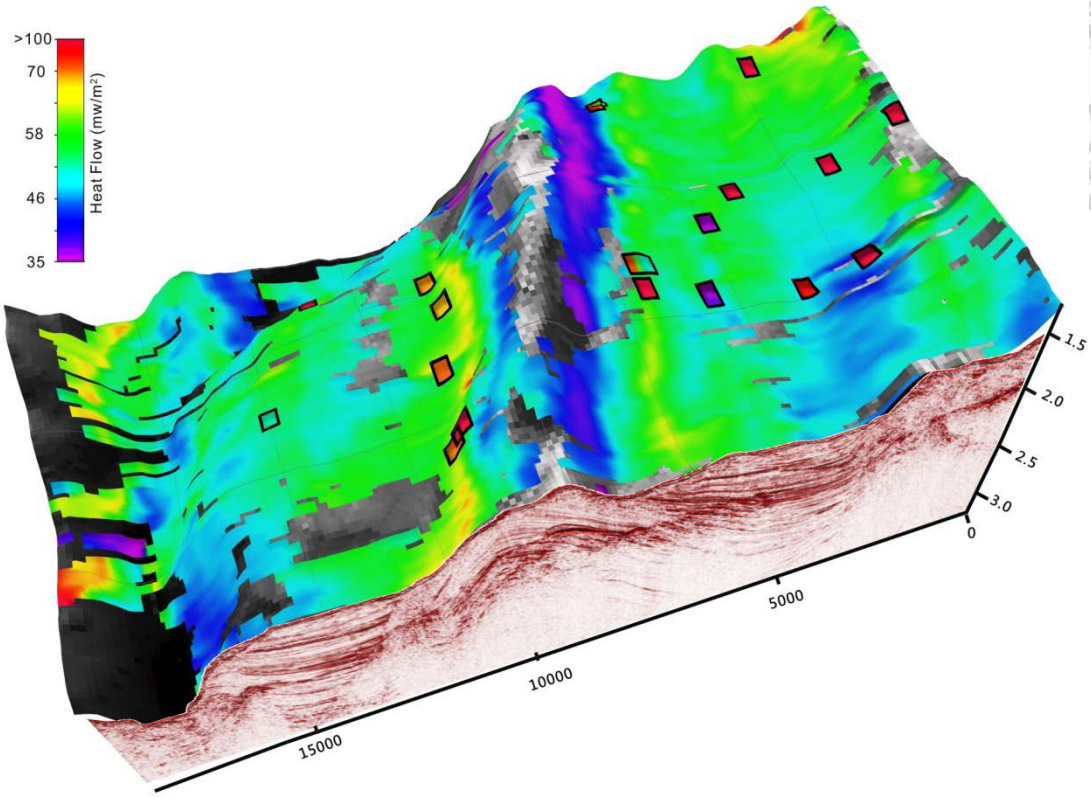

Figure 2-9 The base map shows the 3-D seismic data and heat flow values derived from BSR, which range between 39 and 53 mW/m^2; and the squares point out the values of in-situ heat flow measurements, ranging between 35 ~ 107 mW/m^2. Note that several extremely high values of heat flow (> 100 mW/m^2) were detected here. We use red squares to show them (Peng, 2012). There are not only higher heat flows near the ridge, but also distributed in the depocenter of the eastern basin.

2.1.3 Passive margin - Formosa Ridge

The passive margin is situated in the continental slope of South China Sea. There are many ridges formed by down-slope cutting of submarine canyons, which are mostly developed in the upper part of near the shelf-slope break (Fig. 2-10 a) (Liu et al., 2013). The Formosa Ridge lies to the west of the deformation front in the mid-slope region of the passive China continental slope (Fig. 2-2).

A collaborative Taiwan-Japan ROV diving cruise NT0705 conducted in 2007 offshore southwestern Taiwan has discovered a very densely populated chemosynthetic community animals at a cold seep site on top of the south peak in Formosa Ridge, indicating a vent system dominated by both methane and hydrogen sulfide (Fig. 2-10 b & c) (Lin et al., 2007). Unlike other cold seep environment, the chemosynthetic community of Formosa Ride is supported by unusually high concentrations of dissolved sulfide and methane seeping through sea floor.

To better understand the fluid migration pattern of the seafloor environment, we use a true 3-D seismic data that we collected on R/V Sonne in April, 2013 for the Taiwan-German Collaboration Project. BSR, canyon incision, sediment waves, and a fluid pathway have been found from this seismic data (Fig. 2-11).

In addition to the dense seismic data for support regional geological features, but also heat flow data collected SW offshore Taiwan, as we will discuss in next section.

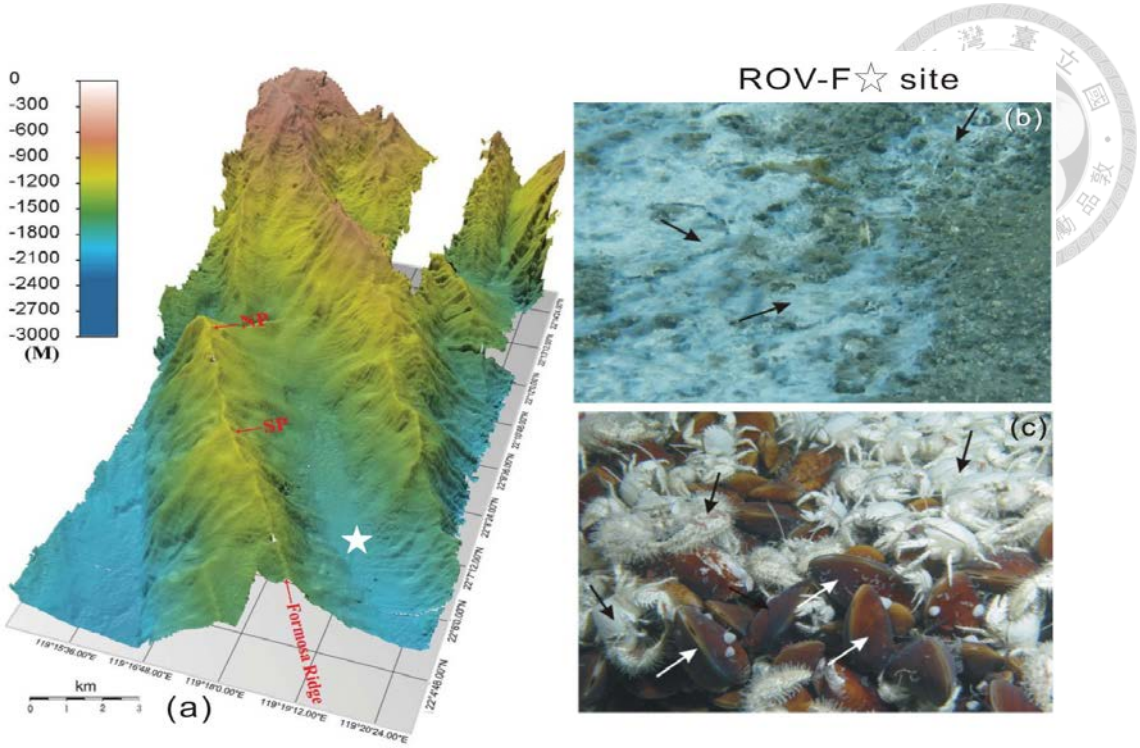

Figure 2-10 Left (a) shows the morphology of the Formosa Ridge revealed by the swath bathymetry data. NP: North peak; SP: Southern Peak; Star: cold seep site (Liu et al., 2013). (b) and (c) are the underwater photographs of typical seep carbonates and chemoauttosynthesis-based community at cold seep in Formosa Ridge. (b) The black arrows point out the bacterial mats; (c) the white and black arrows indicated the mussels and white crabs (Chen et al., 2011).

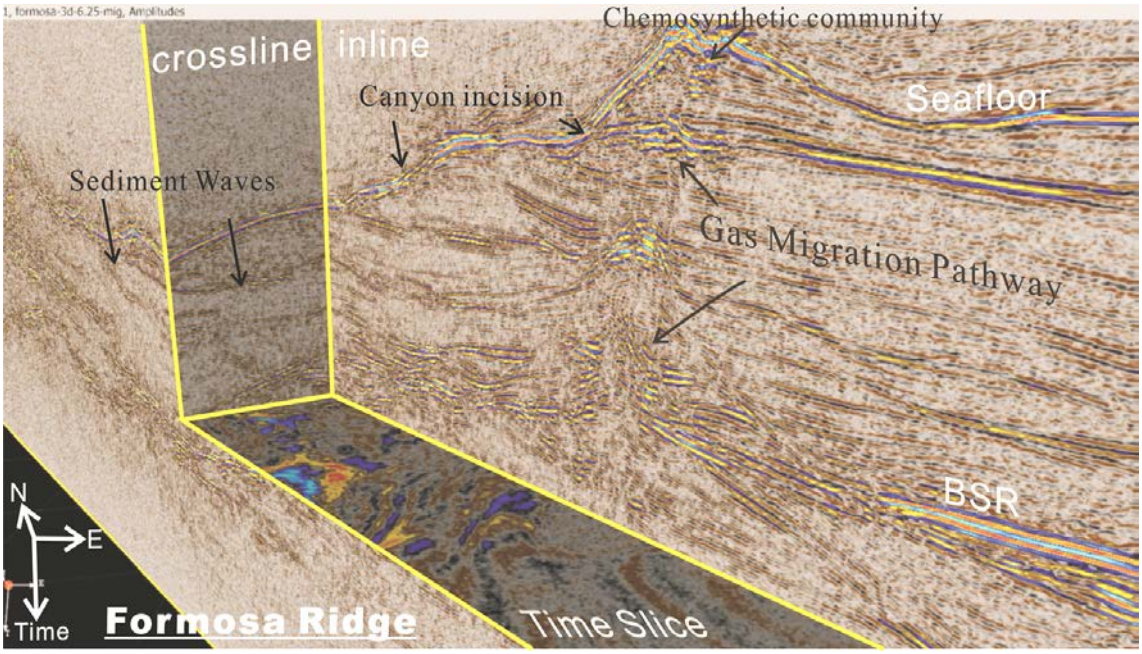

Figure 2-11 The 3-D P-Cable seismic cube in Formosa Ridge showing strong BSR and canyon incision in ridge sides. We have also collected some samples from chemosynthetic communities at the vent site, as shown in the seismic data.

2.2 Thermal measurements on seafloor

Offshore SW Taiwan, two major types of instruments are used extensively for marine geothermal investigations currently (Fig. 2-12): One is Lister-type heat probes, which is self-contained with multi penetration heat probes to measure both thermal gradients and conductivities of sediments in-situ (Hyndman et al. 1979; Lister 1979; Shyu et al. 2005) (Fig. 2-13a). But Lister probes are seldom longer than 6 m due to the weak mechanical strength of their slim thermistor tubes. Another type is to use miniature temperature loggers (MTL) attached to a solid-steel lance or a core barrel to measure temperatures at different depths (Pfender and Villinger, 2002), however, thermal conductivities have to be measured with additional needle probes (Von Herzen and Maxwell 1959; Lister 1979). The resolution of these instruments could be 0.1-1mK (Shyu and Chang, 2005; Chang and Shyu, 2011). So we generally use MTL attached to gravity coring device to derive the temperature data for marine sediments (Fig. 2-13b) (Chang and Shyu, 2011).

According to results from 176 in-situ temperature measurements offshore SW Taiwan (Shyu, 2013), the conductivities are generally uniform with a mean value of 1.10 W/mK that is higher than that of typical marine sediments (~ 0.9 W/mK). They may be affected by the grain sizes of the sediments, so the highest one is just off coastal region with very shallow water (~ 1.94 W/mK); and the lowest one is associated with

the deep sea sediments which is far away from Taiwan (~ 0.3 W/mK) (Fig. 2-14a). Regarding the geothermal gradient patterns (Fig. 2-14b), it seems to get higher from the coast (-0.02 °C /m) to near the trench (0.144 °C /m). The average geothermal gradient is about 0.05 °C/m. The average heat flow value in this region is about 61.5 mW/m^2, after multiplying the thermal conductivities and geothermal gradients together. The higher and lower heat flows occurred in deformation front vicinity (~ 100 mW/m^2) and the accretionary wedge (<30 mW/m^2), respectively (Fig. 2-14c) (Shyu, 2013).

Figure 2-12 Two major types of ship-operated underwater instruments are used in marine geothermal investigations currently (which developed and improved by Prof. Shyu's Geothermal Lab, Institute of Oceanography, National Taiwan University): One is Lister-type heat probes (bottom), which is self-contained with multi penetration heat probes to measure both thermal gradients and conductivities of sediments in-situ; another type is small temperature probes which use miniature temperature loggers (MTL) attached to a solid-steel lance or a core barrel to measure thermal gradients (middle). If we use MTL, we have to use additional needle probes (center) to measure the thermal conductivities of the sediments.

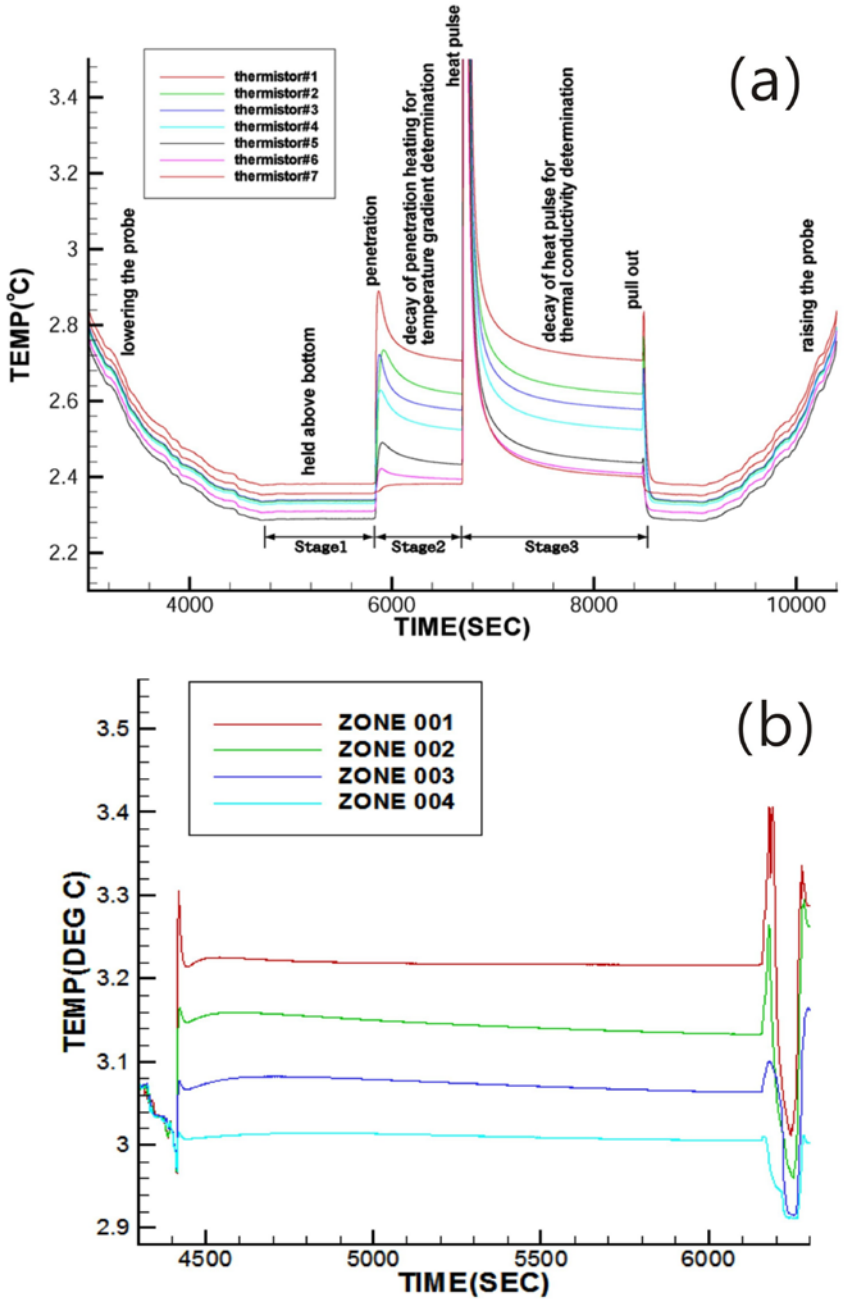

Figure 2-13 Typical examples of temperature vs. time during a heat flow measurement using Lister and MTL probes. (a) There are three important stages for geothermal data analysis on a Lister probe: stage 1 means the probes are staying just above the seafloor to wait for the instrument to be become stable; stage 2 indicates that the probes are penetrating into the seafloor and waiting for the temperature equilibrium, and the temperatures in different subbottom depths could be used to calculate the geothermal gradient; stage 3 shows the self-heating pulse to derived the thermal conductivities (Shyu, 2005). (b) When MTL probes attached to the seafloor, the frictional heat raised temperatures abruptly then gradually decayed, and then we could derive the equilibrium temperatures as the in-situ temperatures. (Lee, 2008)

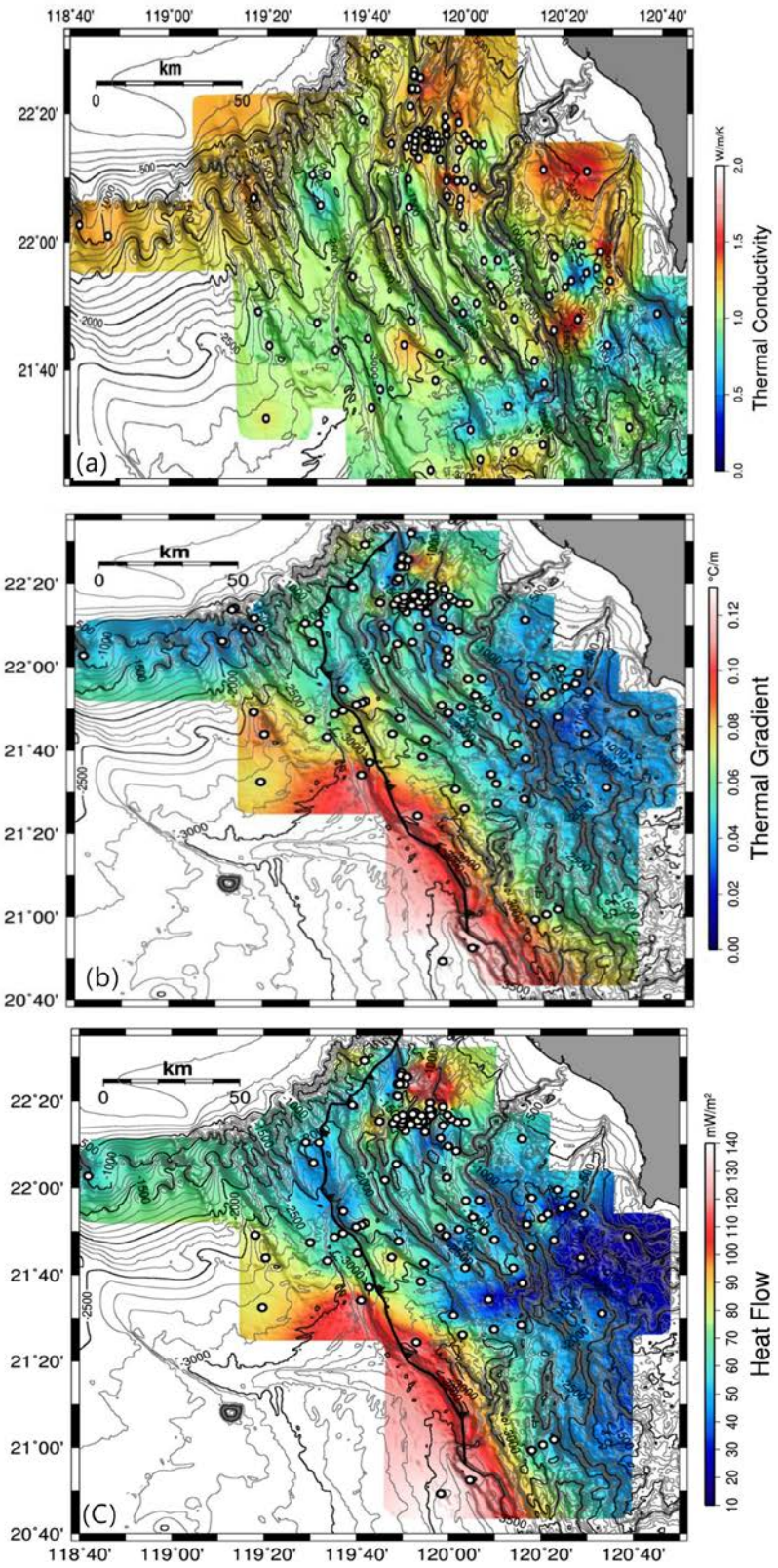

Figure 2-14 176 in-situ temperature data offshore SW Taiwan collected by the geothermal lab (Shyu, 2013), (a) and (b) show the distribution of the geothermal gradients and thermal conductivities, respectively. And (c) is the product of the upper two values to derive the heat flow distribution.

2.3 Implication of BSR for fluid migration

2.3.1 Occurrence and natural condition of Gas Hydrate (BSR)

Methane hydrates form when water and methane combine to generate a crystalline substance that looks like ice. Most hydrates have been found where there is a sufficient supply of methane and where pressure and temperature range between 0.2-5 MPa and 0-25 ^{o}C respectively (depends on the water depth) (Kvenvolden and McMenaminm, 1980). The increase in temperature with depth below seafloor causes methane hydrate to become unstable and dissociate, despite increasing pressure. As a result, the base of methane hydrate stability zone (BGHZ) defines a “phase boundary” separating the stable gas hydrate above from the instable field below (Hyndman and Davis, 1992).

However, the conditions of BGHZ are more strongly depending on a function of temperature than of pressure (Fig. 2-15, Hyndman and Davis, 1992), therefore we usually found them in the sediments at water depth greater than 500 meters, depending on the water temperature, while the temperature increases along the geothermal gradient (geotherm). So we could estimate the temperature at the BSR by combining the information of hydrate phase boundary, pressure, and salinity (Brown et al., 1996).

Regarding the seismic data, BSR are generally inferred from these following observations:

(1) In seismic profiles, a BSR is a reflection with high amplitude and sub-parallel to the

seafloor topography but having reversed polarity compared to the seafloor reflection (Fig. 2-15a & b), it indicates a negative acoustic impedance contrast (high-velocity hydrate above and low-velocity free gas below) at the BSR boundary (Fig. 2-15b).

(2) The P-T condition of BSR is generally consistent with the maximum temperature and pressure at which hydrates is stable (Fig. 2-15c). BSR are commonly observed at depths of hundreds meters below the seafloor in continental margins sediments that have undergone recent tectonic consolidation or rapid accumulation (Fig. 2-15a). And its depth is strongly influenced by the geothermal gradient in local marine sediments.

Thus, we can use BSR to derive temperatures at the depths of BSR in order to study the regional geothermal gradient patterns.

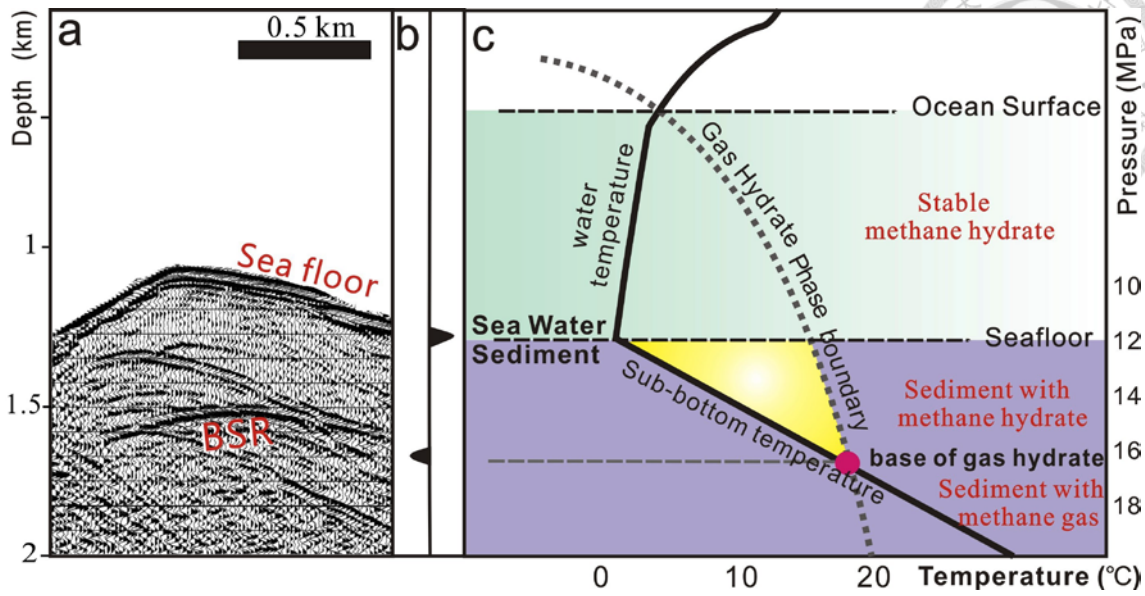

Figure 2-15 BSR feature maps on the seismic data and the P-T condition profile: The left panel (a) shows an example of a BSR sub-parallel to the seafloor topography in a stacked multi-seismic profile. A trace shows amplitudes of the seafloor and BSR in center panel (b), BSR have reversed polarity compared to the seafloor reflection, it is due to the gas hydrate bearing in sediments above and free gas below. The right panel (c) is the phase diagram of gas hydrate and its relationship with the marine environment (modified after Hyndman and Davis, 1992). BSR usually corresponds to the phase boundary separating the stable gas hydrate above from a field of instability below. At the base of the gas hydrate stability zone (BGHS), gas hydrate begins to dissociate due to temperature and pressure conditions no longer meeting the requirement for methane hydrate to be stable (e.g., too higher temperature). Thus, hydrate is confined to the uppermost layer (above BGHS) of sediments, while free gas is stable below the BGHS.

2.3.2 BSR and heat flow studies

Since BSR is a specific boundary between the gas and hydrate, two models for the gas hydrate accumulation have been proposed. First, gas hydrates are generated in-situ from organic carbon contained in the sediments of a gas hydrate zone (Claypool and Kaplan, 1974), whereas in the second, gas hydrates are derived from upward migrating fluids containing light hydrocarbons (Hyndman and Davis, 1992). In addition, Paull et al., (1994) have proposed that the gas hydrates are re-concentrated by "hydrate recycling" in which gas hydrates form from upflow of dissociation gas derived from pre-existing gas hydrates when BGHZ moves upward by tectonic uplift or with burial. In our study, we study the BSR-based temperatures to indicate the thermal models which may be associated with the fluid migration or the regional tectonic effects.

Actually, P-T conditions at BSR have been used to estimate heat flows in several accretionary prism settings (Villinger et al., 2010). Shipley et al. (1979) firstly estimated geotherm from the depth of the BGHZ on continental slopes and rises. Townend (1997) concluded that BSR data is very useful in determining offshore heat flow around New Zealand, and suggested that heat flow estimates need to be corrected for thermal effects of ongoing sediment deposition. Ganguly et al. (2000) have analyzed that the heat flow variations from data of BSR on the continental slope of the northern Cascadia margin, and accentuated that carrying out topographic corrections in regions of significant relief,

such as the continental slope are important to heat flow. Previously, Hormbach et al. (2012) has directly used the BSR depth anomalies to detect and quantify the amount of methane hydrate, the analysis shows anomalously shallow BSR near the crests of ridges; and anomalously deep BSR near the flanks (Fig. 2-16).

Regarding BSR studies in Taiwan region, Reed et al. (1991) first documented the BSR offshore Taiwan and its relation with gas hydrate; Chi et al. (1998) systematically studied the BSR offshore Taiwan and discussed the factors controlling its distribution; Schnürle et al. (2004) used multi-channel seismic reflection and ocean bottom seismic data to study the BSR in this region; Chi et al. (2006) & Liu et al. (2006) evaluated the volume of the hydrate stability zone and published the updated BSR distribution for wider regions. And recently, under the auspices of Central Geological Survey (CGS), Ministry of Economic Affairs, the upgraded seismic data shows more dense-spreading BSR, which were compiled by the Seismic Exploration Lab (SEL), Institute of Oceanography, National Taiwan University (IONTU) (Fig. 2-18, Liu, 2013).

In terms of deriving BSR-based temperatures to study Taiwan thermal structure, Chi and Reed (2008) had compiled 1107 BSR-based geothermal gradients and combined with previous published in-situ measurement heat flow data (e.g. Shyu et al., 1998, 2006; Lee and Cheng, 1986), then discovered the thermal structure varied both in space and time (Fig 2-17) during the arc-continent collision. Most of the BSR-derived

heat flows are within 35 ~ 85 mW/m^2 in the subduction to the south, which have high values along the trench and decreased toward the arc; on the other hand, the heat flows are low near the frontal thrust, and increase, instead of decrease, toward the mountains in the collision zone.

Furthermore, Baba et al., (2004) used BSR as the indicators of gas hydrate and free gas accumulation to classify the BSR types in Nankai Trough (Fig 2-19). Based on his concepts, Lin et al., (2009a) also discussed about the geological controls on BSR occurrences from those classifications (Fig 2-20). They all suggested that the tectonic control is an important factor for BSR distribution, and the existence of multiple fault zones in accretionary prism may help tap more deep-seated gas-bearing fluids.

Besides, there are also plenty of the geochemistry studies about the methane hydrate offshore SW Taiwan, especially after we derived some longer coring samples on Marine Dufresne (MD) cruise in 2010. Yang, (2012) combined the carbon isotope of dissolve inorganic Carbon (DIC) to infer the methane flux information (Fig 2-21).

All these studies successfully addressed several geodynamic processes from their results. But there are still many remaining issues, especially now that we have much denser and well-coverage thermal dataset derived from BSR offshore SW Taiwan (Fig 2-18), I would like to further extend these BSR to study geological processes by examining regional temperature fields.

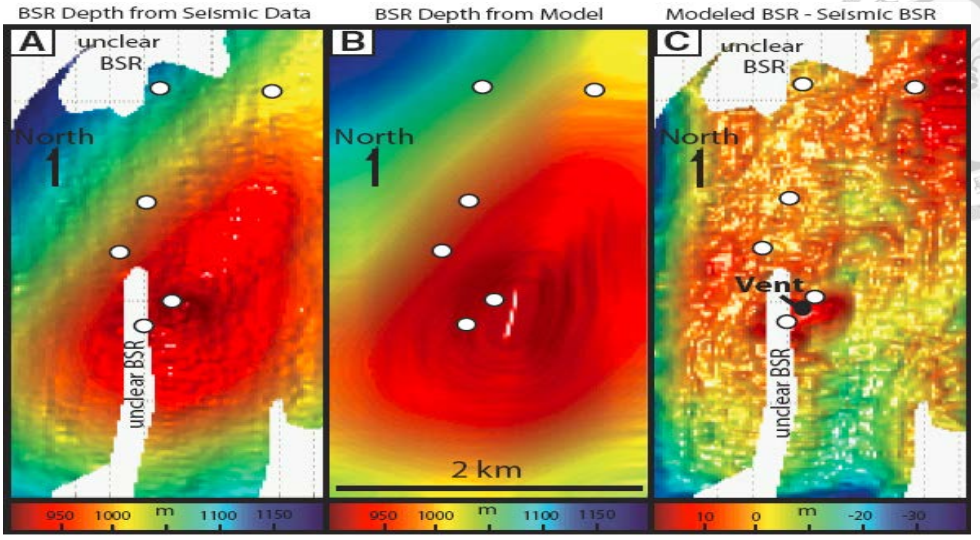

Figure 2-16 Subtracting modeled steady-state BSR depths from seismically imaged BSR depth at Hydrate Ridge reveals clear BSR depth anomalies across the site. (A) Picked BSR mbsl depths from 3-D seismic volume; (B) Modeled BSR mbsl depths in 3-D steady-state cube; (C) Differences between A and B (Hormbach et al., 2012)

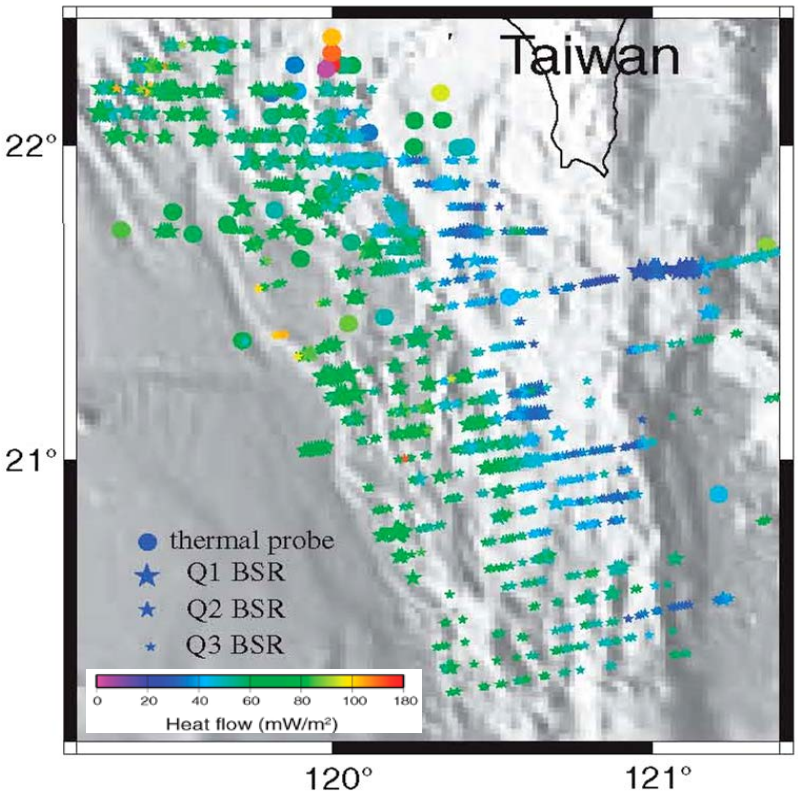

Figure 2-17 Distribution of BSR-based heat flows (Chi and Reed, 2008). Large stars Q1 indicate highest confidence in BSR identification. Medium stars Q2 indicate probable BSR identification. Small stars Q3 indicate possible BSR identification. The large circles are the heat flow measurement results from Shyu et al., (2006). Note higher geothermal gradients along the trench in the subduction zone.

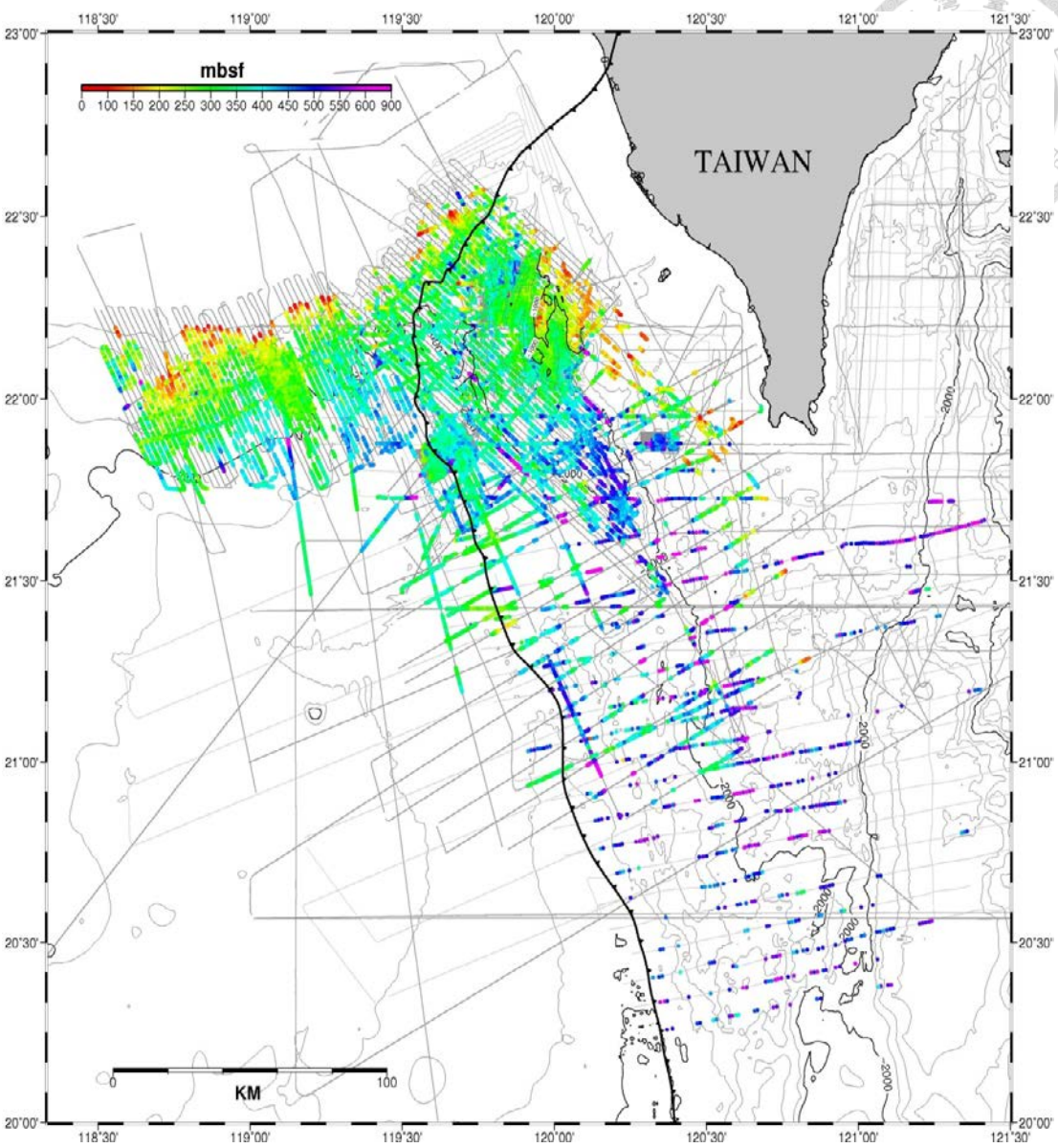

Figure 2-18 Updated BSR distribution maps: Combined the BSR distinguished from Chi et al. (2006) & Liu et al. (2006) with recently collected and compiled seismic data by Prof. Liu's seismic exploration Lab (Liu, 2013).

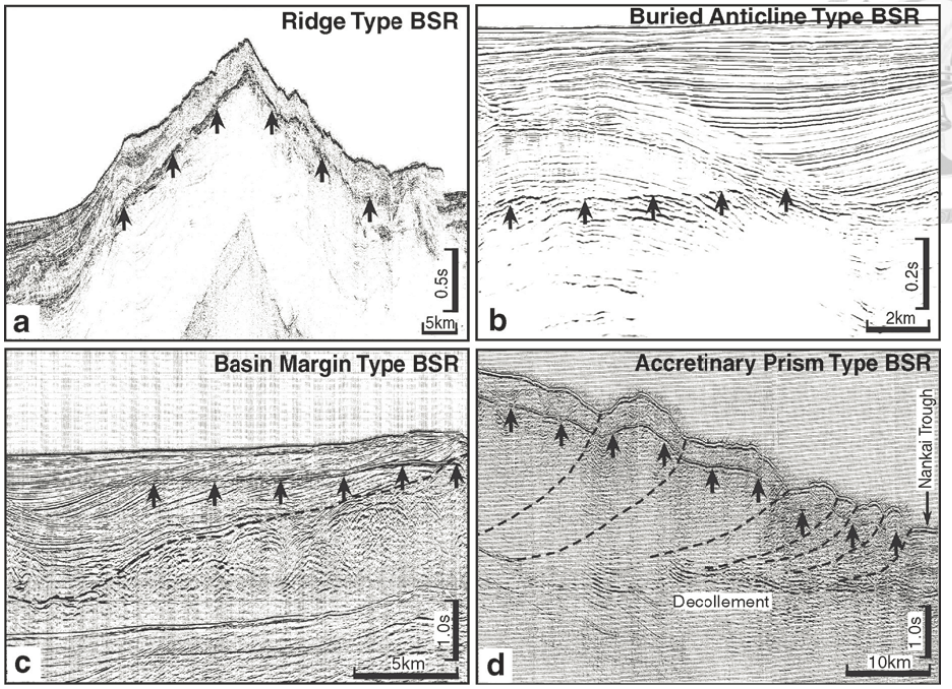

Figure 2-19 Seismic examples of BSR types along the Nankai Trough (Baba et al., 2004): (a) Ridge type BSR from southern flank of the Shima Spur; (b) Buried anticline type BSR from south- western margin of the Kumano basin; (c) Basin margin type BSR on southwestern margin of the Kumano basin. Dashed line indicates the base of the basin; (d) Accretionary prism type BSR off Tosa basin.

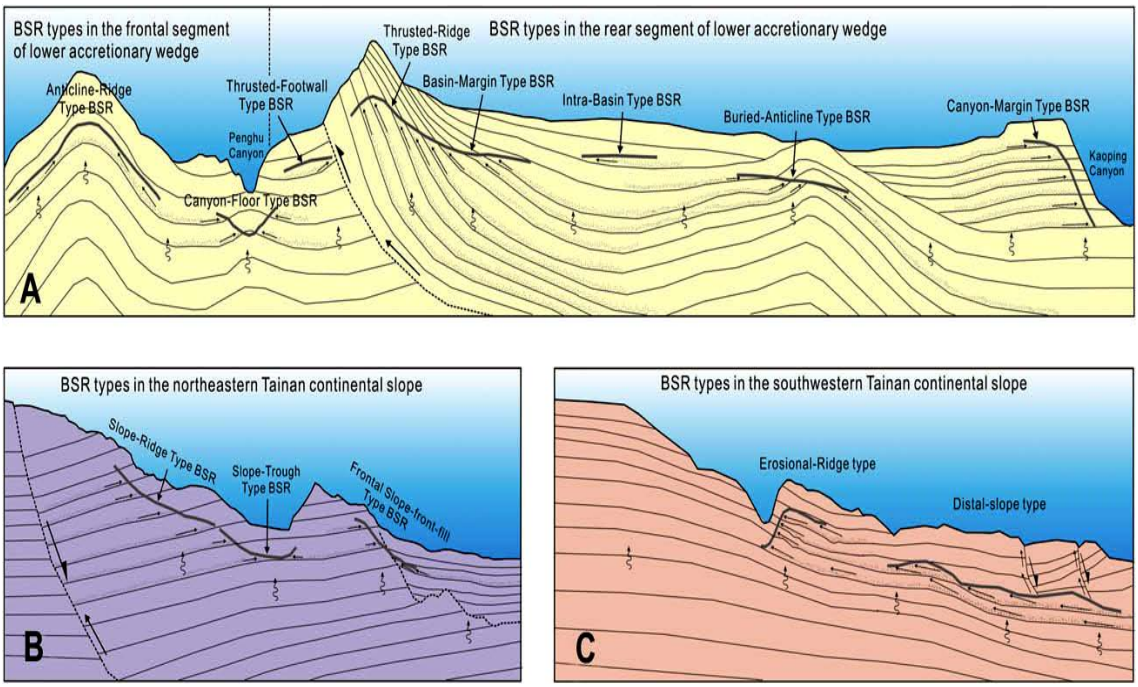

Figure 2-20 Three major BSR-occurrence models (Lin et al., 2009a) in (A) accretionary wedge and (B, C) continental slope, showing existence of all kinds of BSR types and the migration paths of gas-bearing fluids related to various structural styles.

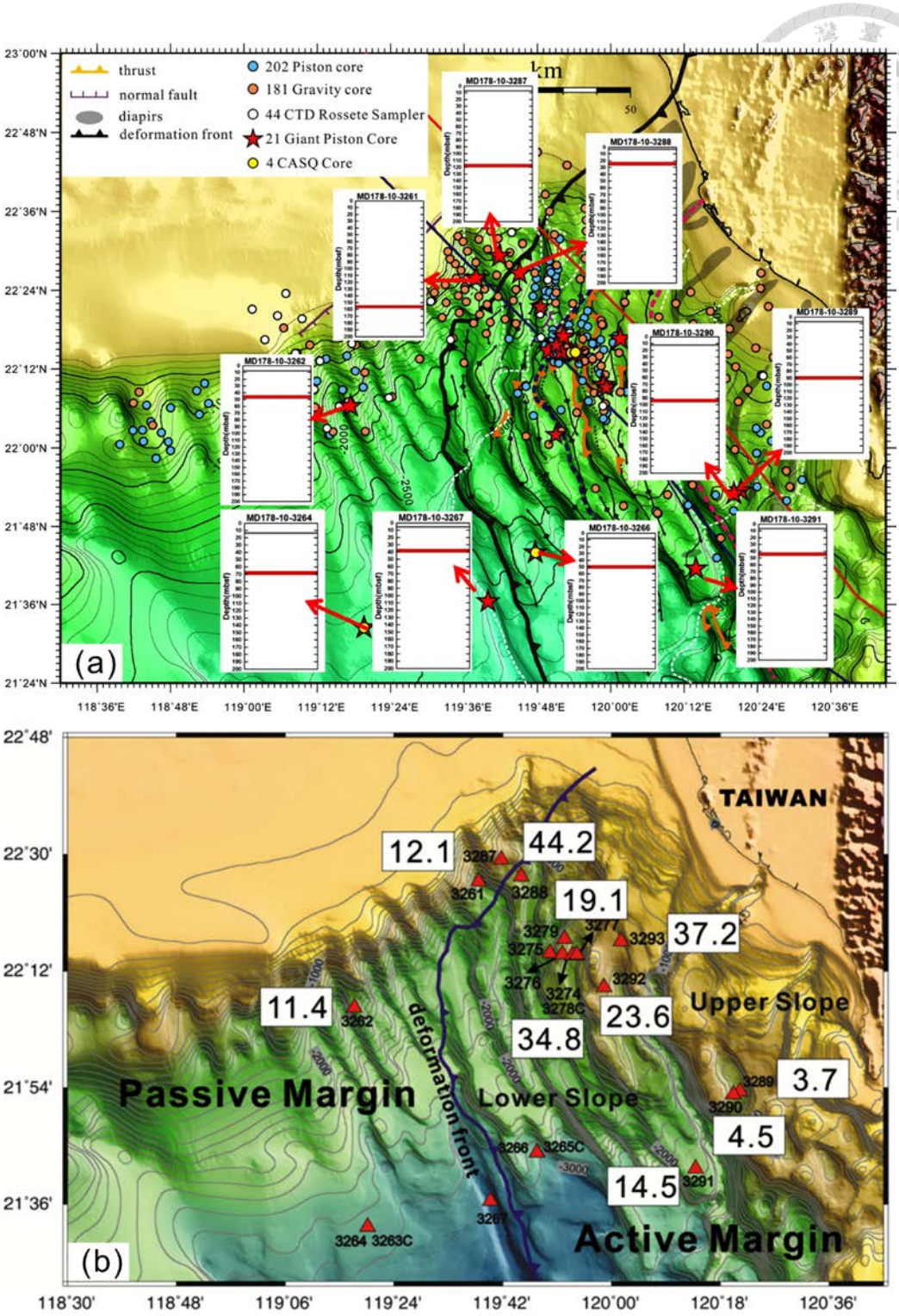

Figure 2-21 The distribution of (a) methane hydrate formation depth (mbsf) and (b) the methane hydrate flux (mmol/m^{2}year) (Yang, 2012).

Chapter 3: Deriving 1-D Fluid Migration Rates from BSR

In this chapter we study vertical fluid migration patterns using the BSR-based temperatures offshore SW Taiwan. Since the gas hydrate forms wherever appropriate physical conditions, as long as the moderately low temperature and high pressure exist. Owing to the BSR are usually sub-parallel to the seafloor and increasing the subbottom depth with water depth, after estimated the depth of BSR from seismic data, the hydrostatic pressure can be derived, and the BSR-based temperatures are predictable from the phase diagram of the gas hydrate.

First we collected the seafloor information which we may need in following simulations. For the seafloor depth ($\boldsymbol{H_{SF}}$) above BSR, we assumed 1450 m/s as the seismic velocity of water, then multiplying it to one way travel time of the seafloor defined from the seismic data. For temperature on the seafloor, we used least-squares fitting on the water temperature as a function of water depth provided by the National Center for Ocean Research of Taiwan. Such water temperature data were collected using CTD measurements of water column temperatures at different depths for different regions, which have a 0.001°C resolution for fitting temperature curves (Fig. 2-15c).

$$\boldsymbol{T_{SF}} = 0.2597\times(\mathrm{Ln}\boldsymbol{H})^3 - 3.802\times(\mathrm{Ln}\boldsymbol{H})^2 + 10.67\times(\mathrm{Ln}\boldsymbol{H}) + 26.96 \qquad \text{(Eq. 1)}$$

Where $\boldsymbol{T_{SF}}$ is the temperature of the seawater right above seafloor in °C. Ln$\boldsymbol{H}$ is the natural log of water depth in meters. The water depths in this dataset range from 600 to 3700 m, so the $\boldsymbol{T_{SF}}$ ranges from 7.5 to 2.0 °C assuming that the temperature on the seafloor sediment is similar to that of the seawater.

3.1 BSR-based temperatures and geothermal gradients

The temperature at BSR can be inferred from two-component (methane and water) hydrate phase equilibrium and estimated in situ pressures (Fig. 2-15c). Combining the depth and temperatures data of the seafloor and BSR, the geothermal gradient and heat flow can be estimated using the following basic equation (Carslaw and Jaeger, 1959):

$$Q = -k\,dt/dz \qquad \text{(Eq. 2)}$$

Where Q is heat flow in mW/m^2; k is thermal conductivity of sediments in W/m^{o}K; dt/dz is the geothermal gradient in K/km, t is temperature in K, and z is the subbottom depth in km.

To derive the temperatures of BSR in our study, first we converted the two-way travel time of the BSR to depth (e.g. Chi et al., 2006) using empirical Hamilton formula (Hamilton, 1980) which is a velocity model derived from global ocean sedimentary profile datasets (Eq. 3). Then we combined the BSR subbottom depth (H_{BSR}) and the water depth (H_{SF}) to derive the hydrostatic pressure, which was applied to the methane hydrate phase diagram to derive the temperatures at the BSR (T_{BSR}) (Eq. 4).

$$H_{BSR} = V_{AVG} \times t = [\,1511 + (\,1041 \times t\,) - (\,372 \times t^{2}\,)\,] \times t \qquad \text{(Eq. 3)}$$

Where H_{BSR} is the BSR subbottom depth in meters; V_{AVG} is the average velocity of sediments above BSR in m/s; and t is the one-way travel time of BSR subbottom depth in sec.

$$T_{BSR} = 2.03 \times [\,\log(\,H_{SF} + H_{BSR}\,) - 2\,] \times 9.75 - 4 \qquad \text{(Eq. 4)}$$

Where T_{BSR} is the temperature at the BSR in ^{o}C; H_{BSR} and H_{SF} are the BSR subbottom depth and water depth in meters; H_{SF} is the water depth in meters.

3.2 Uncertainty of Geothermal Gradient

Geothermal gradients are important parameters for our study. For the study of 1-D fluid migration rate, we have to include as many temperature data as possible so we can improve the credibility of the geothermal gradient curve (see 3.3.1); and for the study of 2-D or 3-D temperature fields, based on the in-situ measurement data and BSR-based temperatures, we have to test a range of geothermal gradients to derive appropriate background models (see 4.1).

There is a large scattering of the BSR subbottom depths offshore southwestern Taiwan, mostly ranging from 250 to 600 m (0.2 – 0.7 s in two-way travel time). This scattering may represent the wide range of thermal gradients derived from BSR (Fig. 2-14). By comparing the discrepancies between the Hamilton's velocity function and a velocity model from a nearby drill core (Lin et al., 2003), Chi and Reed (2008) had proposed that the velocity model discrepancy will cause less than ± 30% variation in BSR subbottom depth, and translating to 0.5-2.5 ^{o}C/km changes on geothermal gradients.

Here, we have more accurate velocity models in this region to carefully examine the errors. Using the large offset seismic data collected and processed from the Seismic Exploration Lab, NTU, it's possible for us to compare Hamilton's velocity model with the velocity analysis models derived from pre-stack depth migration (PSDM) (Tu and

Liu, 2009; Tu, 2010; Tsai, 2010). According to their PSDM analysis results in Yuan-An Ridge and Formosa Ridge (Fig. 3-1), there are about 9% and 4% differences on BSR subbottom depths with respect to the Hamilton velocity model, respectively. According to their estimation, these analyses show that we might have less than 2% discrepancy on geothermal gradient estimation, so our results are still reliable. In addition, because we are only working on small regions (the areas are less than 310 km^2) where the crustal velocity and gas hydrate composition should be very similar, it is likely that the errors are systematic for each site.

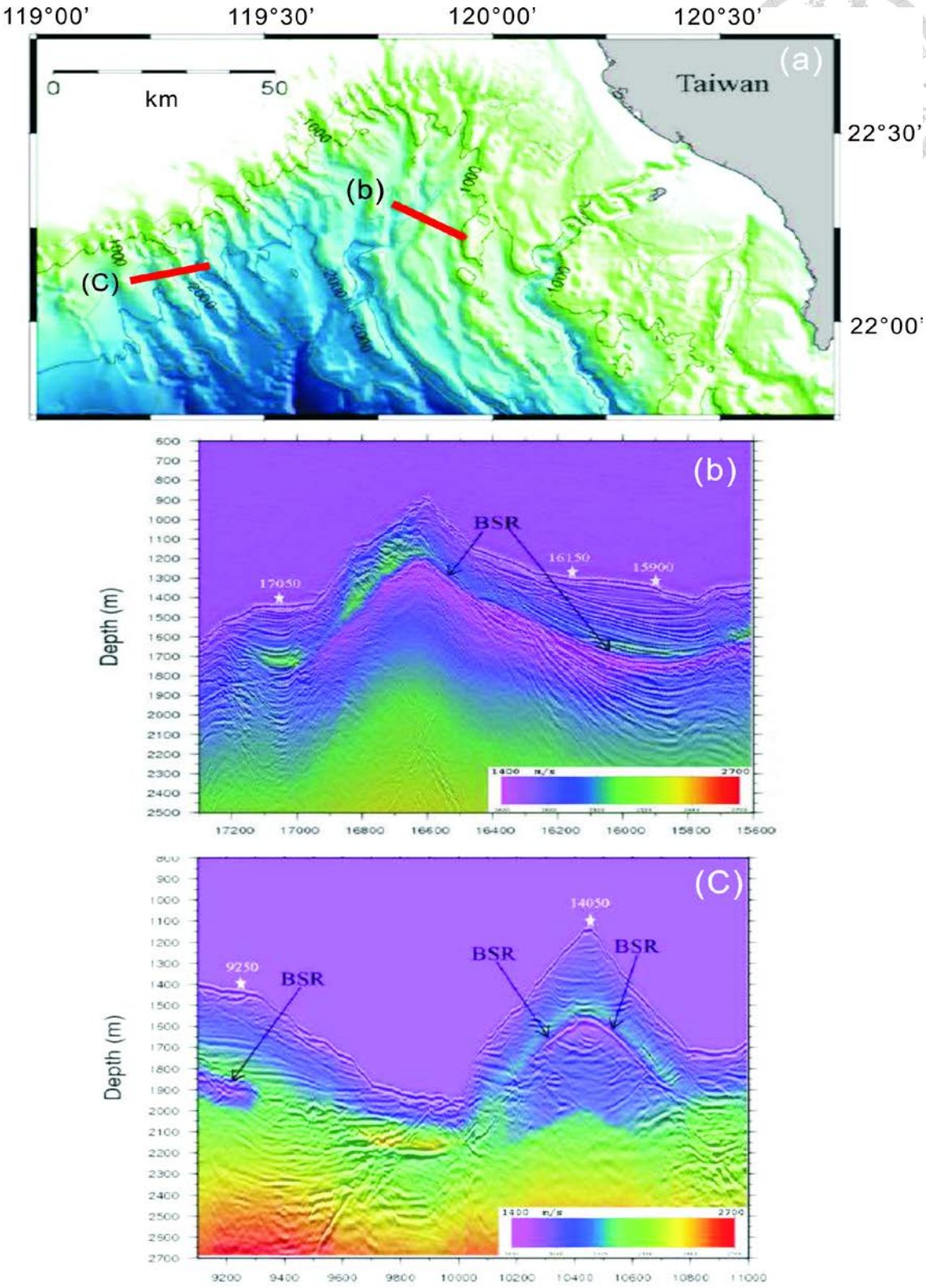

Figure 3-1 A depth profiles after PSDM velocity analysis in Yung-An Ridge (b) and Formosa Ridge (c), their locations are shown in (a) (Tu, 2010). The color level also clearly displays the velocity image on the profile.

3.3 1-D fluid migration rates: *Péclet Numbers* analyses

Basically, in static state, the local geothermal gradient should be constant if there's no fluid involved to influence the temperature field. The heat transportation only relies on a deeper source (e.g. mantle) to spread the heat and cause the temperatures decrease at shallower depths (Fig. 3-2a). In another word, the changes of geothermal gradients in temperature fields might give us an important message of the disturbance from fluid flow (Fig. 3-2b). So combining the hydrological theory of the transport phenomena study in temperature fields, we successfully applied a new method to calculate regional 1-D (vertical) fluid flow rates by analyzing the ***Péclet Number***s of the geothermal gradient curves in steady state (Chen et al., 2011; Chen, et al., 2012).

3.3.1 Method: *Péclet Numbers* analysis

The ***Péclet Number*** is a dimensionless number defined as the ratio of the strengths of convection and diffusion in a physical quantity for the flow driven by an appropriate gradient (Patankar, 1980). We found that if the geothermal gradient systematically decreased with the increasing subbottom depth, it can be used to explain the 1-D static vertical upward fluid migration. To quantitatively study the effects of fluid flow on temperature fields, we analyzed the variations of regional geothermal gradients near BSR subbottom depths (100 - 700 m).

First of all, because Bredehoeft and Papadopulos (1965) considered the vertical

steady groundwater flow through the semiconfining layer of an aquifer system in which the temperature along a vertical section of the semiconfining layer has been measured at multiple points. These temperatures should satisfy the solution to the boundary-value problem describing following both heat and groundwater flow in the semiconfining layer (Fig. 3-3a):

$$\frac{\partial^2 T_z}{\partial z^2} - \left(\frac{c_w \rho_w v_z}{k}\right)\left(\frac{\partial T_z}{\partial z}\right) = 0 \qquad \text{(Eq. 5)}$$

Where:

(The boundary conditions $T_Z = T_0$ at $z = 0$; $T_Z = T_L$ at $z = L$ were applied)

T_Z = the temperatures at any depth z (m)

T_0 = uppermost temperature measurement (K)

T_L = lowermost temperature measurement (K)

z = the origin depth at T_0 temperature measurements (m) (positive downward)

L = length of temperature spreading (vertical distance between T_Z & T_0)

ρ_w = density of the fluid (kg/m^3)

C_w = thermal capacity of the fluid (J/kg K)

V_z = vertical fluid flow rate of the ground water (m/s)

After solving the equation 5**,** the ratios of $(T_Z - T_0)/(T_L - T_0)$ could calculated from measured temperature data, and plotted against the depth factor z / L at the same scale for fitting the curves. Here, we assume that the regional uniform vertical flow of both heat and ground water in a permeable layer (semiconfining marine sediments) would follow the same curve. So, after applying regional BSR-based temperatures in many different depths, the function $f(\beta)$ for defining the curve type was derived from the following equation (Fig. 3-3b):

$$f(\beta) = \frac{T_z - T_0}{T_L - T_0} = \frac{[e^{Pe(z/L)} - 1]}{e^{Pe} - 1} \quad \text{(Eq. 6)}$$

Where:

T_Z = the temperatures at BSR (K)

T_0 = the temperature at the top of a porous and permeable layer (K)

(We use the average seafloor temperature derived from in-situ measurement.)

T_L = the temperature at the bottom of the porous and permeable layer (K)

(Using trial-and-error to fit the regional curve, so we put as many BSR as we can for adding T_Z data constrain to improve the reliabilities)

z = the subbottom depth of the BSR (m)

L = thickness of the porous layer (m)

(Using trial-and-error to fit the regional type curve, so we put as many BSR as we can for adding z data constraints to improve the reliabilities)

Pe = the ***Péclet number*** for the porous and permeable layer

*These parameters are also denoted in (Fig. 3-4)

So here, we assumed a homogeneous semiconfining (porous sediments) layer, and did not consider the effects of depth-dependent porosity and the changes of thermal conductivity. After combining the regional temperature data from BSR and average of shallower heat probe measurements (Fig. 3-4a) to plot the normalized temperatures (T_z- T_0 / T_L- T_0) at normalized subbottom depths (z / L) (Fig. 3-4b), we could fit a curve for local geothermal profile, which is used to indicate the fluid-transportation feature: ***Péclet Number*** (***Pe***). Moreover, Beardsmore and Cull (2001) indicated that ***Pe*** is related to the upward fluid flow rate:

$$Pe = \frac{\phi \rho_w c_w v_z L}{k} \quad \text{(Eq. 7)}$$

Where:

Pe = the ***Péclet number*** for the porous and permeable layer

$\boldsymbol{\Phi}$ = porosity of the rock

$\boldsymbol{\rho_w}$ = density of the fluid (kg/m^3)

$\boldsymbol{C_w}$ = thermal capacity of the fluid (J/kg K)

$\boldsymbol{V_z}$ = vertical velocity of the ground water; leakage rate (m/s)

$\boldsymbol{L}$ = thickness of the porous layer (m)

$\boldsymbol{k}$ = thermal conductivity of the porous medium or rock matrix(W/mK)

In other words, once we have derived the ***Péclet Number*** (***Pe***) and the thickness of the porous layer ($\boldsymbol{L}$) by fitting the curve with the depth-varying BSR-based temperature field, we can further estimate the vertical fluid flow rate ($\boldsymbol{V_z}$) like follows:

$$V_z = \frac{kPe}{\phi \rho_w c_w L} \qquad \text{(Eq. 8)}$$

We use water as the fluid, so the density ($\boldsymbol{\rho_w}$) is 1000 kg/m^3, and the thermal capacity ($\boldsymbol{C_w}$) is about 4186 J/kg K (Tao and Lee, 1993). According to Shyu et al., (2006), the thermal conductivity ($\boldsymbol{k}$) of the rock matrix in this region is1.2 W/m K, and the average porosity of the sediments ($\boldsymbol{\Phi}$) is about 0.3 (Lin et al., 2003).

The curves indicate that, under isotropic and steady-state conditions with no fluid flow (***Pe=0***), the geothermal gradient is linear and does not change with depth (Fig. 3-2a). Here we supposed the fluid flow might comprise methane gas and water. The normalized geothermal profile of $\boldsymbol{f}$ ($\boldsymbol{\beta}$) against $\boldsymbol{z / L}$ is bending upon the fluid flow involved, and it will become convex and concave when the fluid upward and downward movement in the sediments (Fig. 3-2b). And the curvature of the geothermal profile increased with increasing fluid flow rate ($\boldsymbol{V_z}$), here we defined the $\boldsymbol{f}$ ($\boldsymbol{\beta}$) to stand for regional 1-D fluid flow rate (Fig. 3-4b).

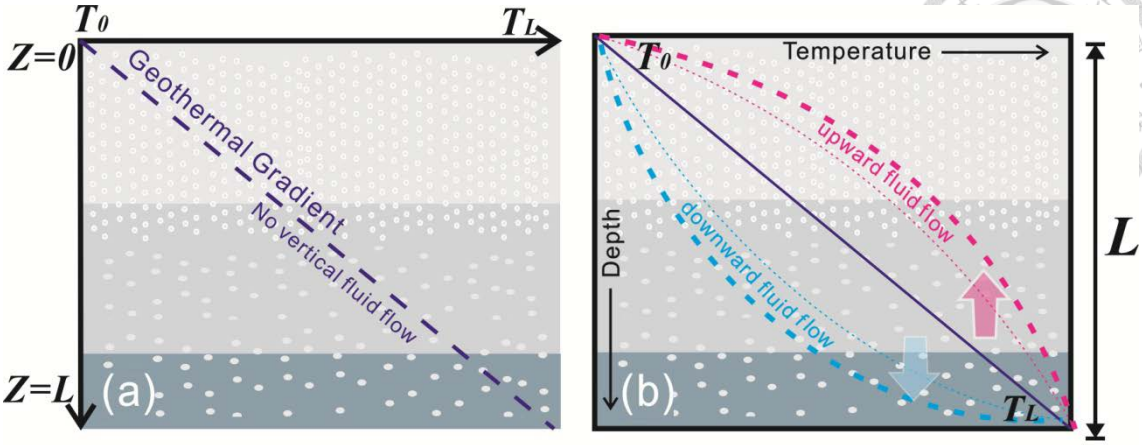

Figure 3-2 (a) shows a linear geothermal gradient with regular temperature change in static state and no fluid flow; (b) when the fluid flow is active and influences the temperature field in steady state, the geothermal gradient would become convex and concave when the fluid migrates upward and downward in the sediments, respectively.

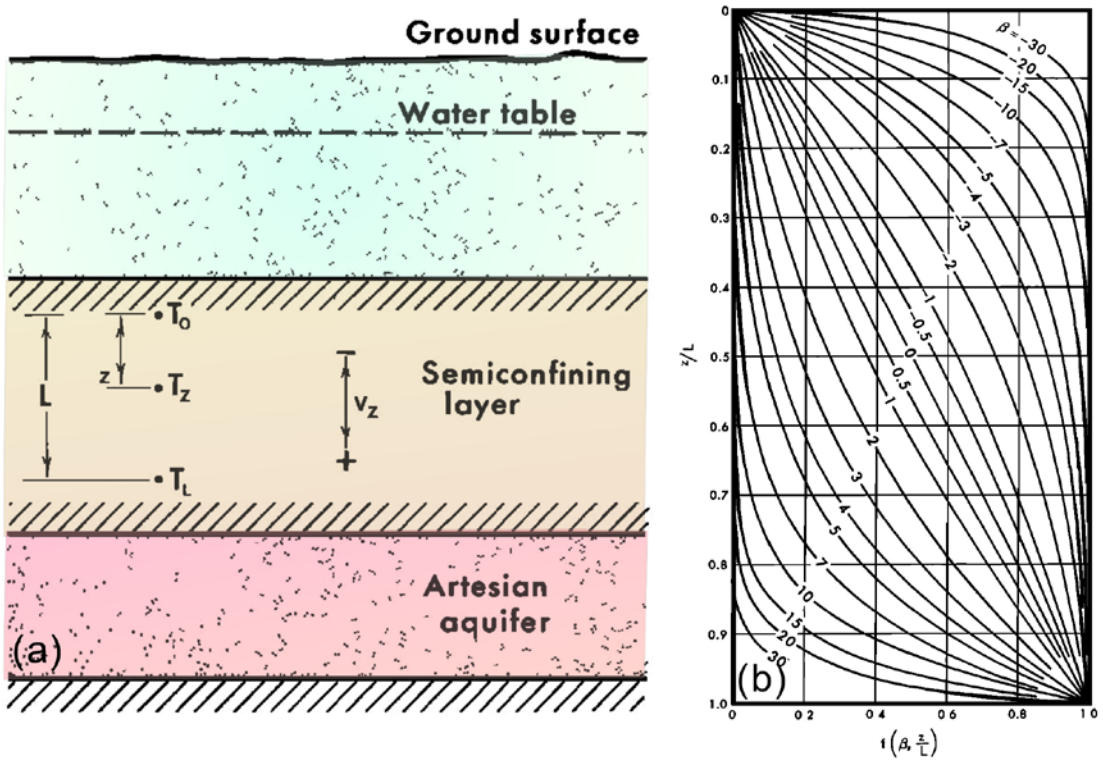

Figure 3-3 (a) is a diagram sketch of typical aquifer, which T_0, T_Z, T_L are measured temperatures, and V_Z is the leakage rate. (b) shows the type curves of the function which derived from equation 6.

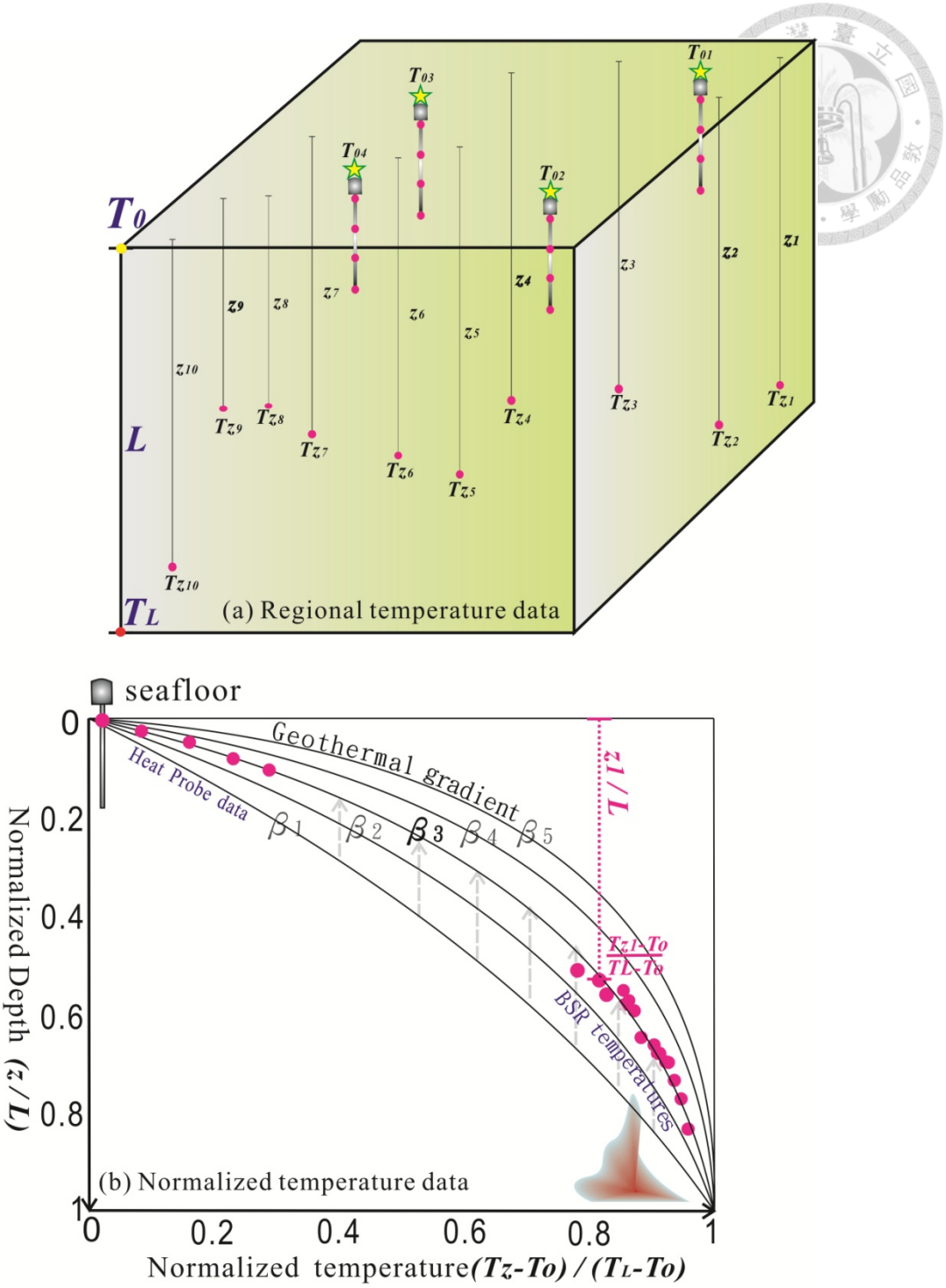

Figure 3-4 (a) is a sketch describing how we dominate the temperature data to our chart. We used the average of in-situ measured seafloor temperatures ($T_1 \sim T_4$) as T_0, then assumed a bottom depth and its temperature of this aquifer as L and T_L, and collected the temperature records from BSR ($T_{Z1} \sim T_{Z10}$) at their depths $z_1 \sim z_{10}$. (b) We could derive a curve of the function from BSR-based temperatures after mapping normalized data into a diagram, which depicts the regional fluid-transportation features, ***Péclet Number*** (***Pe***).

3.3.2 Results of 1-D fluid migration rates

By fitting the geothermal patterns in shallow crust which derived from the regional temperatures information (in-situ measurements and BSR-based), we obtained some local characteristics. Such as the ***Péclet Number*** (***Pe***), thickness of the semiconfining layer in meters (***L***), and the bottom temperatures of the semiconfining layers in degrees ($\boldsymbol{T_L}$) offshore SW Taiwan. We then convert the ***Péclet Number*** (***Pe***) to calculate the vertical fluid flow rates ($\boldsymbol{V_z}$). Generally, the semiconfining layer (***L***) are thicker in the upper slope domain and in subduction to initial collision zones, but get thinner in the continental shelf. The temperature differences between the seafloor ($\boldsymbol{T_0}$) and the bottom of the semiconfining layer ($\boldsymbol{T_L}$) controlled the fluid flow rate in most regions.

We first investigated the evolution of geothermal patterns by studying the fluid flow rate models near the trench from subduction zone to collision zone (white squares in Fig. 3-5); we also studied a transaction in the collision zone from the incoming passive margin to the active margin (black squares in Fig. 3-5). And we tried to derived geothermal patterns on 11 gas hydrate prospecting sites which have more temperature constrains (measured form long cores) in tens meters beneath the seafloor (squares of A to K in Fig. 3-5). The squares of Fig. 3-5 show how many temperature data points are used for our calculation of regional fluid flow rates. Sometimes we have to enlarge the area to include more data points for improving our fits.

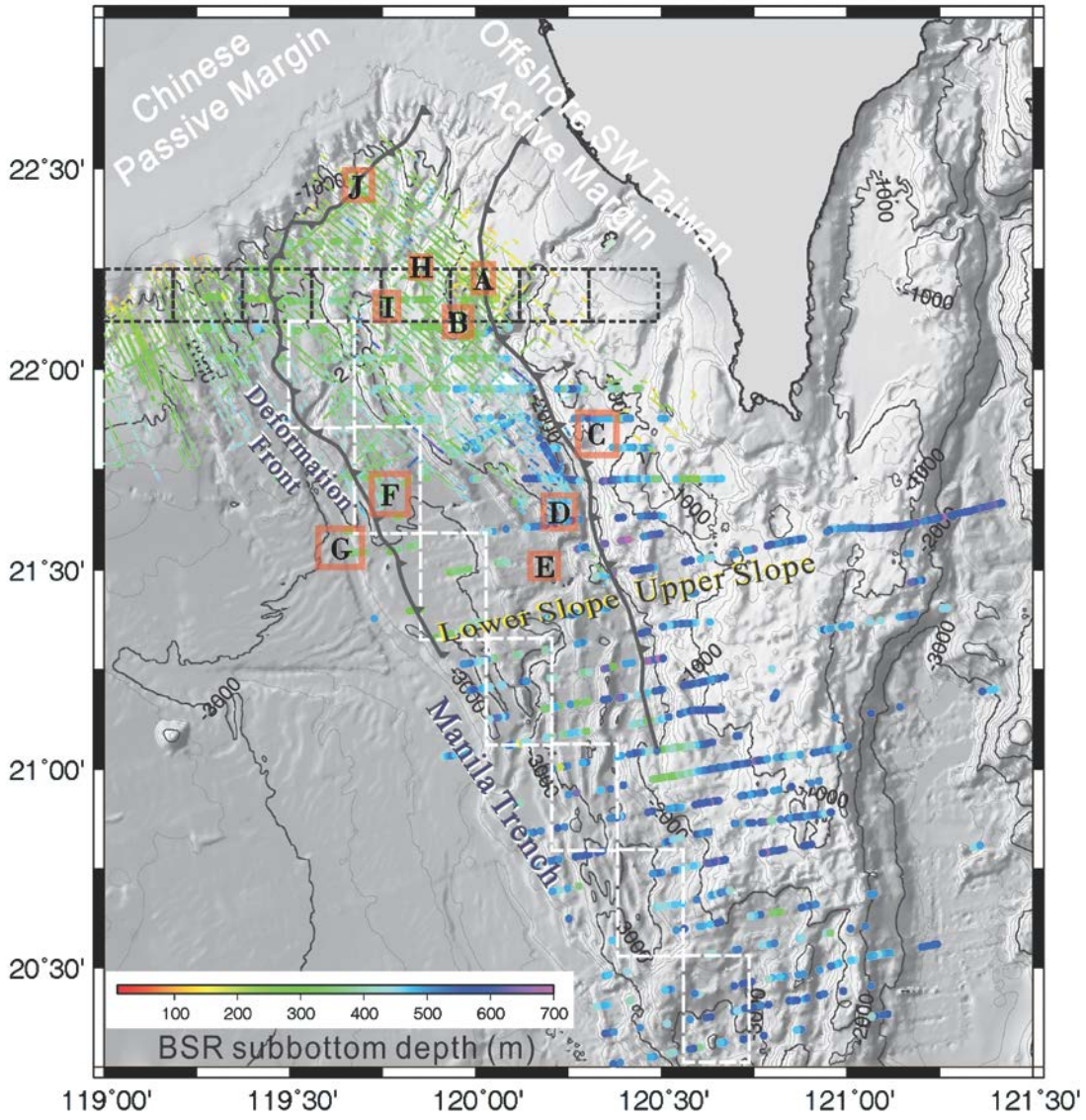

Figure 3-5 Squares show how many BSR-base temperature data points we could used as the reference for our 1-D fluid flow rate studies. We derived a sequence of regional geothermal patterns near the Manila trench from subduction zone to collision zone (white squares from south to north adjacent to the trench), and a transaction in the collision zone from the incoming passive margin to the active margin (black squares from west to east across the deformation front). And we also studied geothermal patterns on 11 gas hydrate prospecting sites which have more temperatures constrain in tens meters beneath the seafloor (see red squares A to J).

3.3.2.1 Result *1*: Evolution of fluid flow rates in offshore SW Taiwan

By fitting the geothermal patterns in shallow crust, we could derive these local characteristics at the same time. Furthermore, we used a box embracing all of our calculated values ($\boldsymbol{Pe}$, $\boldsymbol{L}$, $\boldsymbol{T_L}$, $\boldsymbol{V_z}$) to display the local characterizes, and for easier comparing regional results to each other (left of Fig. 3-6).

Owing to the relatively poor distribution of BSR distinguished from the seismic data along the trench, so we shift the range squares to eastern side of the trench and enlarge them to cover more BSR for better understanding the evolution of 1-D geothermal patterns from subduction zone to collision zone (Fig. 3-6). As a result, we found an increasing trend of the fluid flow rate from south (subduction zone) to north (collision zone). The average fluid flow rate is 10.5 cm/yr in the subduction to initial collision zone (Fig. 3-6, D-G). However, once the thick passive margin enters the convergent zone, the average fluid flow rate increased to 18 cm/yr (Fig. 3-6, A-C). And the vertical fluid rates accelerated as the dewatering increased, some may up to 24 cm/yr (Fig. 3-6, A). The results could be updated after more BSR data around the frontal ridge are collected, but the trend seems to be similar after we check the regional BSR-based temperatures.

Besides, the fluid flow rates in the collision zone also have dramatically changes from incoming passive margin to active margin (Fig. 3-6). Our results show relative low

fluid flow rates in the incoming passive margin (continental slope) (Fig. 3-7, A to C), ranging from 8 to 13 cm/yr. However, the fluid flow rate increases to 14-18 cm/yr once the passive margin sediments get incorporated into the fold and thrust belt of the lower slope domain (Fig. 3-7, D to F), i.e. enters into the east of the deformation front. The fluid flow rate then increases to 21 cm/yr near the boundary of the lower and upper slope domain where there are several a submarine canyons (Fig. 3-7, G). The fluid flow rate then decreases to 8 cm/yr in the upper slope domain (Fig. 3-7, H).

In offshore SW Taiwan, we successfully developed a method to derive BSR-based temperatures at different subbottom depths to calculate regional 1-D fluid flow rates by using Péclet Number analysis (Chen et al., 2010; Chen et al., 2011). Though the absolute values still debatable, but the general trend of the spatial distribution of geothermal patterns seem reliable.

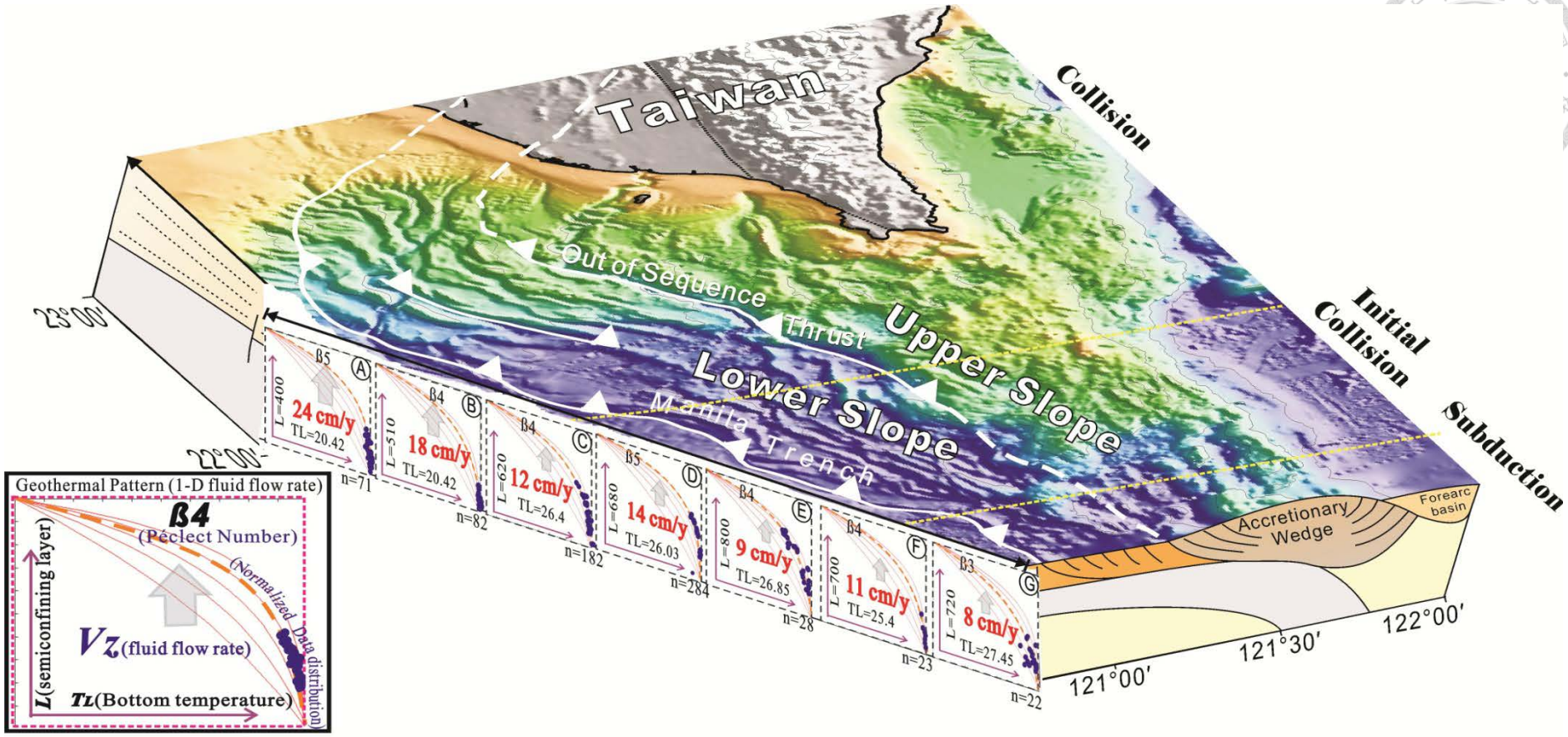

Figure 3-6 Derived regional geothermal patterns near the Manila trench from subduction zone to collision zone. We show the fluid flow rate along the trench in different boxes, and the box description is in left of this figure. The BSR-based temperatures at different depths are mapped to fit the Péclet Numbers (***Pe, β1~β5***) for each area. We found an increasing trend of the fluid flow rate from south (subduction zone) to north (collision zone). The spatial distribution of data used for analyses is shown in Figure 3-4.

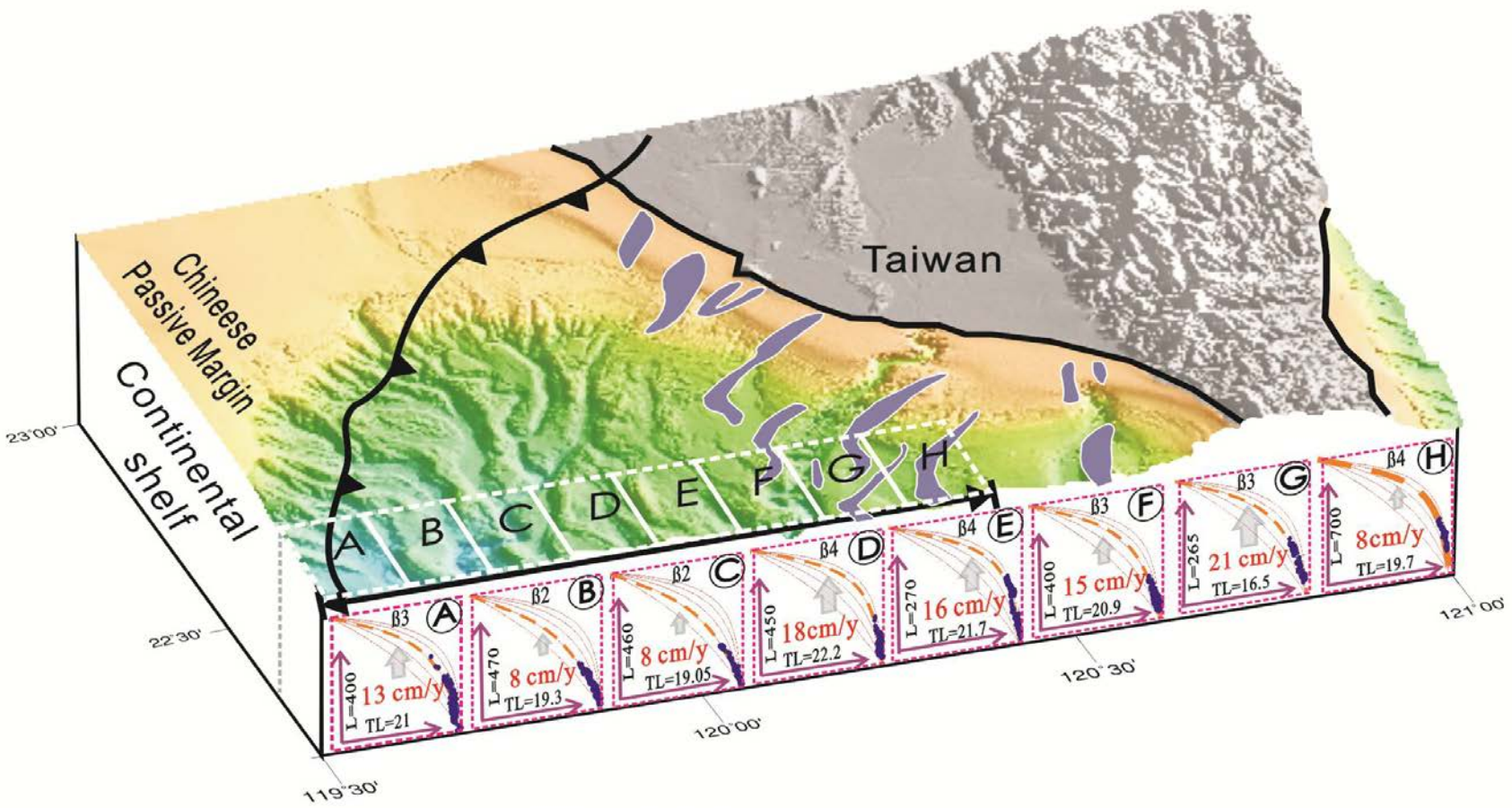

Figure 3-7 Derived a transaction of the fluid flow rates in the collision zone from the incoming passive margin to the active margin. Comparing the geothermal patterns from west to east, we found a dramatically changes of the fluid flow rates. The spatial distribution of data used for analyses is shown in the white squares of this map and Figure 3-4.

3.3.2.2 Result *2*: Regional fluid flow rates in offshore SW Taiwan

We have also studied some specific sites (Fig. 3-5, red squares A to J) where geophysical and geochemical evidence suggest more concentrated gas hydrate. Seventeen giant piston cores, some up to 35 meters in length, were recovered the temperature records and from these sites during a cruise of MD 178 by R/V Marion Dufresne. They provided us more temperature constraints of the shallow sediments southwestern Taiwan offshore, so we could add more temperatures data at more different depths to focus our fitting results within a smaller area. It's advantageous to apply fluid flow rate models from such vast amount of data for helping geophysical interpretation on gas hydrate prospecting sites offshore SW Taiwan.

We derived some regional vertical fluid flow rates at the prospecting sites. In the upper slope domain, we found very slow fluid flow rates (Fig. 3-8, C to E), which are consistent with the result we mentioned in previous section. On the other hand, there are several high fluid flow rates at the lower reach of Kaoping Canyon in the lower slope domain (Fig.3-8, A & B); they are both up to 28 cm/yr.

Adjacent the deformation front, there is a particular high fluid flow rate of 43 cm/yr (Fig. 3-8, J) in the upper reach of the Penghu Submarine Canyon, where a submarine landslide occurred. And there are two similar fluid flow rates just east and west of the deformation front (Fig. 3-8, F & G). The values are 16 and 15 cm/yr.

North of Yung-An Ridge, the fluid flow rate is about 23 cm/yr at site H; south of Yung-An Ridge, we combined three MD sites information to derive a regional fluid flow rate of about 18 cm/yr (Fig. 3-8, I & H). Since regional relief of Yung-An Ridge might strongly dominated the differences of fluid migration pattern, and it's also a hot spot with lots geophysical and geochemical data, so we divided it to night sub-regional parts to compare the 1-D fluid flow rates in different localities in Yung-An Ridge (Fig. 3-9, Y1 to Y9). The results range from 14 to 25 cm/yr; the highest rate is around the south center of the ridge near the blind thrust in the basin; and the lowest is close to the north end of the ridge.

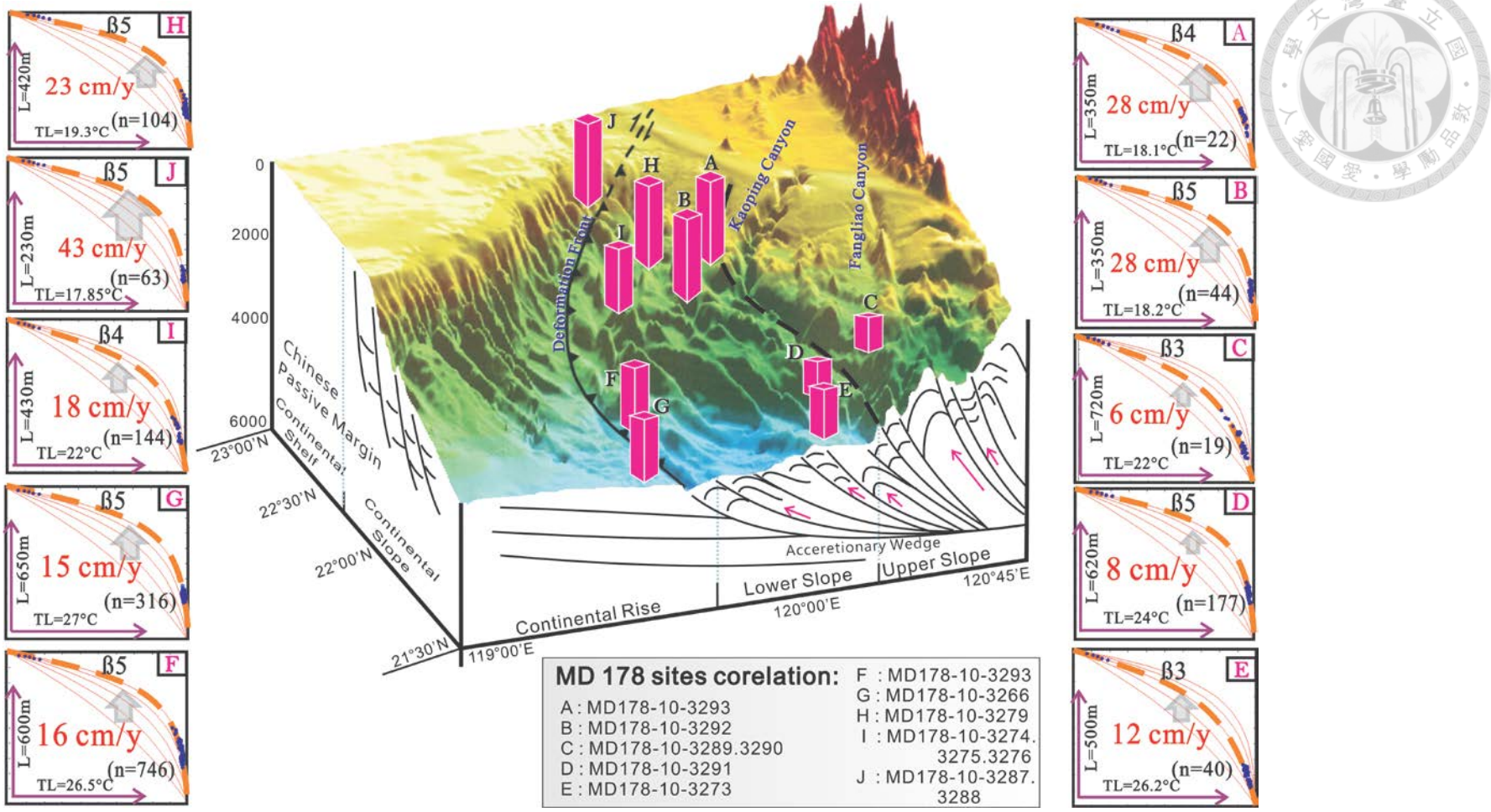

Figure 3-8 Derived 1-D fluid flow rates around the MD coring sites offshore SW Taiwan. The results are ranging from 6 to 43 cm/yr, which might induced by local structure but rough regions. We could still learn some general effects from comparing regions to each other.

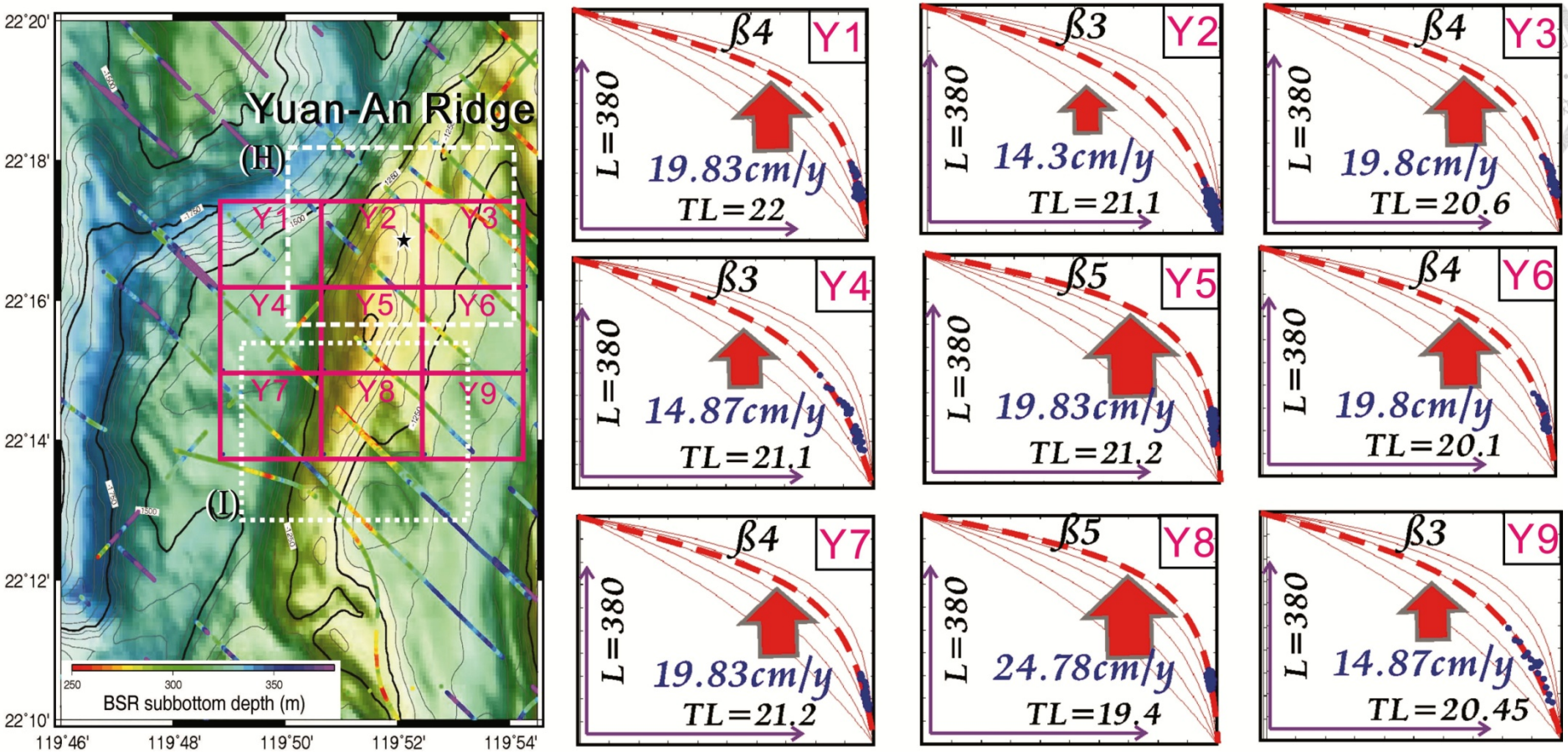

Figure 3-9 We derived sub-regional 1-D fluid flow rates in 9 parts of Yung-An Ridge to study more detail variation on fluid flow rates. The results range from 14 to 25 cm/yr. The purple squares show the spatial distribution of the BSR data we used, and the white dashed squares depict the areas of previous sites H and I in Yung-An Ridge (Fig. 3-8).

Chapter 4: Fluid Flow Migration Pattern Derived from BSR: 2-D and 3-D Temperature Filed Modeling on Pecube

Previously, we found a dramatic increase in vertical fluid flow rate when the continental slope of the China passive margin enters into the trench, and reduced fluid flow rates in the hinterland (Chen et al., 2012). Here, we selected several regions, which have dense seismic data as our simulation targets, to compare the 2-D and 3-D fluid migration patterns.

4.1 Temperature Field Modeling: Differential and Finite-Element Equation

The finite element method (FEM) is a numerical technique for finding approximate solutions to boundary value problems for differential equations. In order to study the influence of the evolving topography on the temperature field in the crust/ lithosphere, Zienkiewicz (1977) applied the finite-element equation to evaluate the temperature change using the heat transfer equation:

$$\rho c\left(\frac{\partial T}{\partial t}\right) = \frac{\partial}{\partial x} k \frac{\partial T}{\partial x} + \frac{\partial}{\partial y} k \frac{\partial T}{\partial y} + \frac{\partial}{\partial z} k \frac{\partial T}{\partial z} \qquad \text{(Eq. 9)}$$

Where:

t = time of past years

T = temperature at x, y, z (locations and depths) of the cube

$\partial T/\partial t$ = temperatures change as time

ρ = the rock density (kg/m^3)

k = thermal conductivity of the porous medium (W/mK)

c = thermal capacity of the fluid (J/kg K)

Usually, for understanding how surface topography affects the thermal structures of the uppermost crust, the top of the model was assumed as the geometry of the surface on earth, and the temperature of the surface (T_0) were determined measurements (Zeitler et al., 1987). Thus we could derive the temperature field related with the rock density and heat capacity from Eq. 9.

Here, we assumed a steady-state form for this equation ($\partial \mathbf{T}/\partial \mathbf{t} = 0$), meaning that the temperature (T) will not change with time (t), Bathe (1982) addressed that variations on temperatures are linear in all directions within each element in the model based on FEM of heat transfer equation (Fig. 4-1). Considering only conductive heat transferring in the crust, we used this approach on Eq.9 to model our background temperature. And this solution could be solved for a given the boundary conditions (b1 to b3) (Fig. 4-1):

$$T_0 = T\,(x, y, z = 0) \quad \text{(b1)}$$

$$T_L = T\,(z = -L) \quad \text{(b2)}$$

$$\frac{\partial T}{\partial n} = 0 \quad \text{(b3)}$$

Where the original of the coordinate (x, y, z, = 0) is one corner of the top boundary, and the top boundary of this model ($z = 0$) is the reference of surface elevation (eg. Seafloor), L ($z = L$) is the thickness of our simulation model; T_0 and T_L are the temperatures of the top and base boundaries, respectively; $\partial \mathbf{T}/\partial \mathbf{n} = 0$ indicates no heat exchange on side boundaries, while n is the outward normal to side boundaries.

For our conductive temperature models, we use high resolution bathymetry data as the top boundary of our model ($\boldsymbol{z = 0}$), and assign a constant seafloor temperature ($\boldsymbol{T_0}$), which is derived from the average measurement data (Shyu, 2013). Then the temperature of the model base ($\boldsymbol{T_L}$) could be determined by a given "geothermal gradient" multiplying with the model thickness ($\boldsymbol{L}$). After assuming there's no heat exchange along the side boundaries, we may successfully derive our model temperature fields. About the selection of geothermal gradient for our 2-D or 3-D modeling, we used a trial and error method, which we will discuss more in section 4.3.

Then we could analysis the temperature variation in 3-D cube (Fig. 4-2). Braun et al., (2004) noted that the temperature field beneath the escarpment shows how the surface topography affects the heat balance in the underlying crust (Fig. 4-2). Importantly, the isotherm follows the long-wavelength geometry of the escarpment, being deflected by up to a kilometer. This is because the temperature anomaly caused by surface topography decreases exponentially with a skin depth equal to the wavelength of the topographic signal (Carslaw and Jaeger, 1959).

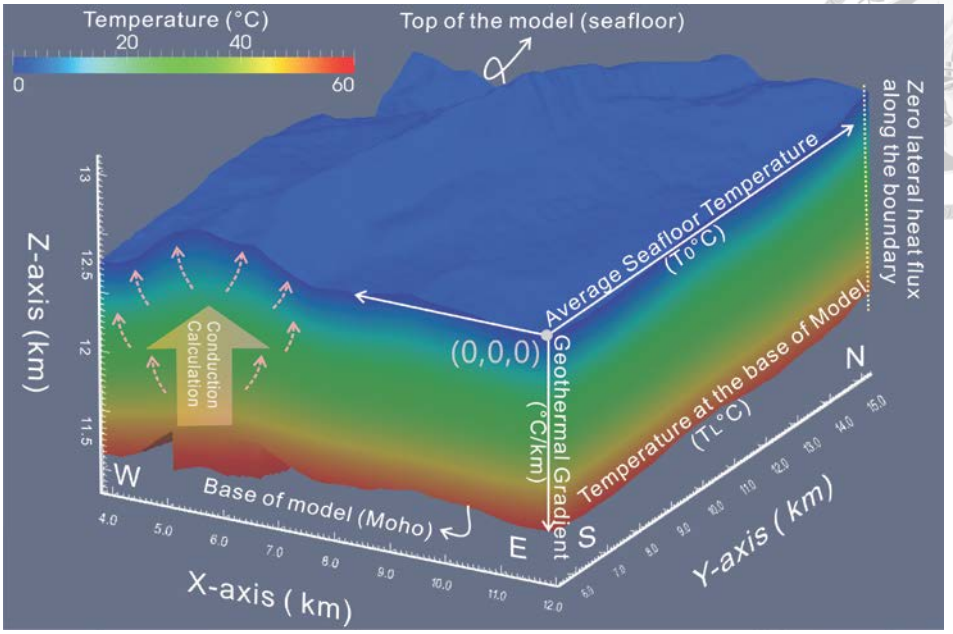

Figure 4-1 A diagram of our 3-D thermal model: The temperature varies linearly in all directions within each element in the model after applied the FEM on heat transfer equation under the steady-state. We assigned constant temperatures of ($\boldsymbol{T_0}$) and ($\boldsymbol{T_0}$) on the top (seafloor) and base (< Moho) boundaries of the model, while we assumed there are no heat transfer in and out of each sides.

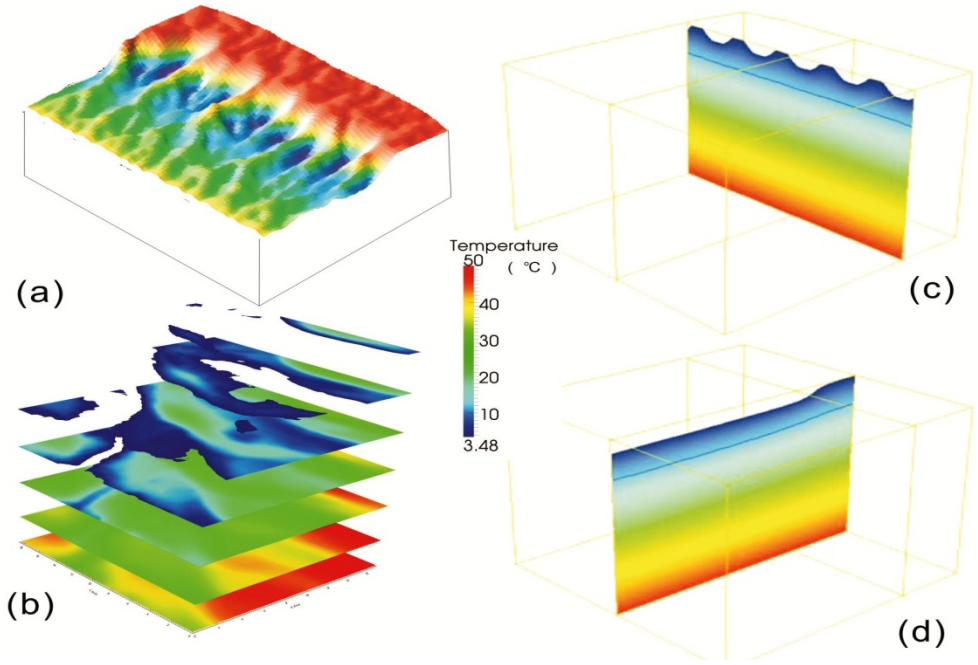

Figure 4-2 (a) Landform predicted from Pecube estimates; (b) the seafloor temperature is constant, then we could compute model temperature fields as the depth change; (c) and (d) are showing the computed model temperature fields runs draped underlying temperature along two orthogonal (modified from Braun et al., 2004).

4.2 A New Finite Element Code - Pecube

A robust finite-element code (**Pecube**) has been developed to solve the 3-D heat transport equation in a crustal/lithospheric block characterized by an evolving, finite-amplitude surface topography (Braun, 2003). The code is available downloaded from http://www.iamg.org/ CGEditor/index.htm.

Pecube has been developed as a user-friendly ForTran90 program. The user can easily build the 3-D temperature field through a detailed ASCII input file (***Pecube.in***) or by modifying the subroutines to create the input file (Fig. 4-3). It includes basic information such as the number of nodes, their horizontal coordinates, and some constant parameters. For ease of use, it is assumed that thermal properties such as rock conductivity, heat capacity, density and heat production are spatially uniform and constant through time; other parameters such as crustal thickness, basal temperature, surface temperature and lapse rate are also defined by the user.

For the digital elevation model used in the 3-D thermo-kinematic modeling, we used the water depth data (seafloor topography) collected during the cruises in recent decades. In our models in **Pecube**, we roughly use these thermal parameters for every region in offshore SW Taiwan: the average rock density of continental crust (***ρ***) is about 2700 kg/m^3 (Anderson, 1995); we defined the thermal conductivity (***k***) is about 1.156 W/mK according to the average measurement data (Shyu et al., 2006); the heat capacity

in lithosphere is about 516 J/kgK which is derived from the diffusion rate of silica (most of the lithosphere is silica) divided by the rock density (Holman, 2002). However, because this is a homogeneous model that is in steady-state, the results will not be dependent on these parameters; in other words, different parameters will not change the results of the temperature fields.

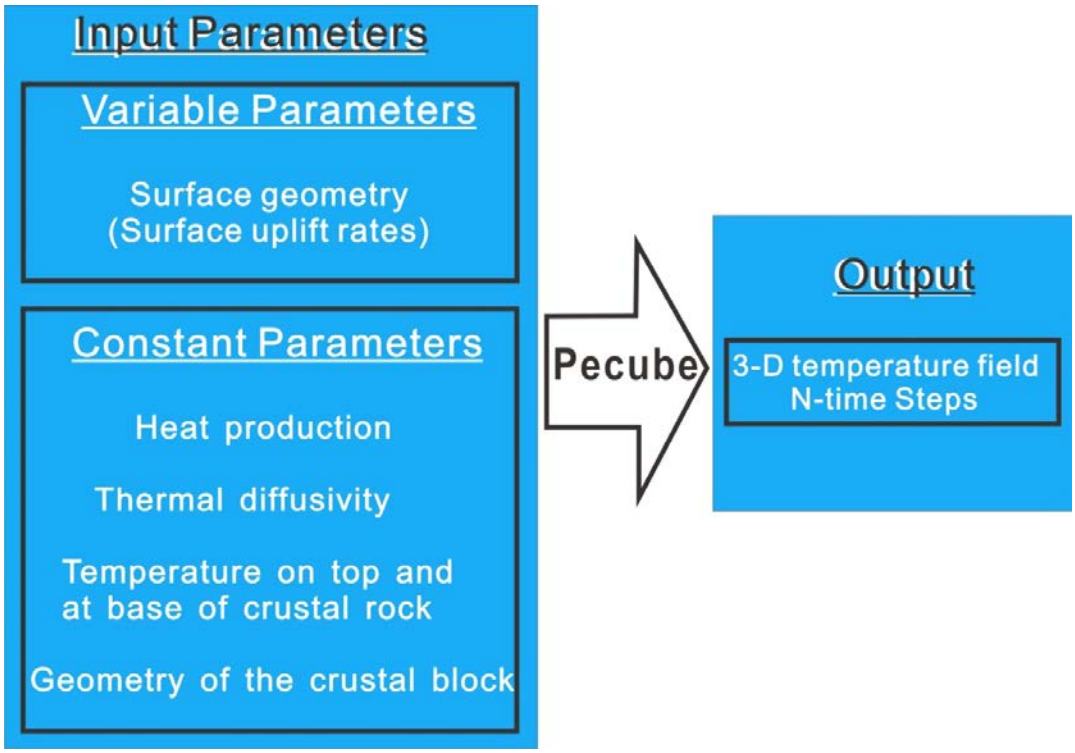

Figure 4-3 This flow chart describes various input options of **Pecube** as well as input parameters and output fields (modified after Braun, 2003)

4.3 Uncertainties in Defining Geothermal Gradient

When using **Matlab** or **Pecube** to calculate our conductive temperature fields from FEM, we have to use an applicable geothermal gradient to define the temperature at the model base. This is among the most challenge part of our 2-D/3-D simulations. In previous sections, we had defined the thermal parameters and applied the boundary conditions for our calculation. After that, we have to select a range of geothermal gradients, then we use the trial and error way to determine the proper geothermal gradient for a specific region. Usually, I decide the gradient from following sequences:

(1) First, we have to check the regional heat probe measurement results (Fig. 2-14) in study area. One is for the average seafloor temperature; another is to know the geothermal gradients in the shallow sediment as reference, though the shallow geothermal gradients are not necessarily to be consistent with that of the deeper ones.

(2) Moreover, we need to consider the thickness of the model (***L***) when we choose a proper geothermal gradient. The bottom of the model should not be deeper than "Moho". On the other hand, it is also important to choose a proper ***L*** that is large enough, otherwise it will force the deeper isotherms abruptly become flat at the base of the model due to the boundary condition. Based on our experience, the isotherms in our models usually became flat at the depth around 9 km based on different geothermal gradients; and the basement offshore SW Taiwan is about 15km according to the

tomography models derived from OBS (Fig. 4-4) (McIntosh et al., 2005; Yan et al., 2001).

(3) In addition, if we have horizontal isotherms at shallow depths of the model that is consistent with the flat topographic region, it is the most helpful clue for us to decide our geothermal gradient. I considered that since there is no topographic effect in the flat region, the BSR-based isotherm should be similar to that of the conductive numerical models (Fig. 4-5).

(4) Furthermore, we will choose a geothermal gradient that will give smaller temperature discrepancies between the BSR-based temperature and the model temperature (Fig. 4-6).

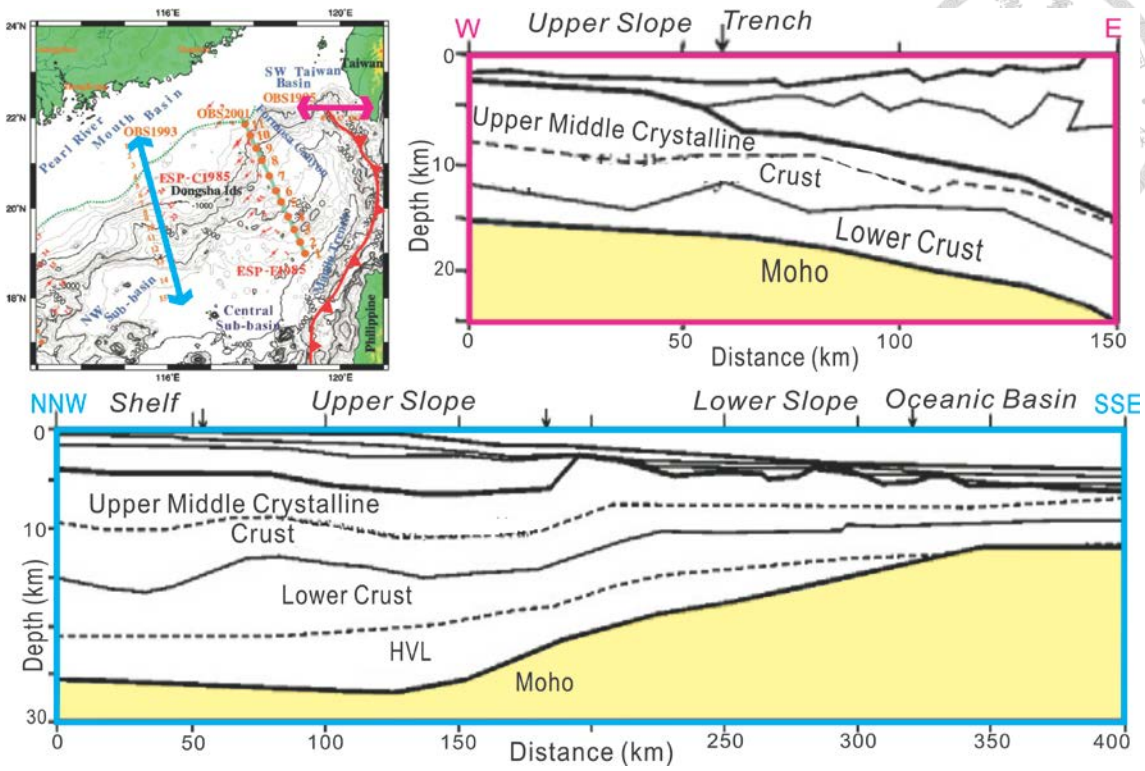

Figure 4-4 According to the velocity structure profile derive from OBS seismic images in northeastern South China Sea (Blue, Yan et al., 2001) and offshore SW Taiwan (McIntosh et al., 2005), we limited our model base to be less than 15 km. (modified from Wang et al., 2006)

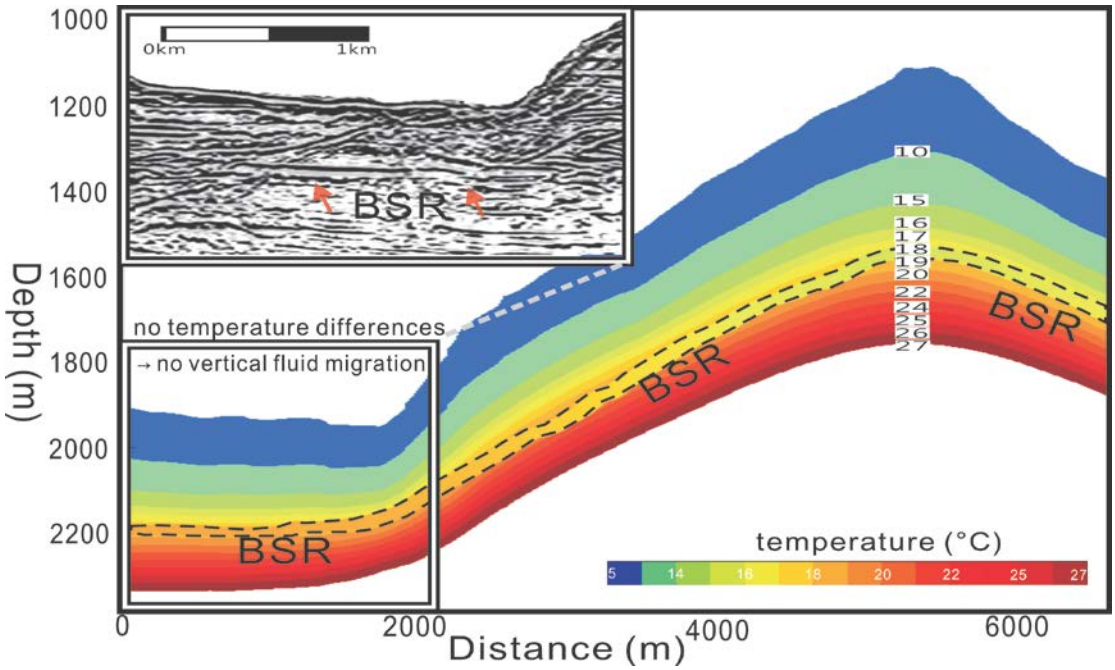

Figure 4-5 An example of choosing a proper geothermal gradient for the numerical model in Formosa Ridge. When we found a good match between BSR-based and model temperatures at west of the ridge, we always chose this gradient as our simulation parameter to study the discrepancy of the temperature field.

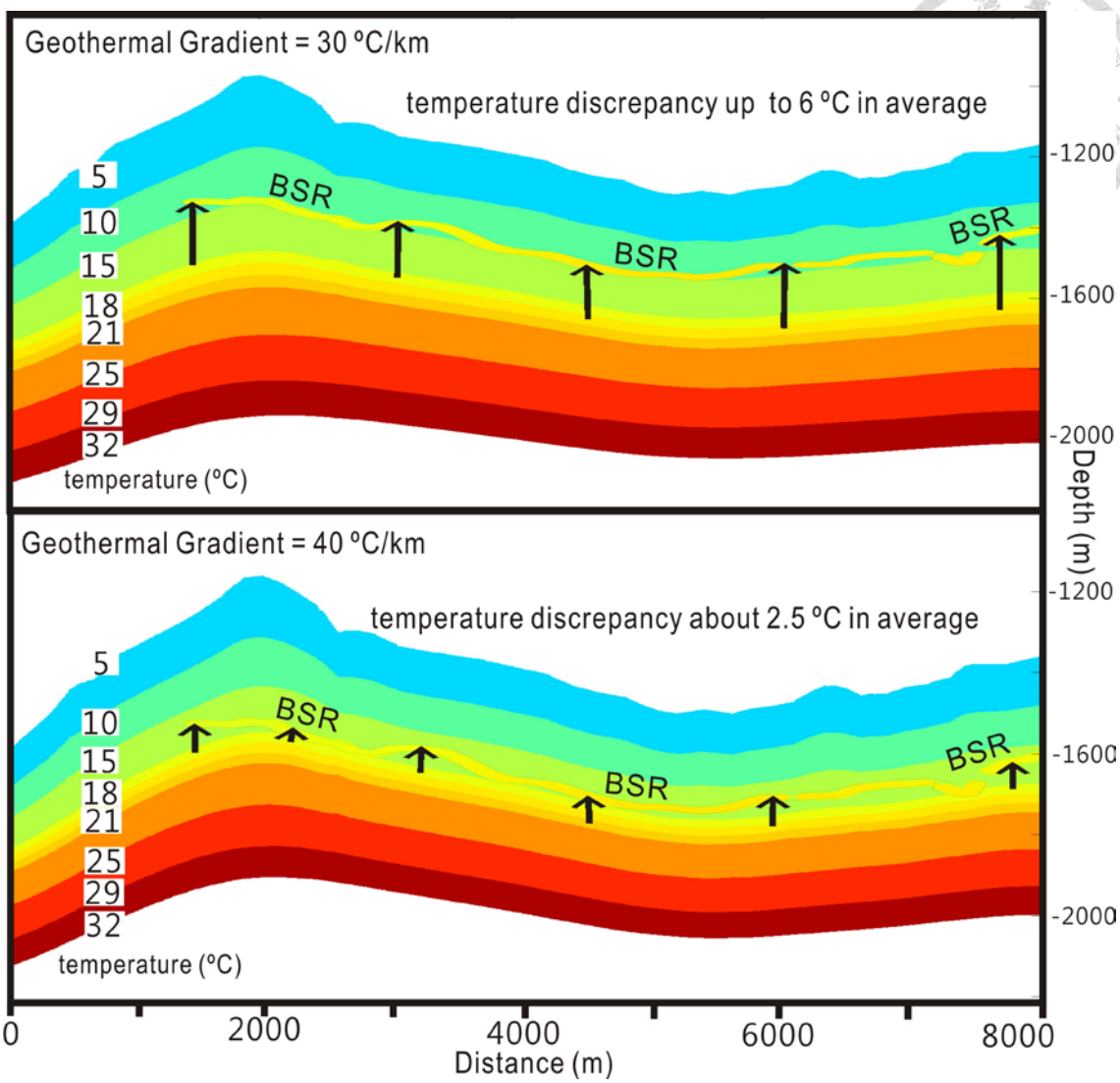

Figure 4-6 Geothermal gradients strongly controlled our model temperature fields. Here we used 30 ℃/km and 40 ℃/km, the examples in east Yung-An Ridge, the temperature found the temperature increased 6 and 2.5 ℃ respectively. We pick a geothermal gradient that will reduce discrepancy of the temperature fields (bottom).

4.4 Results: Temperature Discrepancies in Different Regions

After converting the BSR-based temperature (T_{BSR}), we compared it to our model temperature field (e.g. Fig. 4-6). We then analyzed the temperature discrepancy in depth profiles and showed on mapview for every case. In depth profiles, we combined the 2-D seismic profiles and temperature fields to see which structures are associated with the temperature discrepancies (e.g. Fig. 4-6), then to discuss the possible processes causing them. On mapview, we displayed the temperatures at BSR depths, which are derived from numerical models and BSR respectively. We want to see the regional trend of temperature anomalies.

4.4.1 Result 1: Deformation Front Vicinity - Penghu Canyon

In the upper reach slope of the Penghu Submarine Canyon (Fig. 2-2), previous heat probe measurement shows the seafloor temperature is about 4.13°C, in the shallow sediments, the geothermal gradient and heat flow is about 73 °C/km and 83 mW/m^2 (Fig. 2-14); besides, the rate of vertical fluid flow here is up to 43 cm/yr (Fig. 4-8J; star mark at Fig. 4-7b & 4-9), which is the highest value of our estimate in offshore SW Taiwan. We defined the seafloor temperature and geothermal gradient as 4.13°C and 40 °C/km and modeled an area about 304 km^2 (18.1 × 16.8 km) (Fig. 4-7a).

As the topography change, the model temperature (at BSR depth) show dramatic increase from northwest to southeast (5 °C → 35 °C) (Fig. 4-7a; 4-9b), but for the

BSR-base temperatures are stay relatively stable and increase only (Fig. 4-9a). Temperatures derived from the model and BSR are not very consistent, so we derived the distribution of their temperature discrepancy to study the local process effecting on temperature fields (Fig. 4-9c). According to one of the seismic and temperature discrepancy profiles, we discovered large temperature drop around deformation front (DF of Fig. 4-8) and location J (Fig. 4-8a), as well as the long coring site with highly surface gradient change (Fig. 4-8a1) and vertical fluid flow (Fig. 4-8a2); Through the deformation front on mapview, we found that the temperature discrepancy abruptly change from positive (+10°C of BSR-based temperature with respect to the model temperature) in northwestern continental slope to negative (-10) in southeastern basin (Fig. 4-9c).

Except the northernmost of the deformation front of the upper reach of Penghu slope, the SEL lab has collected dense seismic data at the Frontal Ridge recently, so we could study the thermal effect in different regions along the deformation front vicinity.

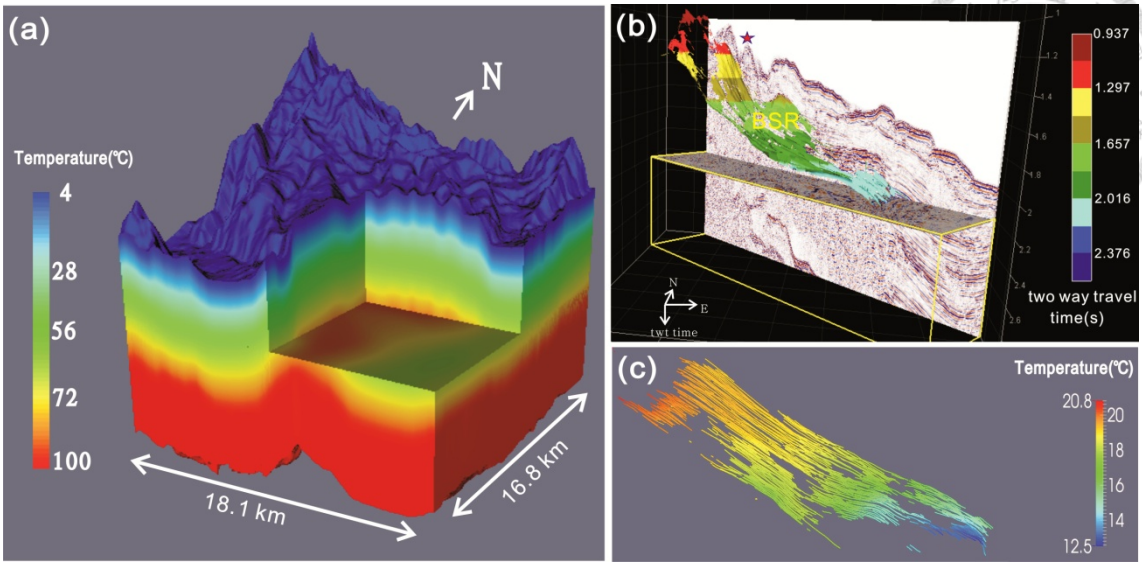

Figure 4-7 (a) 3-D model temperature field in Penghu upper reach slope; (b) BSR in 3-D seismic data (Liu, 2012); (c) BSR-base temperatures distribution here.

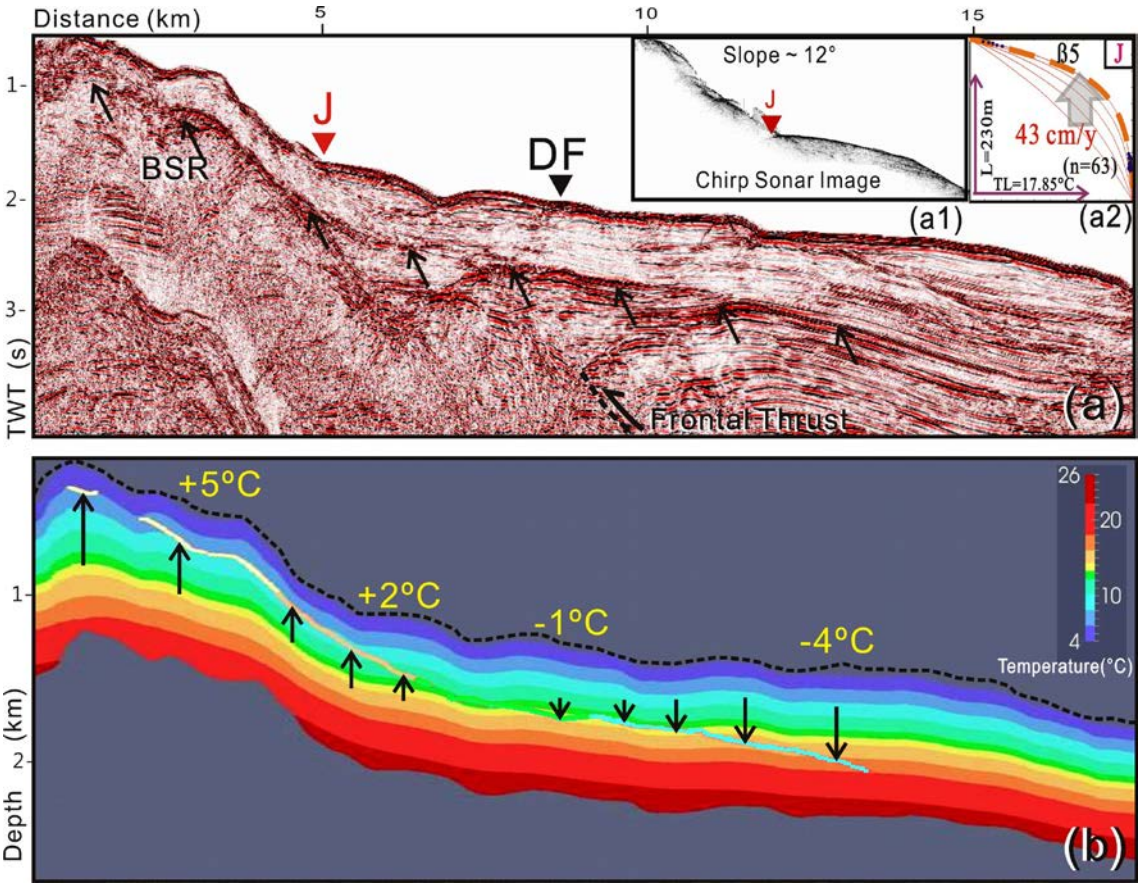

Figure 4-8 (a) In Penghu upper reach slope, an inline profile shows obvious changes on temperature discrepancies around deformation front (DF) and J site, with a highly change of the topographic gradient from chirp sonar images (a1) and vertical fluid flow rate (a2); (b) The background color scale is for our model temperature; arrows showed the discrepancy of BSR-based and model temperatures. (Han et al., 2012)

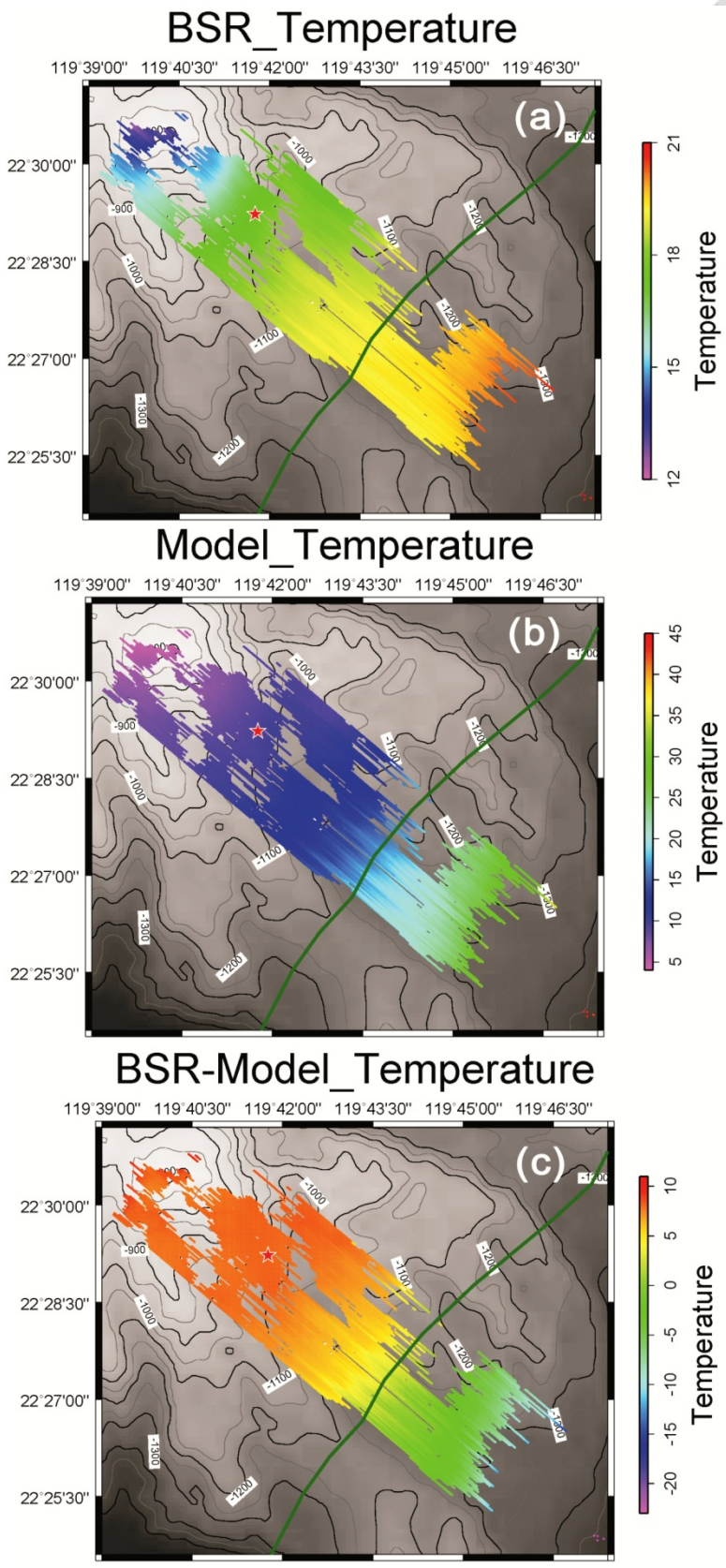

Figure 4-9 At the depth of the BSR in Penghu upper reach slope, we use (a) BSR temperatures subtracted (b) the model temperatures to derive (c) the temperature discrepancy field. The red star and green line mean the J site and the DF.

4.4.2 Result 2: Deformation Front vicinity – Frontal Ridge

In the accreted sediment on our study region of Frontal Ridge, faults and fractures provide dipping porous fluid conduits for gas-charged fluid migration (Lin et al., 2013). Naturally, there are lots of BSR identified from the seismic data (Fig 4-10b; 4-12a), and it's undoubtedly an important prospect site for gas hydrate reservoir research (Liu, 2012). The heat flow measurements here is up to 70 m W/m^2 at about 4.3 mbsf (meters below seafloor), and we derived relative high 1-D fluid flow rate (up to 24 cm/yr) around this region in previous study (Fig. 3-6A).

Consulting the average result of the heat probe measurements, we used 2.61 °C and 60 °C/km as the seafloor temperature and geothermal gradient, respectively, to model the region of 250 km^2 in Frontal Ridge (18.1 × 13.9 km, Fig. 4-10a). The BSR-based temperatures are ranging between 23.5 and 25.6 °C, which are increasing trench-ward (Fig. 4-10c; 4-12a). But the model temperatures are decreasing from 37 to 15 °C (Fig. 4-12b). After superimposing the temperature discrepancy with the seismic depth profile, there is an increasing of temperature at the toe of the wedge up to 8 °C (Fig. 4-11). Also, the deformation front is like a boundary separating the temperature discrepancies from negative to positive (Fig. 4-12 c). Next we will study the regional thermal structures from active to passive margin.

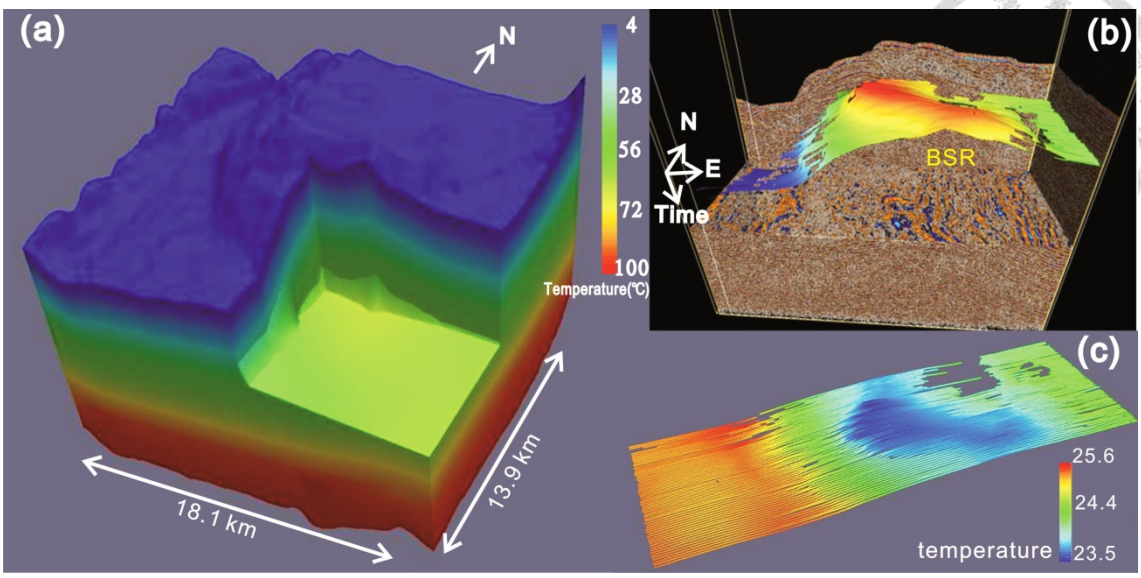

Figure 4-10 (a) 3-D model temperature field and (b) BSR distribution in 3-D seismic image in Frontal Ridge (Liu, 2013); (c) shows the distribution of BSR-base temperatures here.

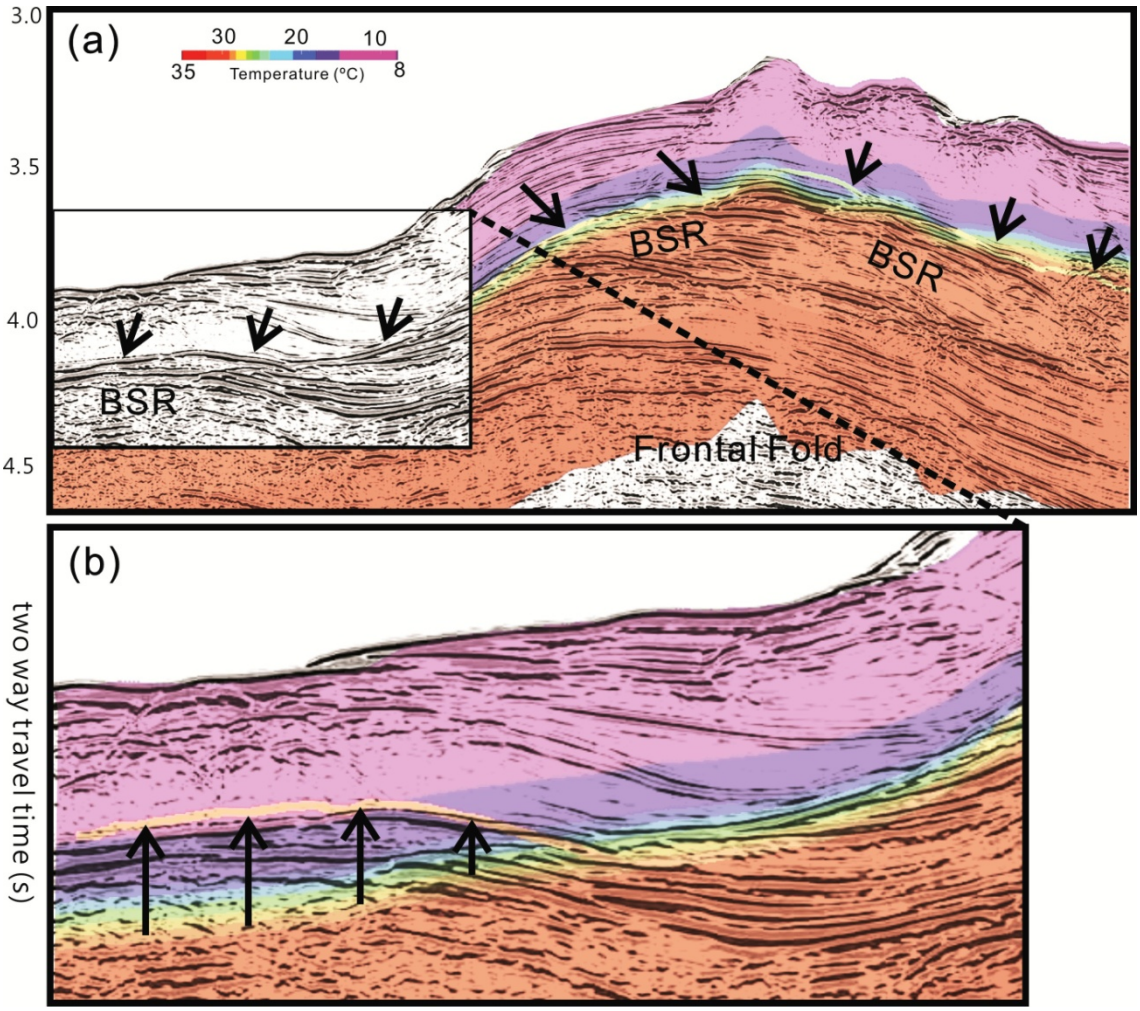

Figure 4-11 (a) The southernmost seismic profile with the temperature fields in Frontal Ridge, (b) we found the temperature increase at the toe of the wedge.

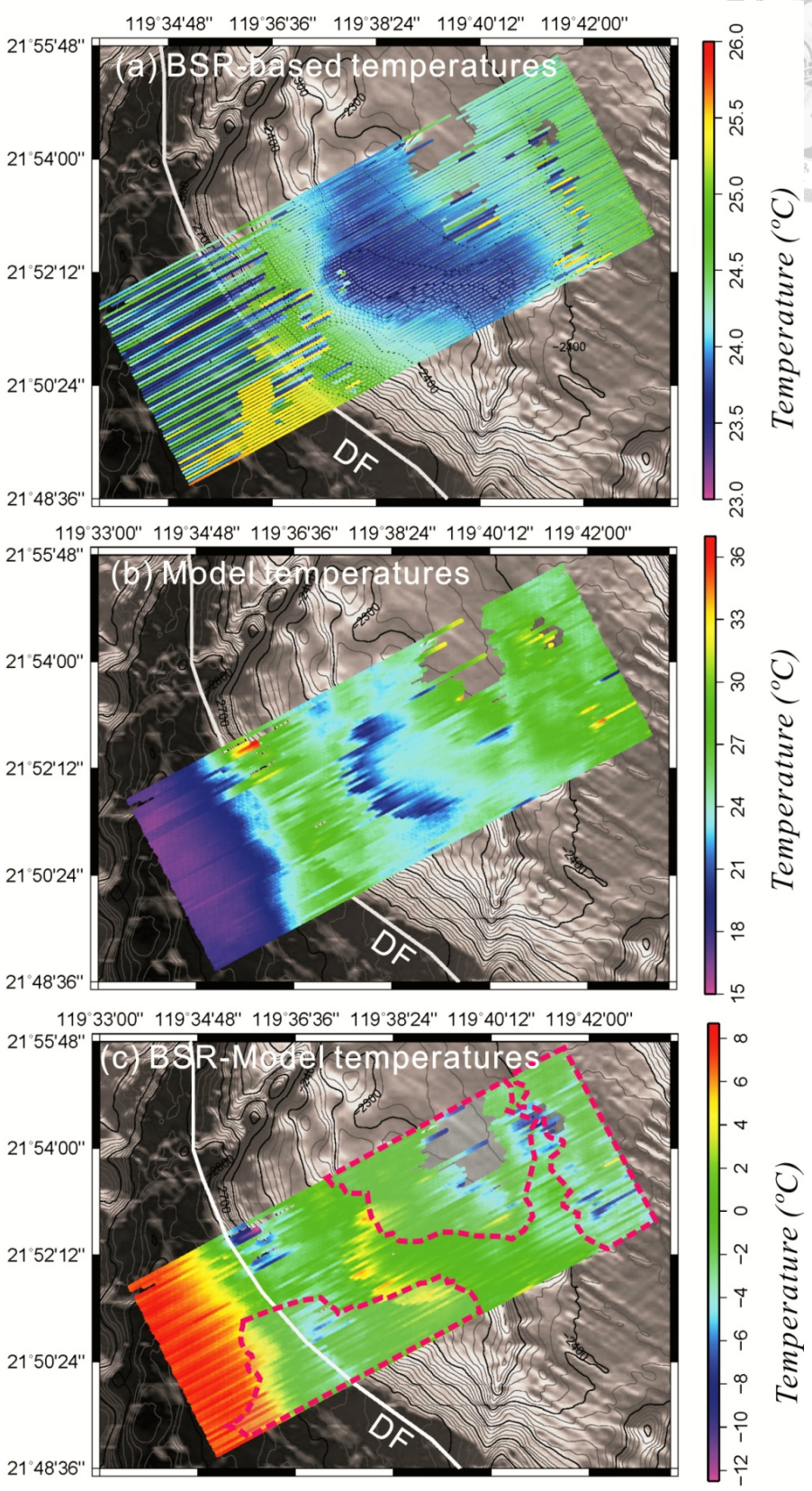

Figure 4-12 At the depth of BSR in Frontal Ridge, use (a) BSR temperatures subtracted (b) the model temperatures to derive the (c) temperature discrepancy field. The dashed red circles marked the paleochannels in this region (Lin, 2012a).

4.4.3 Result 3: Active Margin – Lower Fangliao Basin

In the upper slope domain of the accretionary wedge, there are several mud diapirs (Fig. 2-2; 4-13b; 4-14a) and anticlines (Fig. 4-15) in the lower Fangliao basin, and the BSR sometimes occurred continually (Fig. 4-13b.c). According to the heat probe data, the average seafloor temperature is about 3.48°C, and the geothermal gradient and heat flow is up to 85 °C/km and 99 mW/m^2 in the shallow sediments (Fig. 2-14). Moreover, Lin, (2011) found high concentration of methane (> 10^4 μL/L) and ethane (20 ~ 30 μL/L) by analyzing the pore water from a long (25 m) sediment core, then Yang, (2012) combined the carbon isotope of dissolve inorganic Carbon (DIC) to infer the methane flux here is 3.7 ~ 4.5 mmol/m^{2}yr (Fig. 4-15a). As well as, we had estimated the 1-D fluid flow rates here to be about 8-12 cm/yr (Fig. 3-8 D & E).

The area of our simulation model in Lower Fangliao Basin is about 102 km^2 (7.4 × 13.8 km) which covered the same area with the 3-D seismic data (Fig. 4-13a), and we chose the 32 °C/km and 3.48 °C as the geothermal gradient and seafloor temperature, respectively.

Next, we document the temperature and seismic profiles to the south (Fig 4-14): BSR in this region are hard to recognize inside of the diapirs (Fig. 4-13b.c), but they are more coherent around the diapir and show some local temperatures increasing (~ 2.6 °C) when the BSR extended into the diapir structure (Fig. 4-14b). Another temperature

increasing zone (increased ~ 2 ^{o}C) is in the eastern rim of the basin that has high amplitude reflections reflection just beneath BSR (Fig. 4-14c). From a northern seismic profile with temperatures information (Fig. 4-15), we found the BSR could even cross-cut the anticlines to be parallel to the seafloor as a result of the P-T condition (Fig. 4-15b).

Figure 4-16 showed the temperature distribution at the BSR depths, the BSR-based temperatures are generally around 17 ~ 21 °C, and the model's are about 14 ~ 22 °C, the temperature discrepancies ranges between -5 to +1.5 °C. In Fig. 4-16c, we derived more than one degree increase in anticlines and diapirs, for sediment waves around the east rim of the basin, the temperature discrepancies showed oscillating between increasing and decreasing temperatures from different inline profiles.

In opposition to the upper slope domain, the distribution of BSR is more focus and dense in the lower slope, especially in the fault bend folding ridges. As an example of Yung-An Ridge, it is a prospecting site with lots compressional structures and possible fluid pathways.

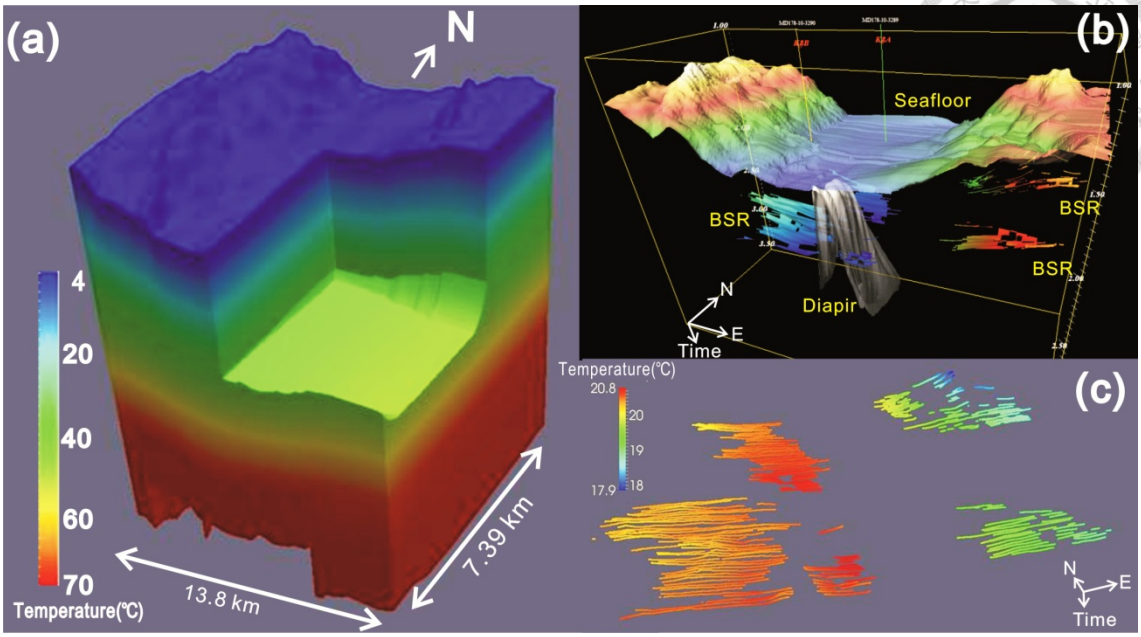

Figure 4-13 (a) 3-D model temperature field and (b) BSR distribution in 3-D seismic data in lower Fangliao Basin(Liu, 2012); (c) BSR-base temperatures field.

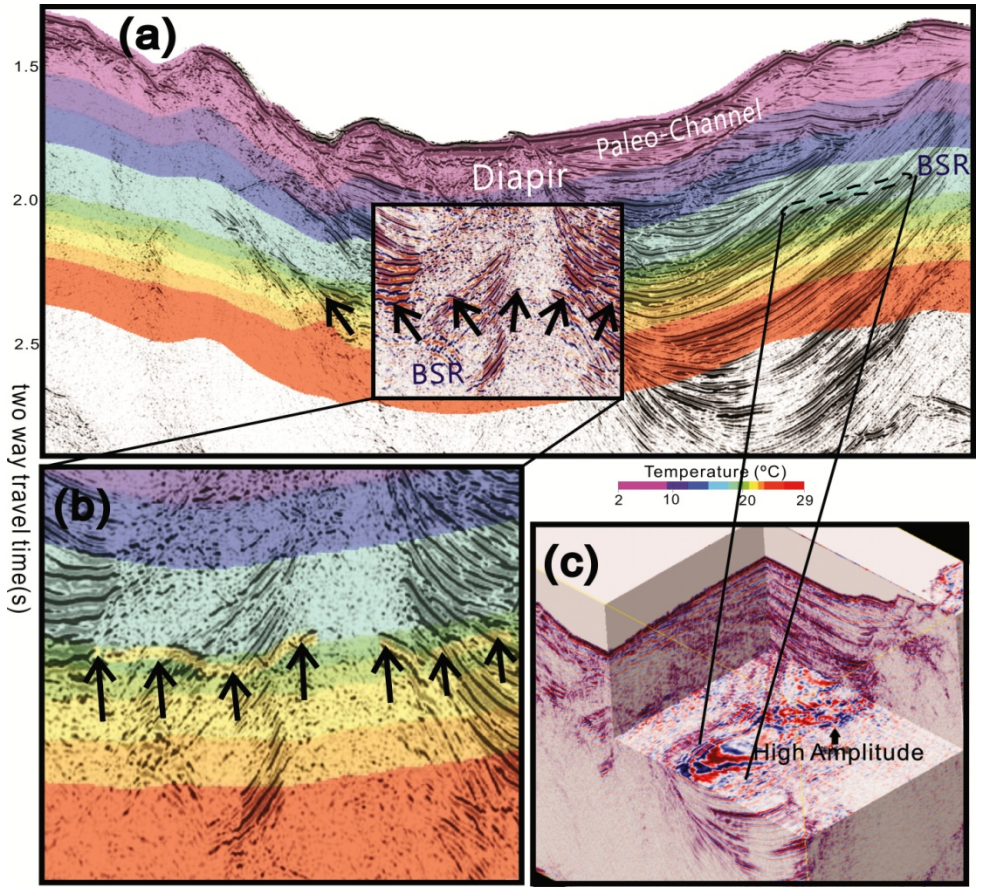

Figure 4-14 (a) An inline seismic profile with the model temperature field in lower Fangliao Basin; we found the raising temperature (b) around the diapir and (c) the basin edge, also note the high amplitude reflection in the time slice.

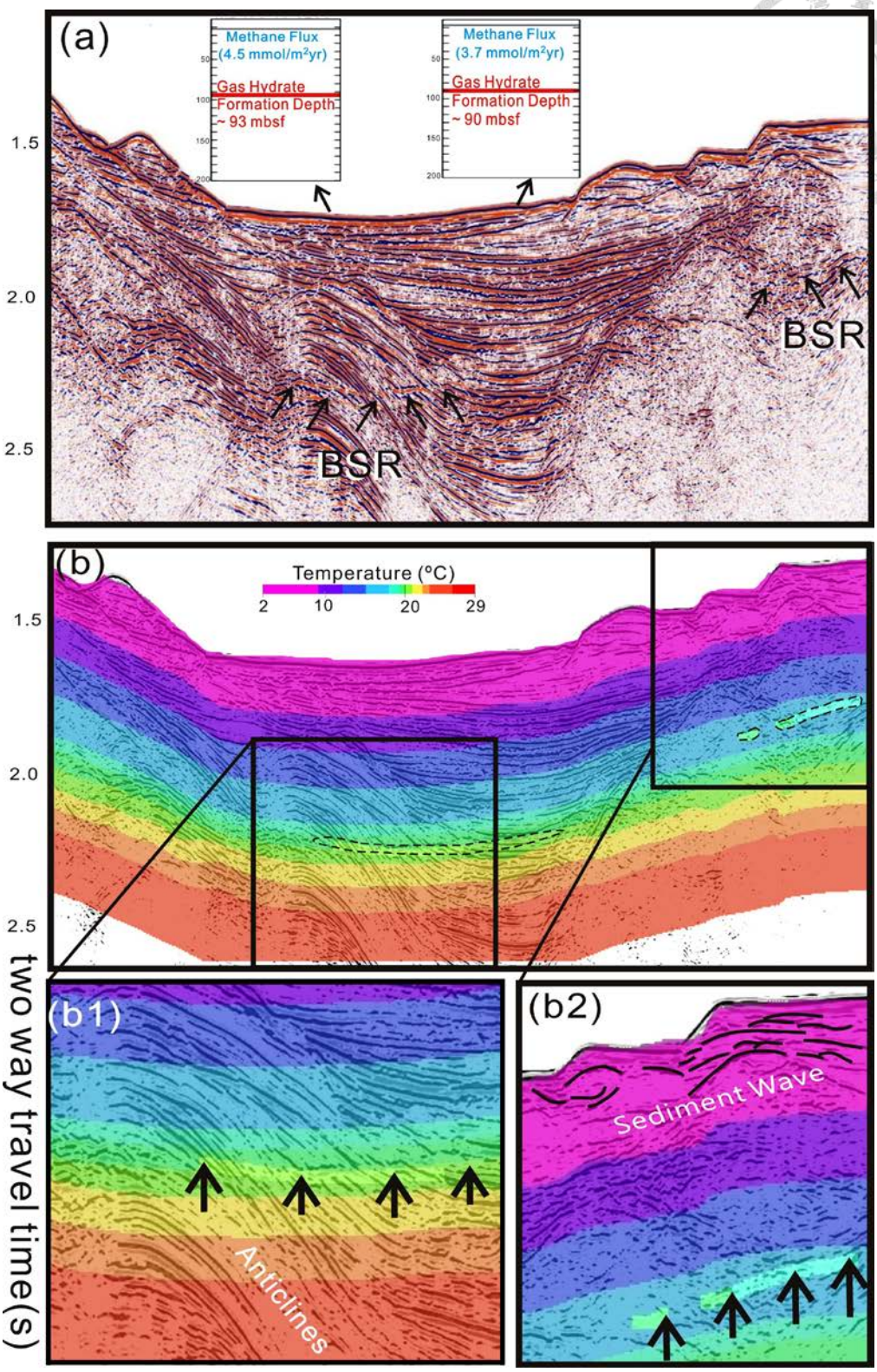

Figure 4-15 (a) One inline profile with anticlines and the geochemistry data derived from two long cores (25m) (Yang, 2012) (b) combining our model and BSR-based temperatures in the seismic profile to show the correlation of feature structures and the locations of temperature discrepancies.

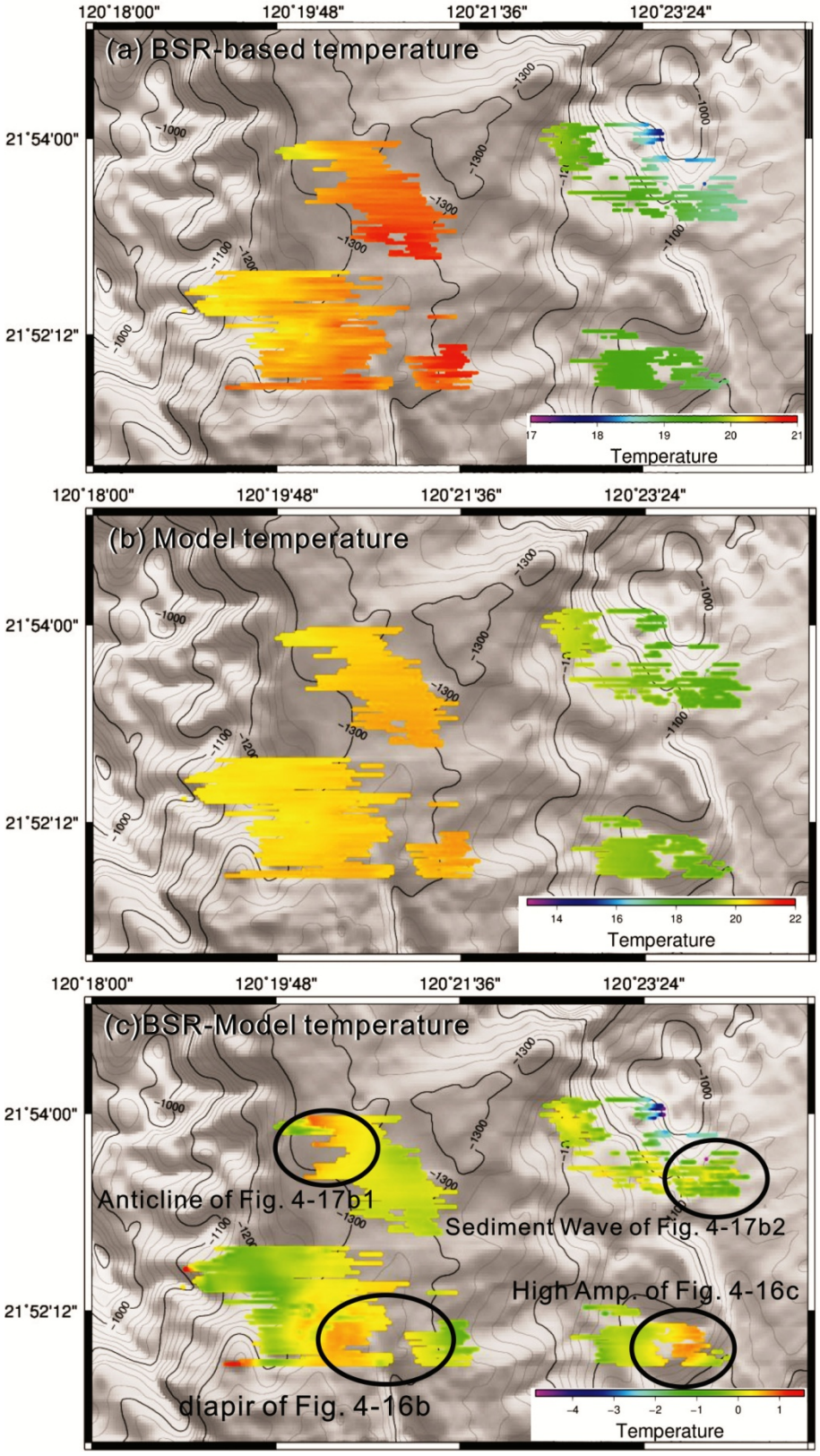

Fig 4-16 At the depth of BSR in lower Fangliao basin, the (a) BSR-based temperatures were subtracted by the (b) model temperatures to derive the (c) temperature discrepancy field. Note that the circles of (c) marked the locations with detail temperature and seismic images in previous figures.

4.4.4 Result 4: Active Margin – Yung-An Ridge

Yung-An Ridge is a particular research hot spot with large amount of geophysical and geochemical evidence to show that it's a good structure high to trap methane (Lin et al., 2008; Lai et al., 2009). According to 32 heat flow measurement results, the average heat flow is about 67 mW/m^2 (ranging from 35 ~ 107 mW/m^2), and four of them are over 100 mW/m^2 (Peng, 2012) (Fig. 2-9). Besides, the geothermal gradients and seafloor temperatures are ranging between 28 ~ 98 °C/km and 2.78 ~ 3.96 °C respectively (Fig. 4-17), so we used 3.89 °C and 40 °C/km as the model parameters for temperature simulating in Yung-An Ridge (Fig. 4-17).

There are three locations showing shallower BSR sub-bottom depths along the profiles, which show some temperature increasing in the sediments (Figs. 4-19 & 4-20): (1) under the west flank of the ridge near the west-vergent thrust that forms the folded ridge (at the distance less than 4000 m); (2) the higher amplitude BSR under the eastern flank (at the distance about 5500 m), where Yang et al., (2006) detected strong geochemical signals from methane concentrations and the shallow sulfate – methane interface (SMI); (3) near the fissures on the eastern side.

In northern transect of Yung-An Ridge (Chen et al., 2012), BSR-based temperatures are generally 2.1 °C higher than the model temperature field which translated to local geothermal gradient is up to 47.8 °C /km. There are higher

amplitudes of BSR occurred in the eastern ridge, so we calculated the vertical fluid flow rate for this small region. We also use the BSR temperatures from different sub-bottom depth to estimate the Péclet Number to examine the 1-D vertical upward fluid flow rates around the R1 site of the profile. We derived a high 1-D fluid flow rate up to 27 cm/yr here (Fig. 4-19a). And the highest temperature increase is in the eastern part of the basin with fissure structures. Note that there is a possible chimney in the east basin, which seems like a BSR gap along with a blanking zone below and velocity push down reflections above (Liu, 2009) (Fig. 4-19b).

In southern transect of Yung-An Ridge, the temperature profile (Chen et al., 2012) sowed BSR-based temperatures are on average 1.2 °C higher than the model temperature. Note that the temperature fields in east basin are very consistent between model and BSR-based values, but it is quite different in the northern profile in previous paragraph. The highest warming effect occurs in eastern flank of the ridge, where the regional temperature increased up to 3.1 °C (Fig. 4-20b). 1-D fluid flow rate here is about 34 cm/yr, which is higher than the northern profile. West of this anticlinal ridge under the slope basin, the topography is gentle but the BSR sub-bottom depth becomes much shallower. The temperatures increase about 2.2 °C (Fig. 4-20b).

The BSR-based temperature field in mapview ranges from 17 to 23 °C; the model temperature field is between 12 ~ 35 °C. The temperature discrepancies range between

-12 and +6 °C (Fig. 4-21. 4-22). Most shows increasing temperature except the northwestern region (Fig. 4-22a). The model temperatures in the northwestern region are higher (red in Fig. 4-21b) and it seems like a low topography region with steep slope away from the ridge (Fig. 4-22b).

We have studied some thermal structures of thrusts and folds region in the vicinity of the deformation front and the active margin regions, but we also studied the passive margin even though we have fewer datasets there. During the 2013 R/V Sonne cruise of TAIGER project, we have collected a P-Cable 3-D seismic data at Formosa Ridge on the passive margin. It provides us an opportunity to study the shallow crustal thermal structures in marine sediments of the passive margin, which will be documented next.

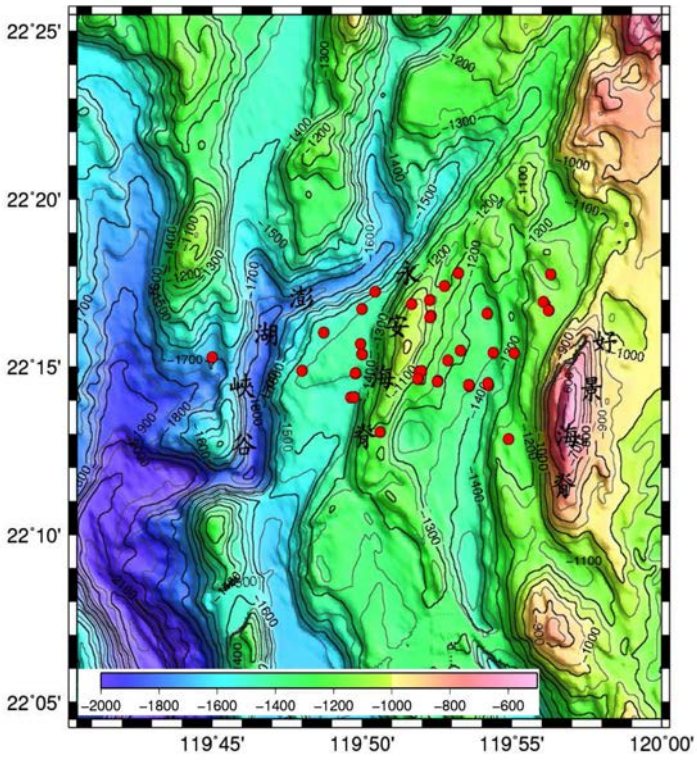

Fig 4-17 The 32 heat flow measurement data locations in Yung-An Ridge (Peng, 2012).

Table 1 The 32 heat flow data information in Yung-An Ridge (Peng, 2012)

Lon. (deg)	Lat. (deg)	T_0 (°C)	K (W/mK)	G (°C/m)
119.8813	22.2533	3.36	0.95	0.038
119.887	22.2967	3.59	NaN	0.028
119.8435	22.2177	3.49	1.33	0.054
119.8272	22.2348	2.88	1.17	0.059
119.8335	22.2563	3.18	1.17	0.057
119.8652	22.2478	3.77	1.21	0.059
119.8717	22.275	3.96	1.09	0.006?
119.8408	22.2873	3.15	1.2	0.029
119.8793	22.2902	3.28	1.27	0.065
119.829	22.235	2.78	1.12	0.07
119.8337	22.2562	2.86	1.07	0.063
119.8665	22.248	3.61	1.09	0.047
119.8718	22.2755	3.65	1.19	0.052
119.8713	22.2747	3.63	1.09	0.067
119.8755	22.243	3.48	1.1	0.032
119.9148	22.2142	3.43	1.03	0.037
119.9343	22.2823	3.82	1.29	0.028
119.9385	22.296	3.65	1.33	0.047
119.8753	22.2427	3.49	1.1	0.035
119.9038	22.2408	3.46	1.13	0.059
119.893	22.2405	3.89	0.98	0.034
119.8648	22.244	3.89	1.23	0.049
119.8298	22.2468	3.28	1.22	0.047
119.871	22.2832	4.24	1.22	0.052
119.9035	22.242	3.08	1.25	0.077
119.8928	22.2412	3.15	1.1	0.066
119.8645	22.2442	3.52	1.18	0.075
119.8298	22.247	2.96	1.09	0.064
119.8002	22.2482	2.91	1.22	0.043
119.9182	22.2568	3.13	1.13	0.095
119.9065	22.2572	3.18	1.01	0.098
119.8882	22.2582	3.36	1.21	0.063

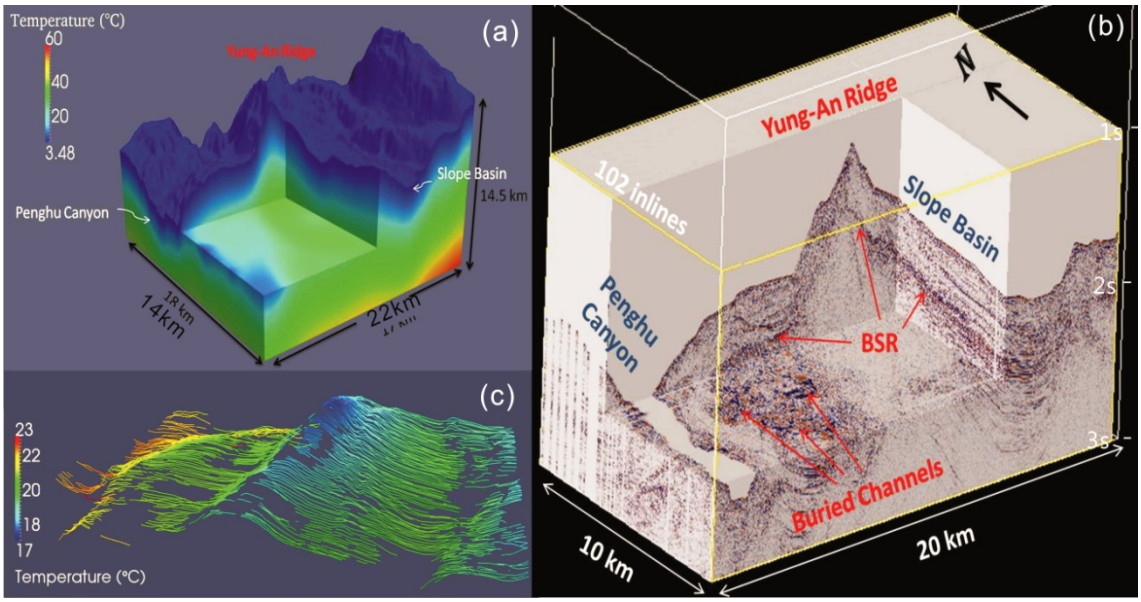

Figure 4-18 (a) 3-D model temperature field and (b) BSR distribution in 3-D seismic data in Yung-An Ridge (Liu, 2011); (c) BSR-base temperatures distribution.

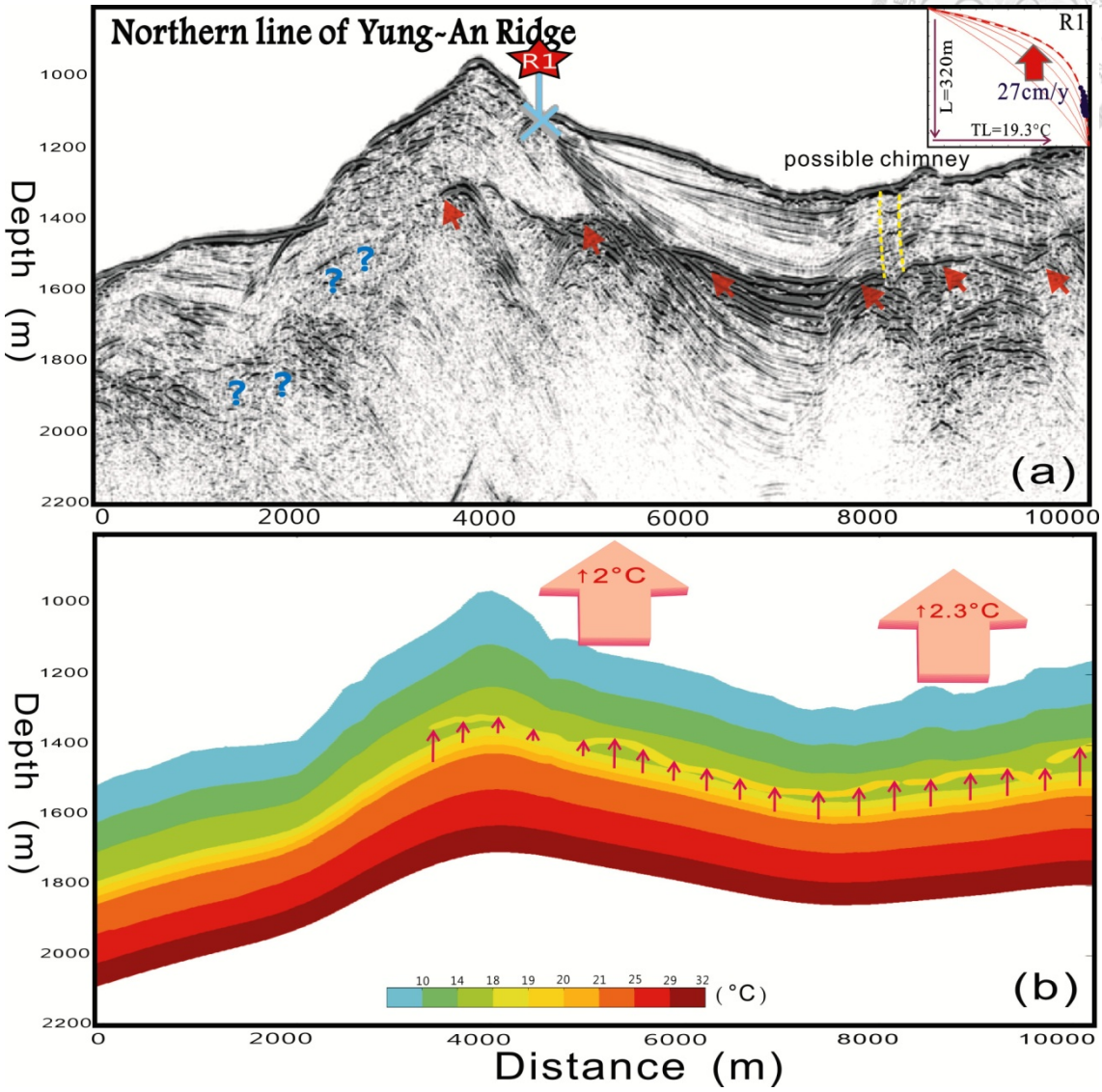

Figure 4-19 (a) A northern seismic profiles with BSR and 1-D fluid flow rate estimation results; (b) it showed the model and BSR-based temperatures along the profile. (The profile location is in Fig. 4-22a). Note that there is a possible chimney in the east basin, which seems like a BSR gap along with a blanking zone below and velocity push down reflections above (Liu, 2009; Chen et al., 2012)

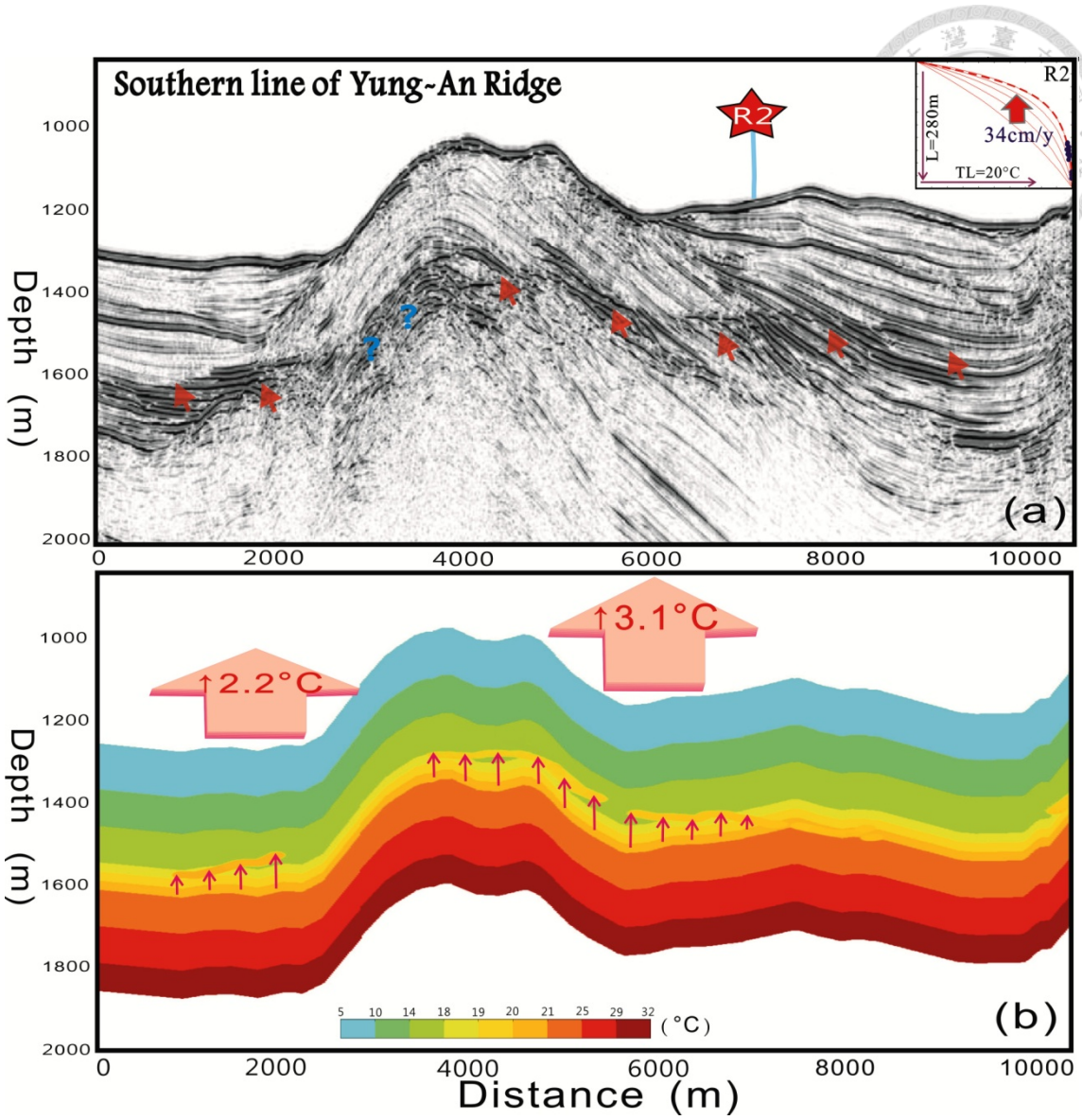

Figure 4-20 (a) A southern seismic profiles with BSR and 1-D fluid flow rate estimation results; (b) it showed the model and BSR-based temperatures along the profiles. (The profile location is in Fig. 4-22a) (Liu, 2009; Chen et al., 2012)

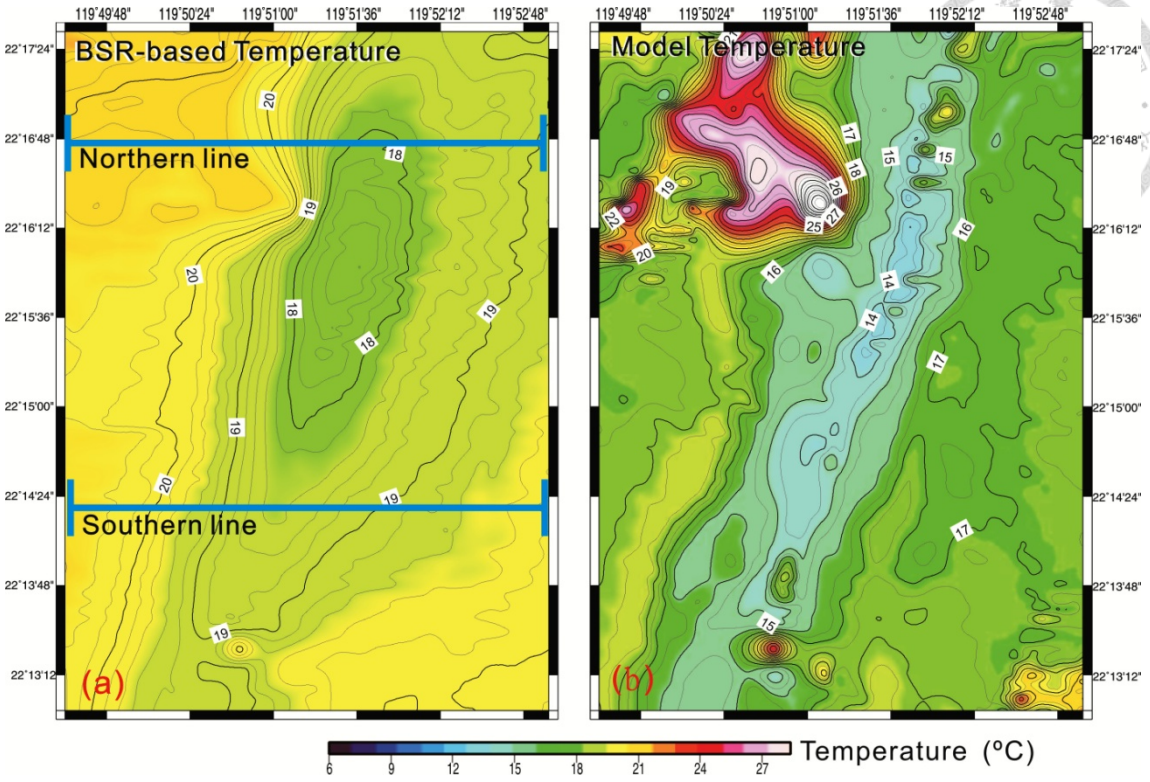

Figure 4-21 (a) Smoothed temperature fields derived from BSR and (b) model at the depth of BSR in Yung-An Ridge.

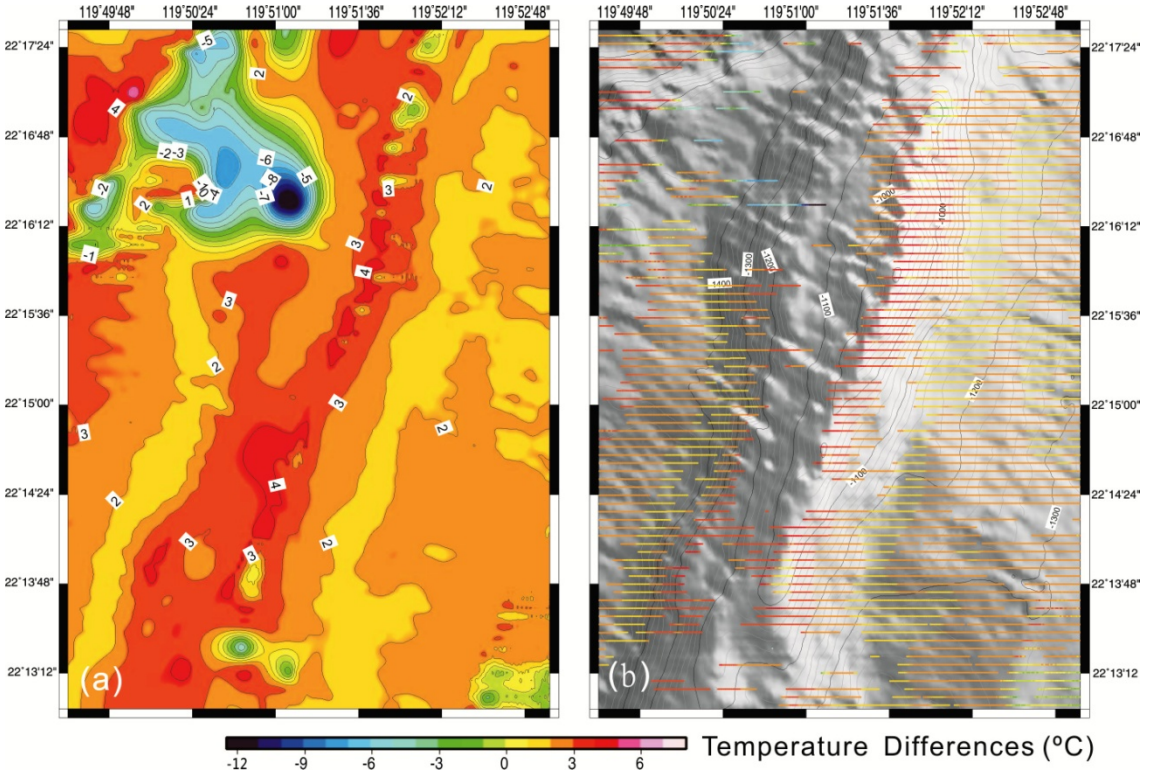

Figure 4-22 (a) Smoothed temperature discrepancies; and (b) the exact temperature discrepancies combined with the topography at the depth of BSR in Yung-An Ridge. There's a small region in northwestern part with decreased temperature.

4.4.5 Result 5: Passive Margin – Formosa Ridge

In South China Sea margin west of the deformation front, we simulated the temperature field to understand the possible mechanism driving the chemosynthetic community of this cold seep environment (Lin, et al., 2007; Chen et al., 2011). Most heat probe measurement results are assembled around the south peak, and the average geothermal gradients and heat flow are about 30.8 °C/km and 21 mW/m^2, respectively. Here, we constructed the temperature profile by using 3.48 ^{o}C and 45°C /km as the seafloor temperature and geothermal gradient (Fig. 4-23a), and analyzed two profiles to depict the structures that are perpendicular and parallel to the ridge (Figs. 4-24 & 4-25).

The subbottom depths of BSR in this region are ranging from 286 to 460 m, so that the BSR-base temperatures are fluctuating between 18 to 21 ^{o}C (Figs. 4-25& 4-27a). And these two profiles intersect to each other at a point close to the southern peak of the Formosa Ridge (22°7' N, 119°17' E) (Figs. 4-24, 4-25 & 4-26, the black cross mark). Note that BSR are very continuous for all Formosa Ridge, so we could study the 2-D and 3-D temperature fields in details.

In E-W profile at Formosa Ridge, the BSR-based temperatures overall are slightly similar to the model temperature fields (Fig. 4-24a). There is a strong temperature decrease (~ 3 ^{o}C) under the top of the ridge (center of Fig. 4-24b), and we found the BSR-based temperatures are little cooler than the model temperatures (1.5 ~ 2.6 ^{o}C) on

the flanks of the ridge. Sometimes we could even see perfect match on BSR-based and model temperatures; they have little discrepancies in the western foothill of the ridge in E-W profile (Fig. 4-24b). Such feature shows that the assumption on the chosen geothermal gradient as we mention in section 4.3 is valid (Fig. 4-25). And the average temperature decrease in the west and east sides are about 2.6 and 1.5 ^{o}C (Fig. 4-24b). Regarding temperature discrepancies under the eastern side of the profile, it is much less than that in the western side and the average temperature decrease is about 1.5 ^{o}C (right of Fig. 4-25b). However, there is a strong temperature decrease (~ 3 ^{o}C) under the top of the ridge (center of Fig. 4-25b). It is clear that the overall BSR-based temperatures are generally cooler, compared with our model temperature fields.

The N-S transect is approximately parallel to the long axis of the Formosa Ridge on the continental margin and crosses the southern peak of the ridge (Fig. 4-26a), and the topography of the north flank is gentler and shallower than of south. We constructed a temperature profile using 3.48 ^{o}C and 45 °C /km as the seafloor temperature and geothermal gradient respectively. These boundary conditions are same as the E-W transect. Our results showed a distinct decrease in temperature under Formosa Ridge. The largest temperature discrepancy occurs under the southern peak (~ 4.5 °C) and the temperature reducing are more obvious than topography change, thus this ridge structure is associated with a cooler temperature anomaly.

Furthermore, we found the distribution of temperature discrepancies on mapview is ranging from -8.5 to 9 °C (Fig. 4-26). Most of the results are close to zero differences from BSR-based and model temperature fields around the ridge (-3 ~ +3 °C). We could discovered a clear trend with large temperature decrease along the ridge axis (~ -3 °C) (Fig. 4-26). Most parts of this region are with minor temperature decrease.

Next, we will compile the results from the different sites, and interpret the mechanisms to cause the temperature discrepancies to better understand the correlation between the thermal effects and structure process.

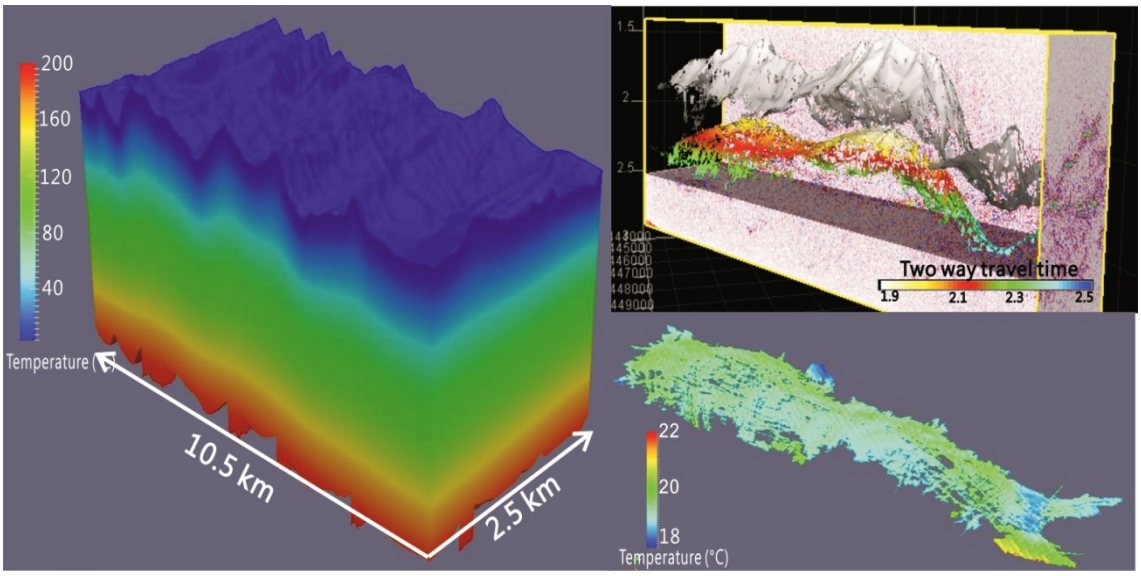

Figure 4-23 (a) 3-D model temperature field and (b) BSR distribution in 3-D seismic data in Formosa Ridge; (c) BSR-base temperatures distribution.

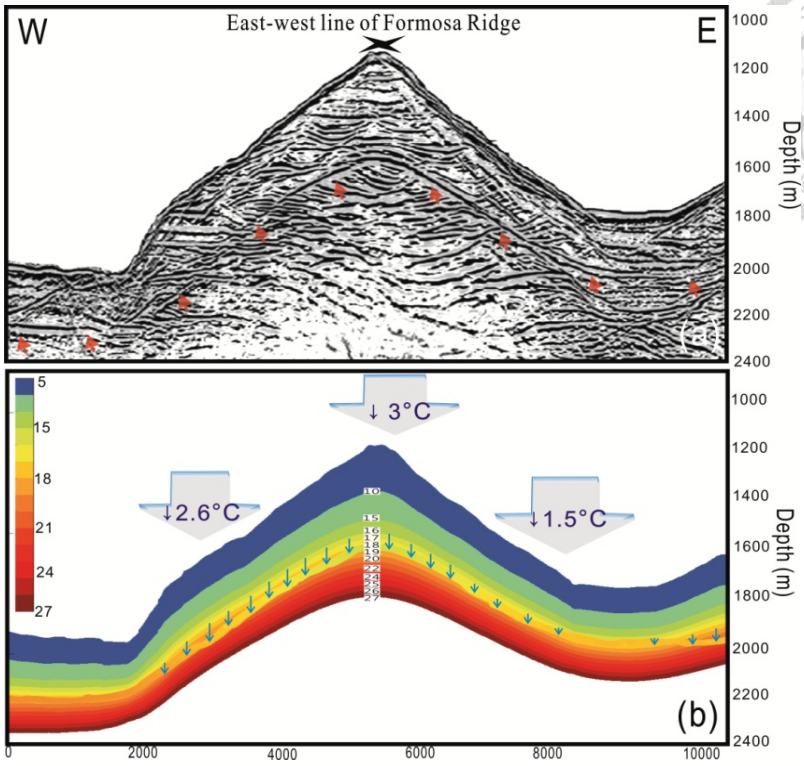

Figure 4-24 (a) E-W seismic profile with BSR; (b) is showing the model and BSR-based temperatures along the profiles. Blue cross marks the intersect point.

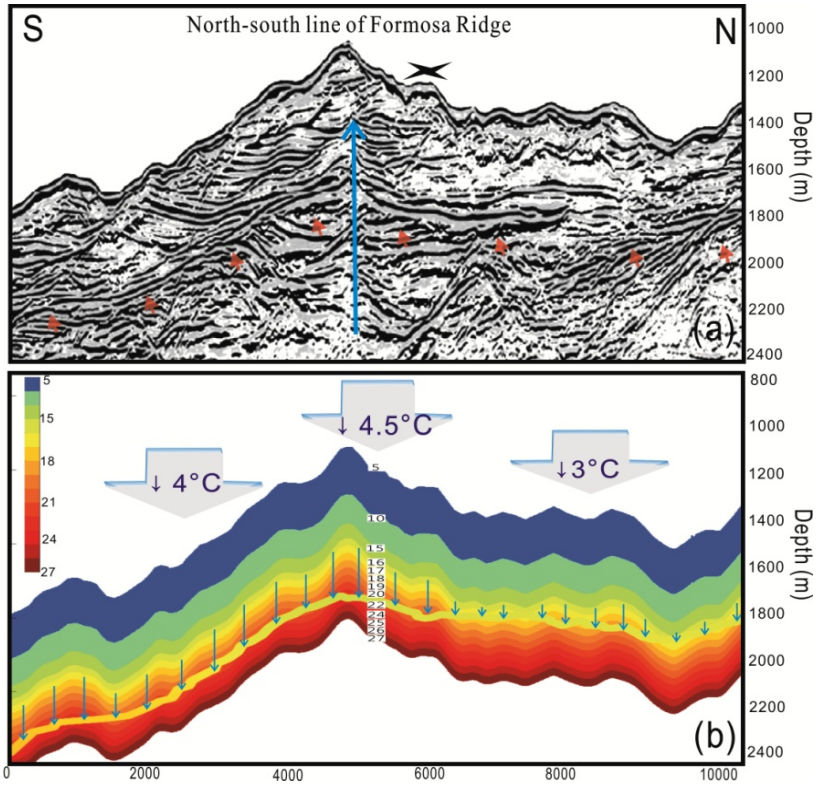

Figure 4-25 (a) N-S seismic profile with BSR; (b) shows the temperature discrepancies along the profiles. Blue cross marks the intersect point.

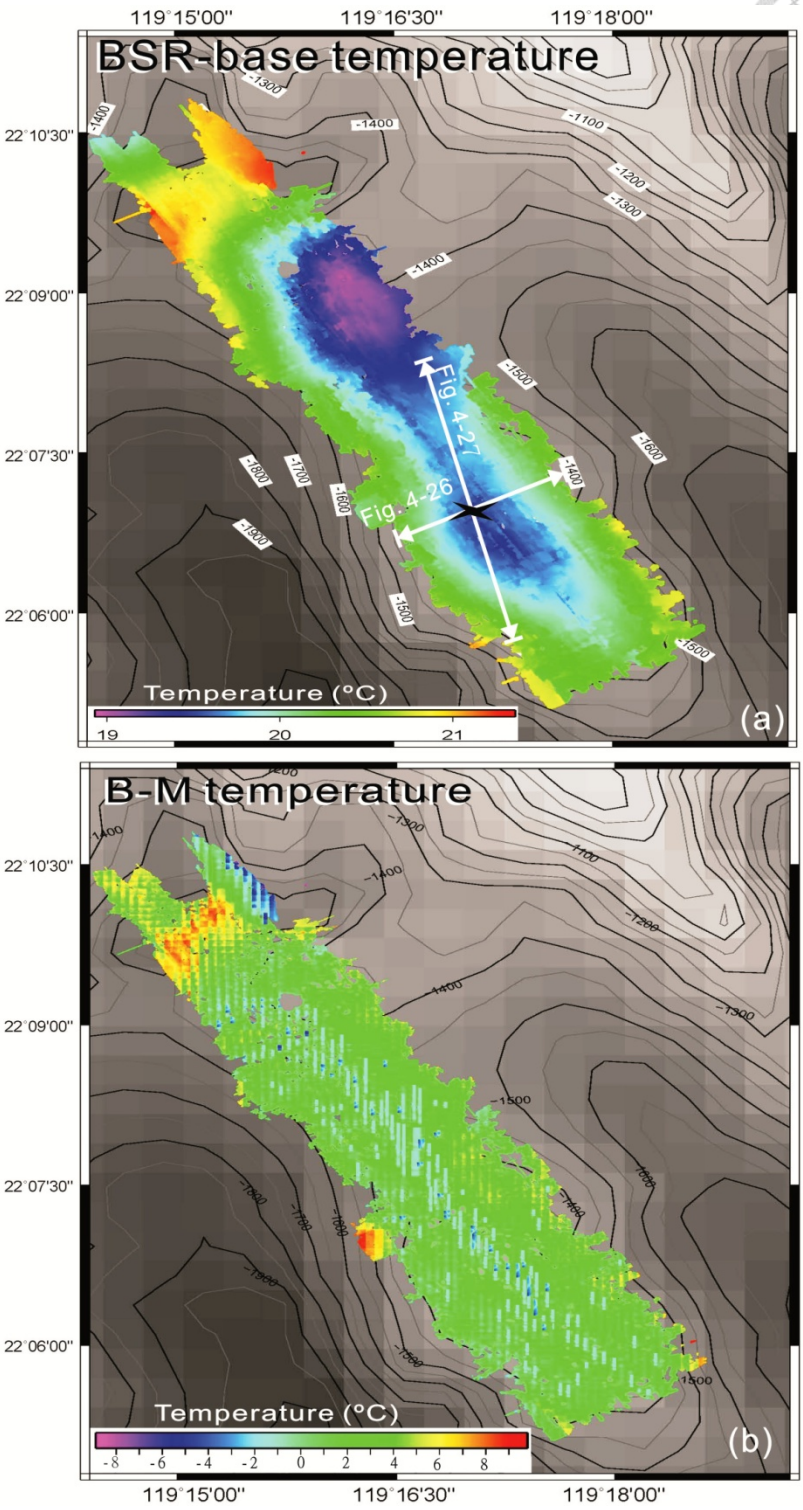

Figure 4-26 At the depth of BSR in Formosa Ridge, we use (a) BSR-based temperatures subtracted the model temperatures to derive the (b) temperature discrepancy field to see the regional changes.

Chapter 5: Interpretation and Discussion: Regional Geological Processes that Cause Thermal Perturbation

From this work we have documented temperature discrepancy between the BSR-based temperature field and the results from thermal conductive models. We found there are some positive and negative temperature differences to indicate the regional heating or cooling effects, they might caused by several geological processes. Next we will propose some possible geological processes to interpret the causes of such discrepancies.

5.1 Topographic Effects

Heat flow that escaped from the crust will take the shortest path to reach the low temperature regions, such as the seafloor in our case. The irregular bathymetry will cause non-vertical heat transfer, and the geothermal gradient naturally increases under the valleys while it decreases under the bathymetric highs (Fig. 5-1a). Using Yung-An Ridge as an example, we found that the geothermal gradients can vary 3.5 times (Q values changed from 0.028 to 0.098 °C /m) within a small region (Table 1).

Ganguly et al. (2000) have quantitatively studied the topographic effects on 1–2 km scale based on BSR data from the Cascadia margin, and they found ~50% variation in heat flow due to topographic effect in that region. Chi et al., (2008) had used a

transect in the subduction zone at the latitude of 20.5 °N, the preliminary results give more than 20 °C/km of perturbation from topography alone, which is consistent with the results from the analytical solution using a sinusoidal topography (cf. equation 4–66 of Turcotte and Schubert, 1982).

Based on the finite element thermal modeling, we have found obvious topographic effects on the thermal structures for the shallow crust after combining the BSR-based temperature fields (Figs. 5-1b & c). The curvature of BSR-based temperature is usually slightly less than that of the seafloor topography (Fig. 5-1a). Such large topographic effects mean that the heat flow data acquired at shallow depths in a high topographic relief region will need to be corrected for topographic effects before the heat flows can be used for geological interpretation, that's the reasons why we always used the good match of the BSR-based temperature field with the model temperature filed (Fig. 4.5) to decide our geothermal gradient.

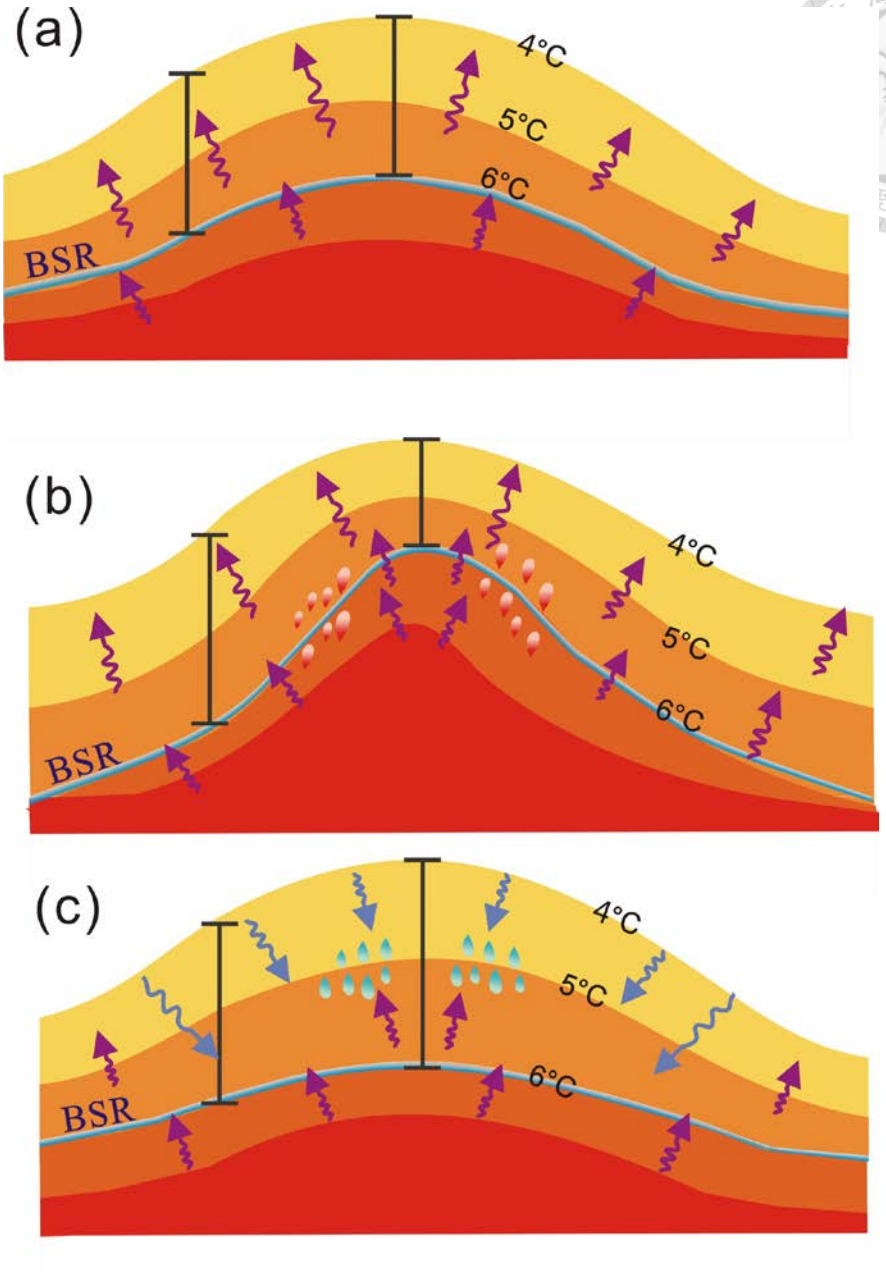

Figure 5-1 Conception models showed how topographic effects influence the temperature fields: (a) Topographic effect caused the temperature fields become focusing beneath the topographic high (ridge) in a non-vertical heat transfer way to keep similar geothermal gradients near the surface ; (b) If there are some heat flow beneath the ridge, BSR-based temperatures will increase temperature field in shallow sediments and raise the regional geothermal gradients; (c) If there are some cold flow (e.g. seawater) penetrated into the ridge, BSR-based temperatures will decrease temperature field in shallow sediments and lower the regional geothermal gradients.

5.2 Thrusting and Fluid Flow

According to our regional studies, the most noticeable heating effect is around the Yung-An Ridge. There are major thrusts just beneath the ridge imaged by the long offset seismic data (Fig. 2-8) (Lin, 2012). Another example is in upper part of the Penghu Canyon (Han, 2012) which is nearby the northwestern tip of deformation front. Here, we combined the results of regional temperature fields and structure interpretation to study the thermal effects.

5.2.1 Thrusts in Yung-An Ridge

Refer to the proximity of the Yung-An Ridge; two thrusts (T1 & T2 of Fig. 5-2) can bring temperature increase in hanging wall (Fig. 2-8) (Lin, 2012). The T1 thrust might provide a pathway for the upward fluid flow, and the T2 thrust can be another conduit allowing the fluid migration as well, these are consistent with our simulating results (red zone of Fig. 5-2). But the gap of BSR signals between T1 & T2 might owe to the intermitted fluid migration disturb the temperature filed then dissociate the gas hydrate. The positive temperature differences could extend from the ridge (Fig. 4-22b) to the western basin according to our study result (Fig. 4-22a), moreover, there are some high methane fluxes (65 to 118 mmole/m^2yr) were detected to indicate it has very active venting with methane here (Lin, 2011). So we considered there is generally warm fluid upward migration along the fault planes leads heating effects in this region (Fig. 5-2).

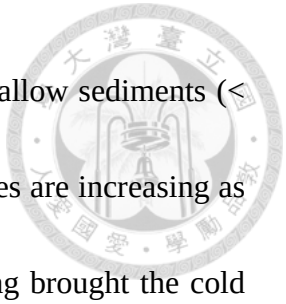

However, regarding the heat flow measurement data in very shallow sediments (< 30 m) of Yung-An Ridge (Peng, 2012) (Fig. 2-9), the heat flow values are increasing as the distance from the thrust, which might indicate that thrust faulting brought the cold sediments (the sediments near seafloor are colder than the deeper ones) to deeper depth to cause cooling effect (Fig.5-3b), it even stronger than the warm fluids upward along the fault conduits (Ganguly et al., 2000) (Fig.5-3a).

Here I presumed a possible model for these converse results in Yung-An Ridge: The fluid upward migration along the T1 fault plane caused the heating effect here, which is consistent with our results of simulating temperature fields (red big arrow on the thrust of Fig. 5-4). Then the active thrusts or a splay fault (eg. T2 of Fig. 5.2) might deform and bring cold sediments down to the deep thus cool the temperature field, which is consistent with the measured results of heat flow data (blue big arrow on the thrust of Fig. 5-4). Note that the heat flow measured data here is still higher than the average value offshore SW Taiwan (~ 58 mW/m^2yr). So, even though the in-situ measurements showed a few relative cooling effect (deformed sediments) near the top of ridge, I considered that the major thermal effect in Yung-An Ridge is due to the upward fluid migration along the fault planes, and the splay fault may reducing some heating effect to cause the heat flow pattern as the measurement results.

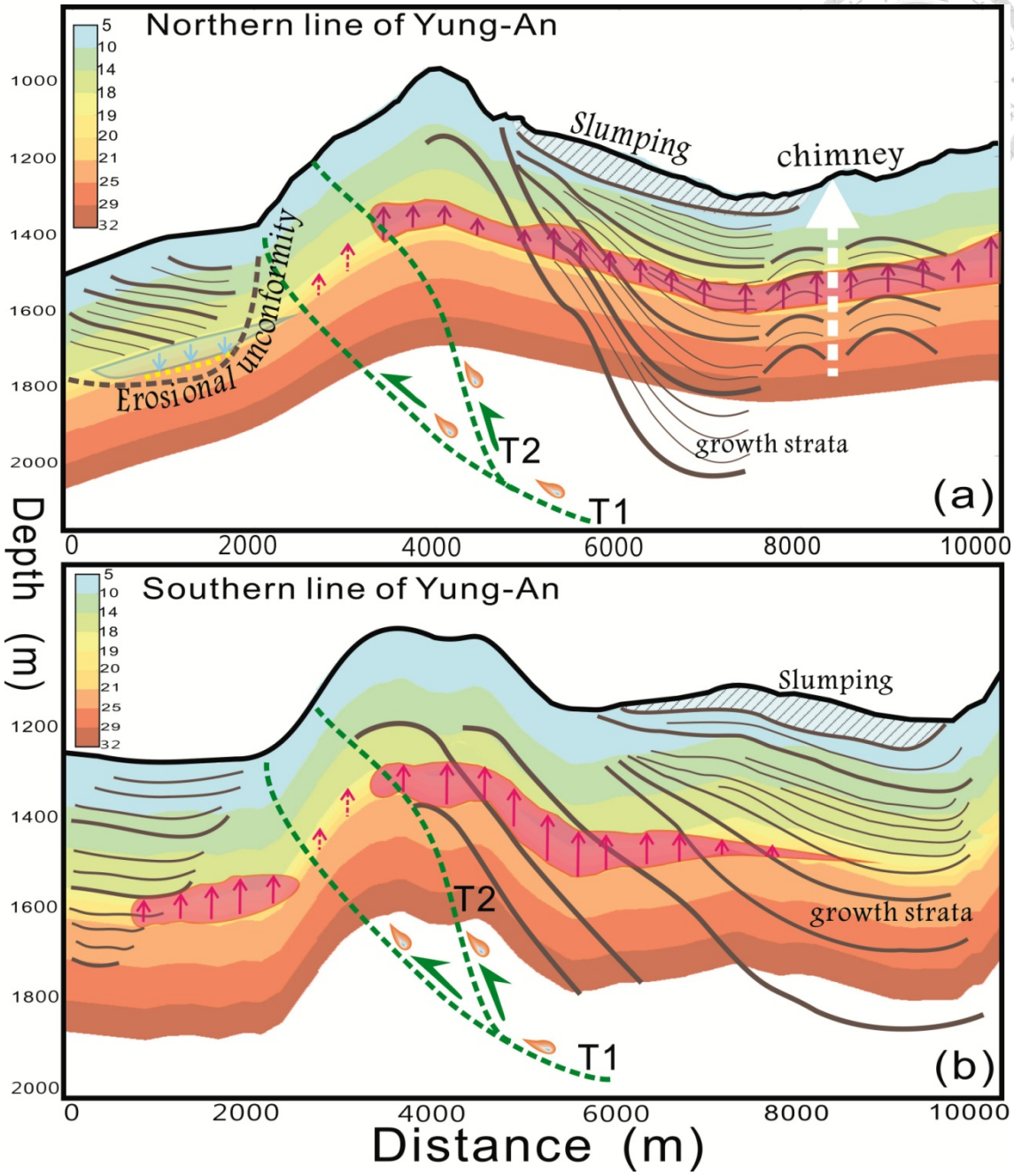

Figure 5-2 Interpreted profiles (follow Lin, 2012's interpretation) of temperature fields and structure features derived from Figs. 4-19 & 4-20, red upward and blue downward arrows meant heating and cooling effect respectively. Major thrust (green dashed lines of T1 and T2) propagated from south to north to influence the structures, and increased the temperature field because of the fluid migration along the fault planes. (a) North line marked a possible cooling effect from an erosional unconformity and a chimney structure. (b) The obvious growth strata might deform by a newer splay fault (T2) then brought more heating effect in the eastern than the western side.

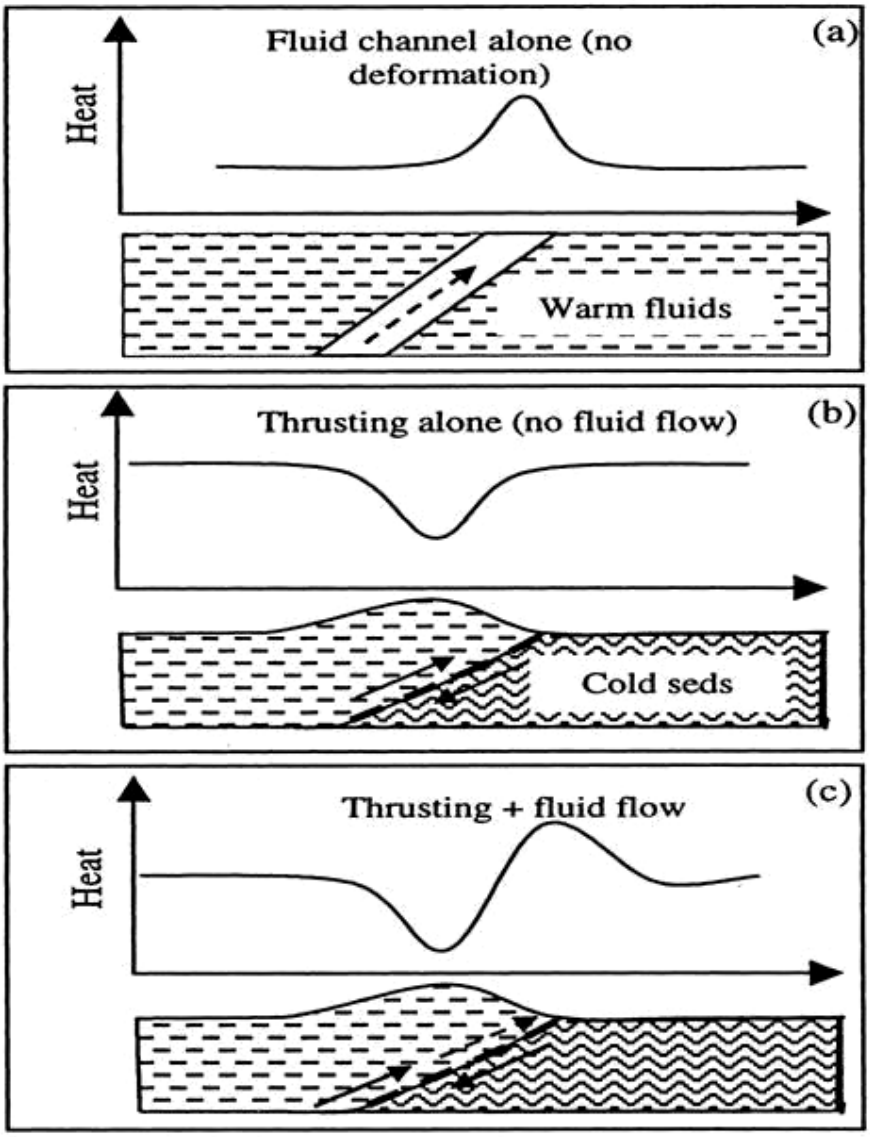

Figure 5-3 Localized fluid flow and thrusting may contribute to the correlation between seafloor topography and heat flow. (a) Migration of warm fluids upward along a channel leads to anomalously high heat flow. (b) Thrust faulting, which brings cold sediments to greater depths, lowers the heat flow. A topographic high is produced as an anticline in the hanging-wall block. (c) When both phenomena occur, a pattern is formed with low heat flow over the topographic high and high heat flow at the base of the high (Ganguly et al., 2000).

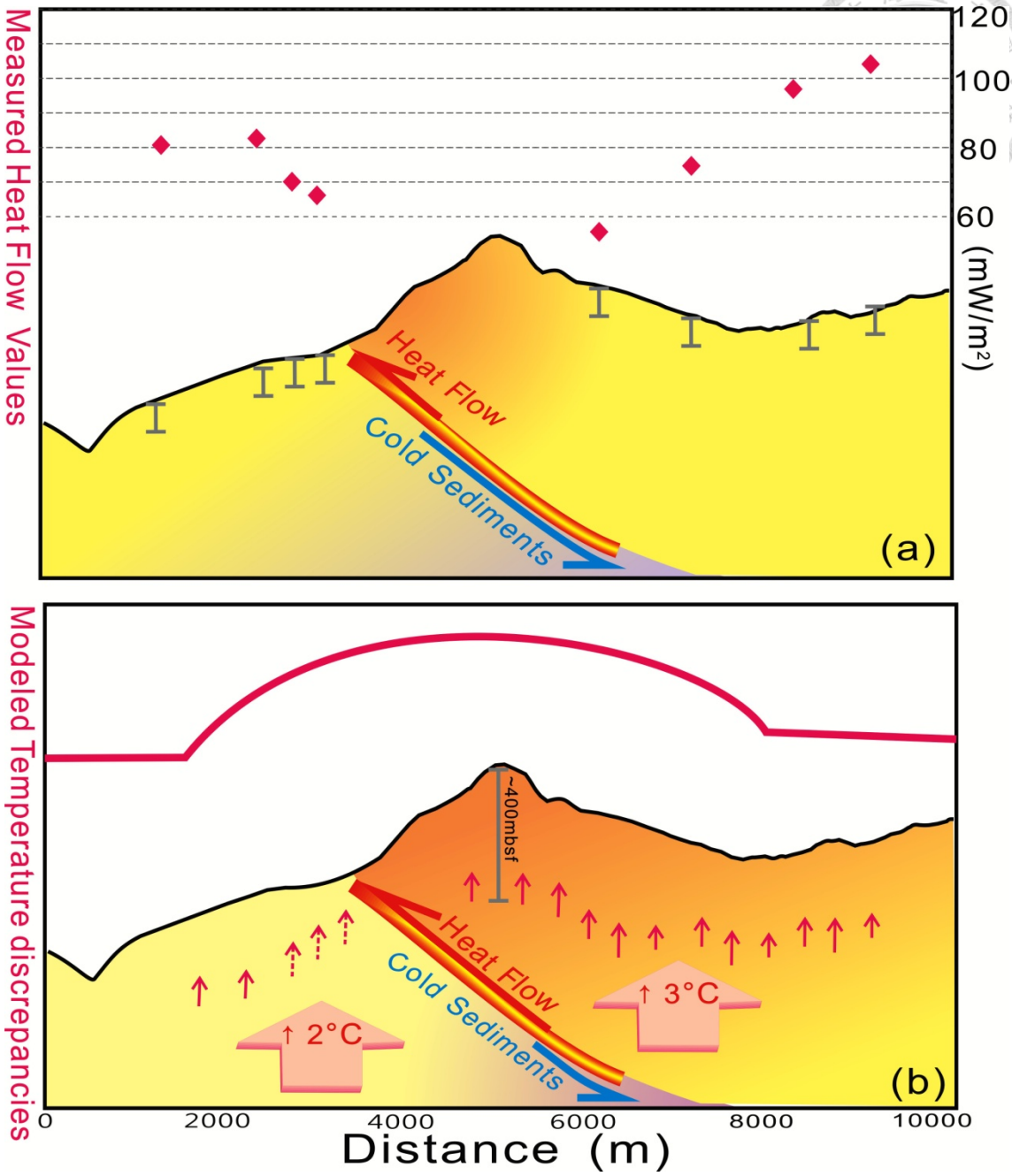

Figure 5-4 Sketches showed two different heat flow profiles derived from the measurement data and model temperature field in Yung-An Ridge: (a) Projected the in-situ measured heat flow (< 30 mbsf) in an east-west profile; (b) Our simulated results indicated the heating effect beneath the ridge (~ 400 mbsf). Big arrows along the thrust indicated the heating effect induced by the fluid flow upward migration; and the big blue arrows meant the cooling effect caused from the cold sediments slipped down to greater depth.

5.2.2 The Frontal Thrust

For the frontal thrust in upper reach of Penghu Canyon, Han (2012) defined the location of frontal thrust from the long offset seismic data (Fig. 4-8a). From our study, we found some cooling and heating effect on the hanging and foot walls, respectively (Fig. 4-10b). Base on the third model addressed from Ganguly et al., (2000) (Fig. 5-3c), warm fluids could migrate upward along the fault plane leading to anomalous high heat flow, and if the thrust faulting simultaneously bring cold sediments into a greater depth then lower the heat flow at the same time, the temperature fields will display both phenomena as our simulation result in upper reach of Penghu Canyon (Fig. 4-8), there are negative (blue; cooling effect) and positive (red; heating effect) temperature differences over the handing and downing wall respectively (Fig. 5-5a). What we discovered might be part of the thermal evolution history in this north tip of the frontal thrust region, maybe someday the temperature field will change its pattern.

Furthermore, we derived similar patterns on temperature discrepancies of the frontal thrust in upper reach of Penghu Canyon and Frontal Ridge (Fig. 5-6), which are respectively located in the northernmost and southernmost boundary of the arc–continent collision zone while China passive margin is entering into the trench. Both of them show temperature increase at the toe of the accretionary prism. And this heating effect might be owing to the sediment dewatering and the extensive fluid

migration there (Bray and Karig, 1985; Suess et al., 1998). The increasing temperatures of our simulating results are similar with the temperature anomalies in Barbados accretionary wedge (Vrolijk et al., 1991; Moore and Vrolijk, 2010) (Fig. 5-7). On the other hand, the arcward-decreasing temperature may be explained by the slab cooling effect (Chi et al., 2008), so the heating effect is gradually reduce.

The 1-D fluid flow rate is higher and the heating effects are spreading broader in Penghu (23 cm/yr) than Frontal (16 cm/yr) region. That's because the dehydration reactions, which is forcing the fluid migrating upward within the sediments (Moore and Vrolijk, 2010), are getting intense in more compressive collision region to the north. On the other hand, more focus heating effect in Frontal ridge to the south also consistent with the fluid accumulated which was identified from a low velocity anomaly below the BSR (Fig. 2-5). They both supported that there are huge amount of fluid migration from the deeper part (such as the décollement), to cause such temperature anomalies in shallow sediments.

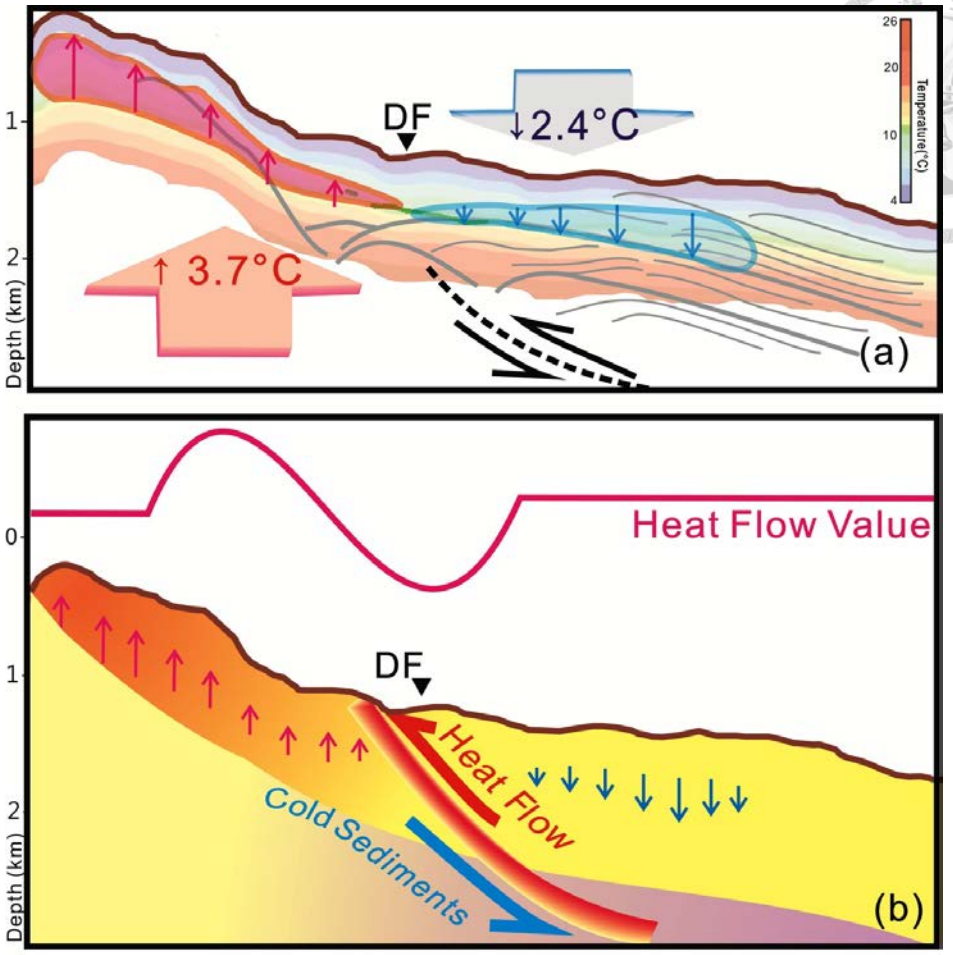

Figure 5-5 The Conceptual model of frontal thrust region: (a) We found a drop of the temperature discrepancies around the deformation front, which is almost correlated with the outcrop of the frontal thrust on the seafloor (DF: deformation front). (b) Our modeled result showed heating and cooling effect simultaneously along the profile.

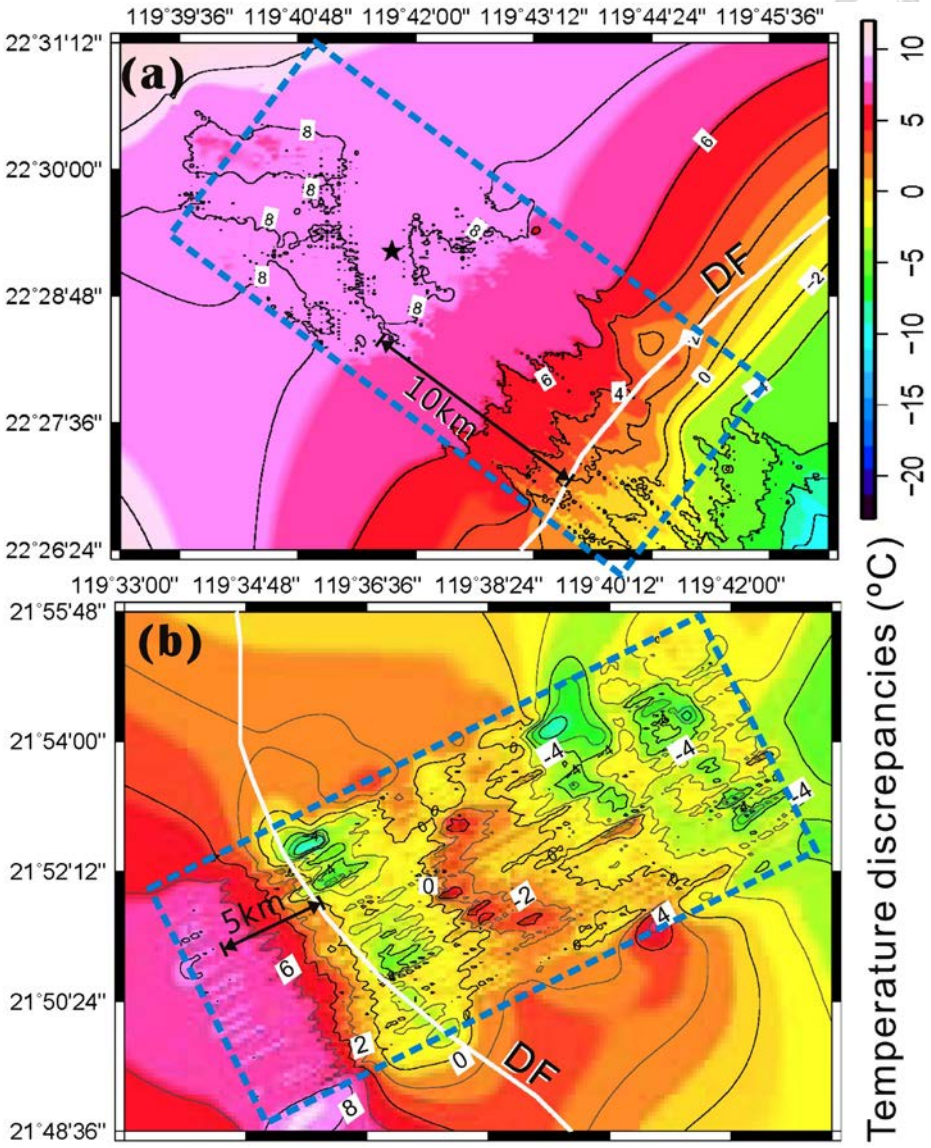

Figure 5-6 Compare the temperature discrepancies in mapview of (a) the upper reach of Penghu Canyon and (b) Frontal Ridge. Using the deformation front (DF) to be a nearby index on the location of the frontal thrust, we found not only obvious heating effects at the toe of the accretionary prism, but also the arcward cooling effects in the accretionary wedge in the vicinity of the deformation front.

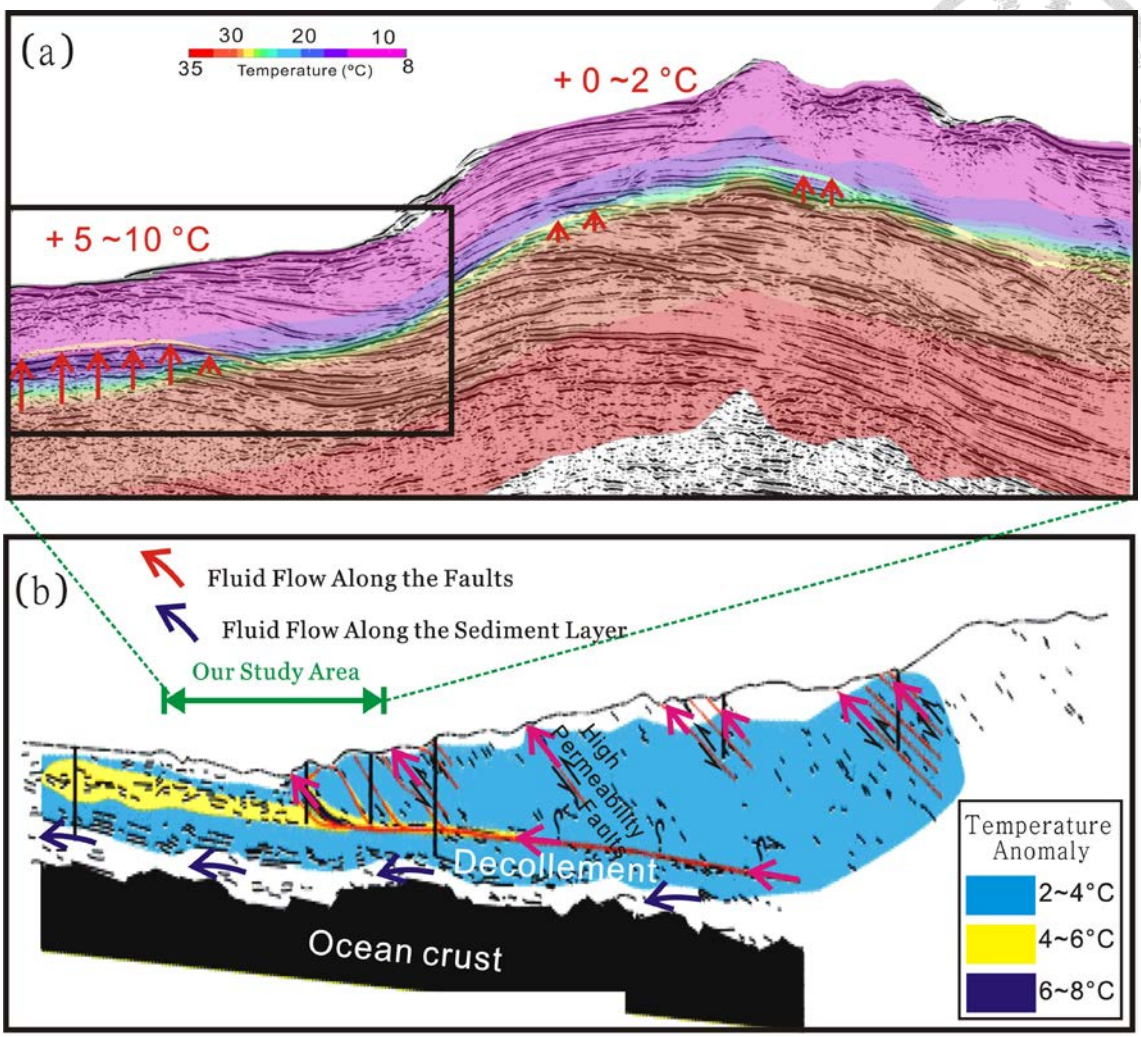

Figure 5-7 Our simulation region is relative close to the trench in the accretionary wedge; we found similar temperature increasing results as the temperature anomaly in Barbados accretionary wedge. (a) There are more temperature increases (+ 5 ~ 10 ℃) in the toe of the accretionary wedge than in frontal ridge (0 ~ + 2 ℃). (b) The permeability of the faults allowed the fluid upward migration along the faults from the décollement in the accretionary wedge, and increased the fracture permeability, so the in-situ measured temperature anomalies along the profile in Barbados accretionary wedge also showed the obvious heating effect, especially at the toe. (After Moore et al., 1991 and Vrolijk et al., 1991)

5.2.3 Thermal Models of Thrusts Region

For our study results in shallow sediments, I suggested the thermal effects of the thrusts region could include: (1) the thrust faulting brought shallow sediments to the deeper then caused cooling effects; (2) the fault plane allowed the fluid upward migration to cause heating effects; (3) the geometry (eg. the fault dip control the fluid upward migration easily or not) and slip rate (eg. slip faster could induce more friction heat) of the fault planes could dominate the temperature spreading and equilibrium rate since the fluid migration is mainly propagate along the fault plane.

Here I proposed several possible models to describe the thermal effect after studying our simulated temperature fields and Ganguly et al (2000):

(a) If the cooling effect is stronger than the heating effect, or the permeability along the fault is too low to offer complete pathway for the fluid migration, thus the heat flow in faulting region will be lower than adjacent areas (Fig. 5-8a).

(b) If the fluid migration upward is heating the ridge intensely, but the downward thrusting is getting weaker to bring cold sediments down to the deeThe relative higher heat flow will be easily detected in shallow sediments (Fig. 5-8b).

(c) When the thrust deformation is eased off, as well as the fluid migration is in an constant rate, the thermal effect could achieve a harmonious situation (Fig. 5-8c), so that both the heating and cooling effects could be detected. As the phenomena we

discovered in Penghu (Fig. 4-8). In front and behind the thrust, the sediments are heated and cooled, respectively. Note that if the dip angle of the fault is too steep, it may be difficult to clearly demonstrate the thermal effects in hanging and foot wall blocks, respectively. But we could still detect a general trend along the temperature field.

(d) When the heating effect brought from the upward fluid migration influences the whole ridge for a long time, then the thrust deformation from a reactived fault or a splay fault to carry the cold sediments down to the deep and cause the cooling effect, thus reduce the heat flow beneath the core of the ridge (Fig. 5-8d).

Maybe all these thermal models on thrusts could achieve a regional dynamic equilibrium after a long time. Therefore, the proposed thermal effects can only partially explain the heat flow patterns. We need more detail and precise information of the faults, such as the slip rate and the geometry, to better understand the heat flow patterns.

Besides thrust faults, there are some other geological process that can increase the temperature at shallow crust. Next, we will discuss the heating effect nearby the anticlines or diapirs.

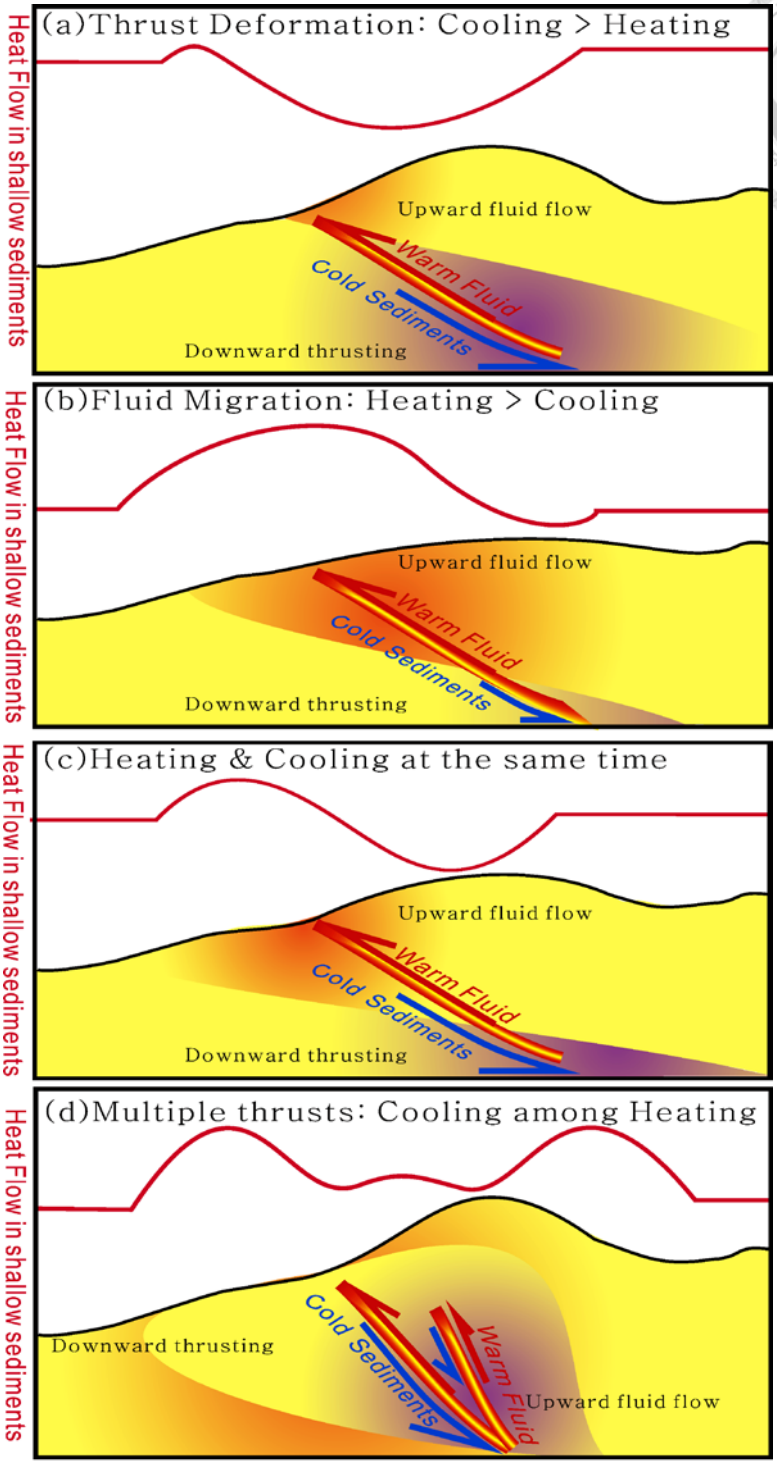

Figure 5-8 Several possible thermal effects near the thrusts: (a) Stronger cooling effect caused by cold sediments carried down to the greater depth in the footwall block (b) Stronger heating effect owing to the fluid migration along the fault plane; (c) Cold sediments and heat flow effect occurred in a lower angle thrust, the cooling and heating effect happened in the handing and foot walls, respectively. (d) The heating effects already spread all over the ridge, and the second thrust is activated to lower the heat flow around the thrust.

5.3 Sedimentation and Erosion

5.3.1 Mud Diapirs

Our thermal modeling results showed the heating effect in the anticline and diapir (Fig. 4-14. 4-15.4-186). Mud diapirs occur in numbers of modern accretionary wedges (Brown and Westbrook, 1988) and provide significant contributions to structural development, sedimentary bed distortions, mass motion and heat transportation, fluid pressure development, and hydrocarbon generation, migration, and accumulation (Bagirove and Lerche, 1999). Therefore, we focused on the diapir structure and tried to reconstruct the thermal model by studying temperature discrepancies and previous geochemical investigations. However, we have just one example of the mud diapir from our study regions, maybe we could study additional diapirs in the future to see if our interpretation can also be applied to the other regions.

The mud diapir has clear vertical structure imaged by the seismic data, and the diapiric crest even reach the seafloor and its root could extend to more than 1260 mbsf (Figs. 4-14; 5-9). Here we used the simulated and measured results along this profile to compare and analyze the thermal data in the flank and summit of the diapir respectively (Tab. 2; Fig. 5-9), as a result, I found that this diapir has previously brought some warm fluid flow from deeper depth based on the increasing heat flow as followings:

(1) The vertical fluid flow was increased from 8 to 15 cm/yr in outside and inside

of the diapir, it meant the diapir structure increased ~ 88 % upward fluid flow rate.

(2) We could derive the geothermal gradients (G) changed from 32 to 40 °C/km at the depth of BSR (~ 440 mbsf), and from 62 °C/km to 80 °C/km at the seafloor respectively, it meant the diapir structure increased 25 ~ 29 % of geothermal gradient in this region.

(3) After multiplying the measured thermal conductivities (K), we found the heat flow increased from 28 to 38 mW/m^2 at the depth of BSR, and 55 to 76 mW/m^2 at the seafloor. There is 36 ~ 38% increase of the heat flows from the flank to the summit of the diapir.

Oppositely, we used the relation derived by Von Herzen et al., (1989) to study the possible reduction rate of the heat flow due to the sedimentation in this region:

$$\frac{Q^*}{Q} = 1 - erf(X) - \frac{2X}{\sqrt{\pi}} e^{-X^2} + 2X^2 erfc\,(X) \qquad \text{(Eq. 10)}$$

Where $X = 0.5 \times U \times \sqrt{\frac{t}{\alpha}}$; (Eq. 11)

And Q is the initial surface heat flow, α is the diffusivity, Q^* is the modified heat flow due to the sedimentation; ***erf( )*** and ***erfc ()*** are the error function and its complement. U is the sedimentation rate. The time ***(t)*** is in seconds. We use the thermal diffusivity of 8.3×10^{-7} m^2/s as α here (Holman, 2002).

Here, we used the sedimentation rate about 0.4 mm/yr nearby this region (Horng, 2013), then we derived ~ 38 % reduction of the heat flow base on the relation equation 10; it's quite consistent with our simulation results. On the sum, this percentage also meant the heating effect from the diapir was reduced 38 % by recent sedimentation.

Table 2 Comparison of measurement and BSR-based thermal data in diapiric structure:

Latitude N	Longitude E	K (W/mK)	G (K/km)	K X G =Q (mW/m^2)	Diapir Relevant	location
22.080	120.344	0.952	80	76	Summit	Seafloor
21.863	120.354		40	38		BSRs
22.038	119.891	0.887	62	55	flank	Seafloor
21.863	120.300		32	28		BSRs

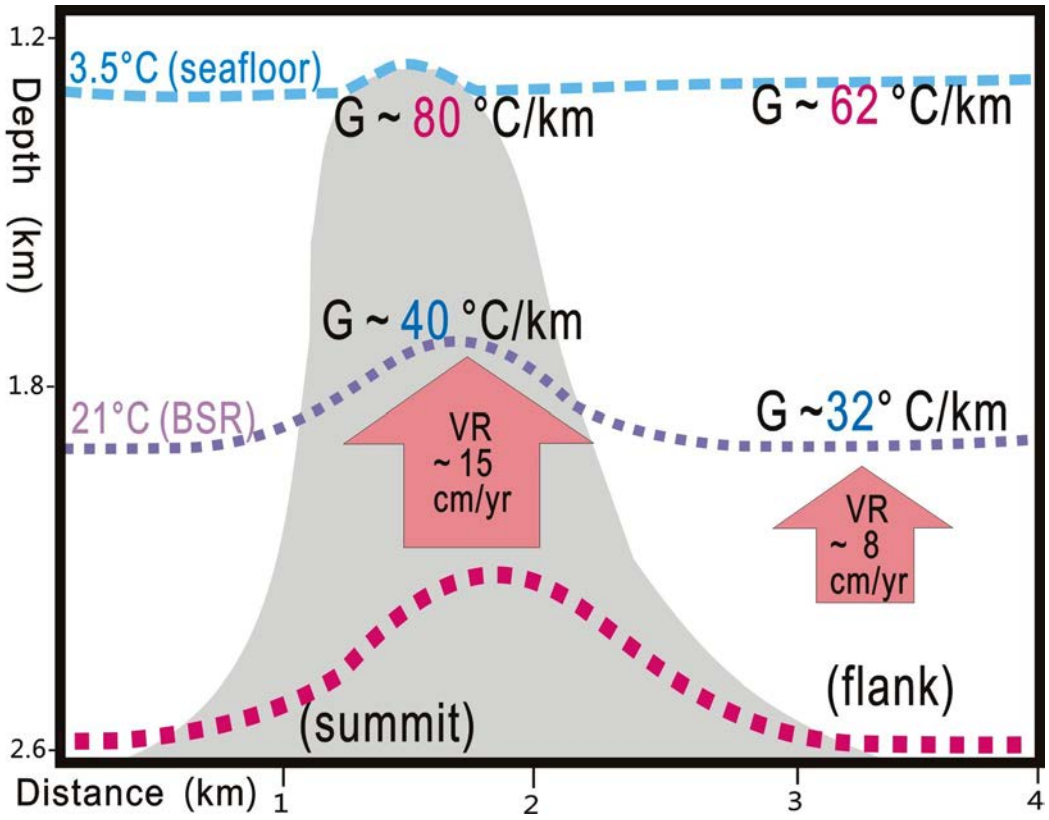

Figure 5-9 Combined the measurement and simulated results; we draw a conception sketch to compare the differences between the geothermal gradients (G) and vertical fluid flow rates (VR) in flanks and summit of the diapir.

5.3.2 Mass Transport Deposits

We found a possible slump structure in Penghu upper reach slope using the seismic profile (Han et al., 2012), which shows a bulge surface and transparent reflections (no clear strata) in the sediments, as well as the chirp sonar image indicating that the topographic slope is decreased from 12 to 6 degrees from uphill to downhill (Fig. 4-8a1). All of these features support the possibility of a mass-transport deposits (MTD) event occurred in this region (Fig. 4-8a).

Along the profile of Fig. 4-8, the temperature fields at the depth of BSR also show some dramatic changes allowing us to further analyzing it. Near the site J nearby the MTD location, we found the highest vertical fluid flow rate (~ 43 cm/y) (Figs. 3-8J; 4-8a2) of SW offshore Taiwan. The temperature discrepancies are averagely higher 2 ~ 5 degrees in downhill and uphill. So that we proposed some processes in sequence to interpret our study results:

(1) Before the MTD happened in Fig. 5-10a, we supposed that it is in a steady state for all sediments that had a consistent geothermal gradient (G_0), so the previous temperatures in BSR were consistent with the model temperature field in equilibrium.

(2) As the MTD happened for a while in Fig. 5-10b, the model temperature field (which is a topography-dependent temperature field) would be modified as the surface changed, but it still need more time for the thermal pulse to propagate to the depths of

BSR. So that the geothermal gradient increased to G_1 to respond to the shallower BSR-subbottom depth due to the losing materials from the seafloor; at a mean time, the geothermal gradient decreased to G_2 to respond to the increased BSR-subbottom depth from the newly deposited materials on the seafloor. And the delayed heat transfer has not reached below BSRs (deeper part) to modify its geothermal gradient (G_0) yet. So we interpret that at this time the thermal equilibrium has not been reached yet.

(3) After a while (maybe thousands years) in Fig. 5-10c, the model temperature field could restore a new isotherm (G_3) to be consistent with the topography, but the gas hydrate system needs more time to response the new P-T condition, so we could find distinct increases in Penghu upper reach slope (c_1) to indicate that it is still in a transient stage. This time period could be derived from an average thermal diffusivity, as that we will further discuss about this in this section later.

(4) After a much longer time in Fig. 5-10d, the P-T condition of BSR will lead the BSR-based temperature field approaching to the model temperatures with consistent geothermal gradient (G_4). It might restore to an equilibrium state in this region and the BSR-based temperatures will consistent with the model temperatures then.

We could see a future map that if we got the dating result of this MTD structure from a local coring samples, we may have the chance to derive more information about the thermal diffusion rate caused by this MTD structure. Moreover, the transient process

might have occurred in other places with different geological processes. For example the cooling effects at the regions with rapid erosions in northwestern of the Yung-An Ridge (Fig. 5-1a) or Formosa, we will also discuss about them in next section.

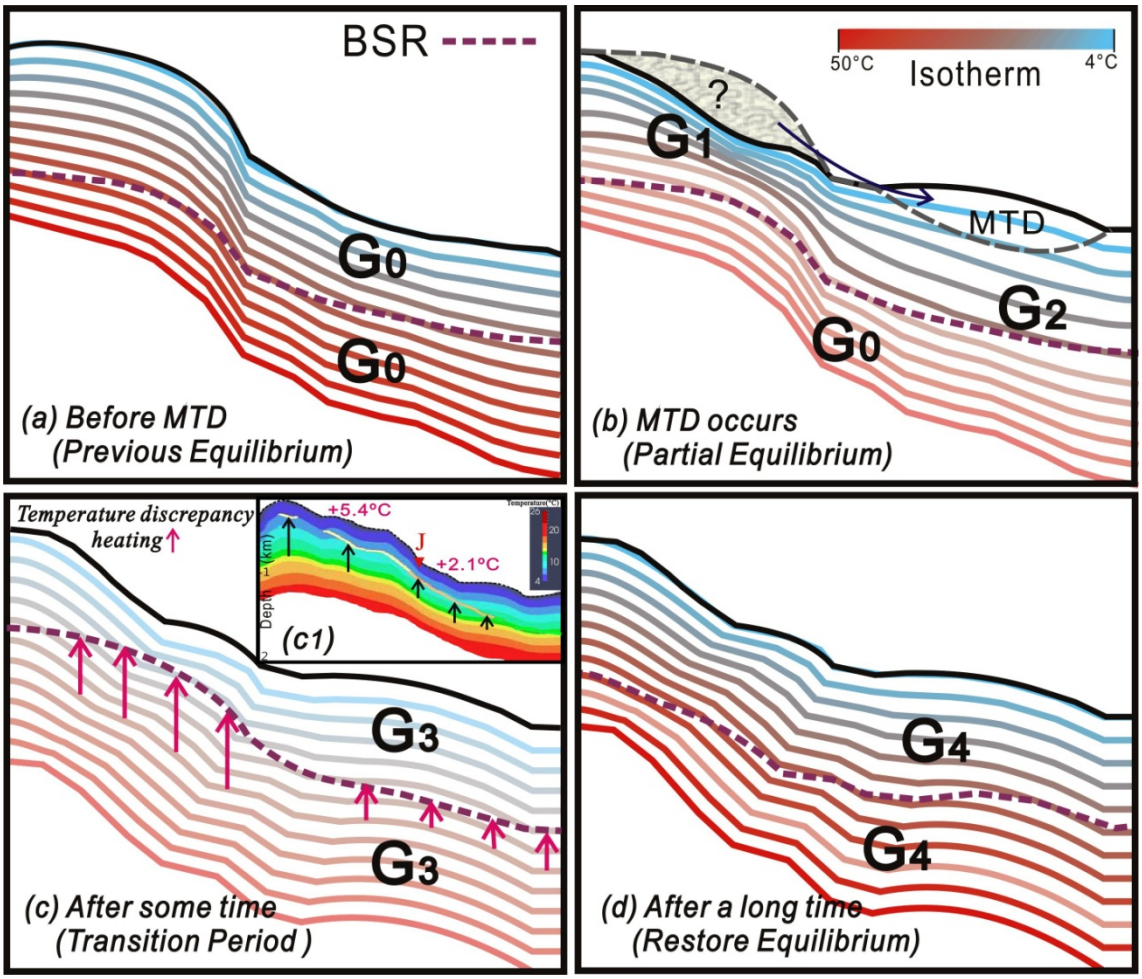

Figure 5-10 We modeled the isotherms and geothermal gradients during the MTD event to describe the isotherm evolution. (a) The isotherm before the MTD happened. It is in a steady state with consistent geothermal gradient (G_0) (b) The near surface geothermal gradients started to modify to new geothermal gradients (G_1, G_2) as a result of the MTD occurred, but it has not influenced the deeper part yet. (c) The BSR-based temperature field might need more time to adjust to the new temperature field (G_3), so the geothermal gradient in Penghu upper reach slope (c_1) indicates that it is in a transitional stage. (d) Temperature field here might restore to an equilibrium state after a long time (G_4), and the BSR-based temperatures will be consistent with the model temperatures then.

5.3.3 Canyon Incision

We have a classical erosion example for study regional thermal effect. In South China Sea, the magnitude and distribution of heat flow may affected by the tectonic development and sedimentation (Cloetingh et al., 2010). Around the Formosa Ridge, the ridge slopes down from north to south, and the strata within the ridge are generally flat but exhibit sediment waves features (Fig. 2-11). The submarine canyons cut into the strata and form the valleys surrounding the ridge, and the local eroded strata (Figs. 4-24a & 4-25a) are also probably due to the submarine mass wasting processes. A stronger erosion effect can be found in the E-W profile that crosses the canyon (Figs. 4-24a). However, the cooling effects are more obvious in the N-S profile (Figs. 4-25b), which may suggest a strong N-S horizontal fluid migration. In short, these cooling effects around the ridge supported that there is a relatively cold and diffusive fluid flow under the ridge.

The fluid related temperature perturbation made the BSR-base temperature field is not parallel to the bathymetry as the model temperature field (Fig. 4-26b & 4-27b). Instead, it becomes more parallel to the sub-horizontal strata (Fig. 5-11). In another word, the isotherms of BSR-based temperature field are relatively flat but not "simulating" the sea bottom as usual.

Here we proposed that the diffusive fluid migration has facilitated mixing and

smoothing the temperature field in Formosa Ridge, especially in the southern peak (Figs. 5-11a & 5-11b). We brought up a possible scenario here from our observation that:

(1) The sub-horizontal strata in the E-W profile of the south peak allowed the seawater laterally migrated into the ridge (Figs. 4-24 & 5-11a), and cool down the temperature beneath the south peak directly.

(2) And also, there is a clear conduit under the southern peak acting as a pathway for upward fluid migration (Figs. 5-12), so if the seawater flows into the ridge from each side, it could migrate upward along the conduit to become a fluid cycle activity.

(3) There is another possible scenario to cause the same fluid cycle activity, if the conduit is a fluid release pathway to reduce the pressure inside of ridge; the cold seawater might be siphoned into the ridge automatically for preserving the hydraulic equilibrium.

(4) Furthermore, from the seismic image, the fluid flow here may not only focused within the vertical conduit (Figs. 4-25; 5-11), but also has a diffusive pattern along the ridge (Fig. 5-12). The temperature discrepancies are larger along the N-S profile compared with the E-W's, which we interpreted that there is more active horizontal fluid flows diffused in N-S direction along the long axis inside of the ridge. Under this scenario, the near horizontal ripple strata with plenty of the negative temperature discrepancies could support the cooling effect diffused along the N-S direction as well.

(5) Beside, in our steady-state model, we assumed the seafloor temperature is maintained at 3.48 °C not only at the ridge top but also on the flank, and the model temperatures eventually are higher at the core of the ridge, so and the fluid might be more buoyant to migrate upward. As a result, the cold seawater can flow sub-horizontally into the ridge from different depths of the strata to replenish the fluid flow under the ridge, and supply the vertical fluid flow successively.

These viewpoints are supporting the possibility of the cyclic cooling effect existing in the ridge, then influence the temperature filed of the ridge and produce a unique cold seep here. Therefore we could acquire such special chemoauttosynthesis-based community at cold seep in Formosa Ridge (Fig. 2-10). This is a specific example of canyon incision region with successive seawater cooling effect, but there might have some examples just related about the sedimentation or erosion to deposit or carry away the sediments then disturbed the temperature field directly, they are more common cases in small regions, that's why we can't slip our discussion in next section.

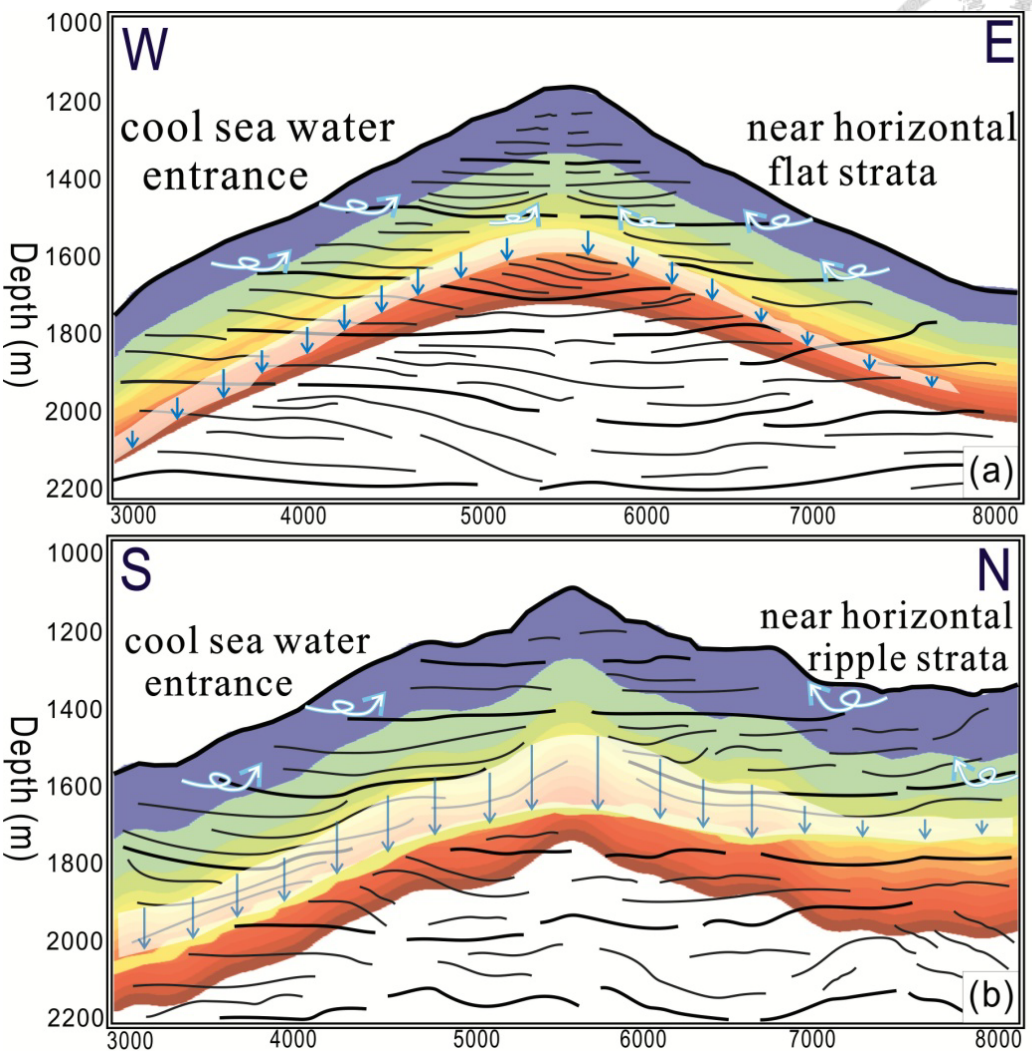

Figure 5-11 Combined with the interpreted structures and fluid migration patterns of the cold seep model in Formosa Ridge to support our possible scenario. (a) The conception model of the thermal pattern with the feature structures in W-E profile (b) The conception model of the thermal pattern with the feature structures in N-S profile.

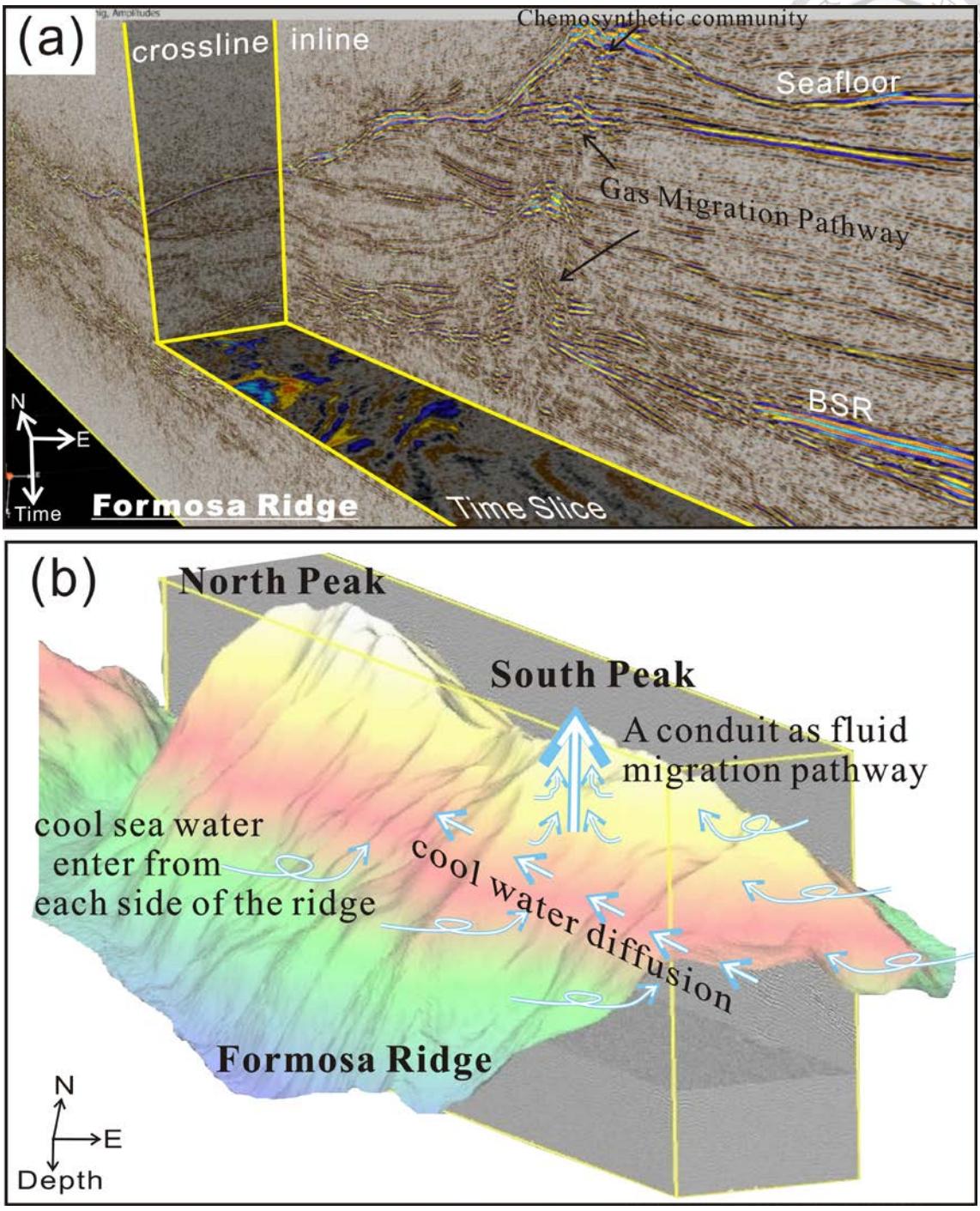

Figure 5-12 (a) The P-Cable 3-D seismic cube showed the conduit in the south peak of the Formosa Ridge; (b) We interpreted the conduit as a fluid migration pathway to allow the fluid upward migration, combined with the cool seawater supply in each side to become a cooling cycle, then horizontally diffuse the cooling effect in another direction to produce cold seep here.

5.3.4 Thermal Models of Sedimentation and Erosion

From previous analysis on the temperature discrepancies, we mentioned about the transient time on the temperature field of the MTD or thrust faulting processes. Actually, there are generally occurred in other places, such as the regional rapid sedimentation (Fig. 4-15b2), or rapid erosion in northwestern of the Yung-An Ridge (Fig. 5-2a) and Formosa Ridge (Figs. 4-24 & 4-25). Here we proposed two possible procedures to interpret their transition models.

Quick sedimentation events (Fig. 5-13) could destroy previous temperature equilibrium and justify the isotherms as the topography changed. After the sediments rapid deposited and created some sediment waves above the seafloor, BSR-based temperatures may need more time to catch up the changes of temperature filed, so we might discover the positive temperature discrepancies in the transient stage (Fig. 5-13b) from BSR-based to the model temperatures.

For quick erosion events (Fig. 5-14), such as the turbidity event could effectively take the surface sediments away, then the temperature would be modify to another new balancing isotherm to reflect the topography effect. As the P-T condition changed, the BSR-based temperatures start to catch up the modification of the temperature filed, so that we could find out some negative temperature discrepancies to indicate the cooling effect during the transient time (Fig. 5-14b).

Eventually, we could also apply the average thermal diffusivity on our regional model results to derive a rough time-scale for BSR-based temperatures restoring to equilibrium. The time period could be used in sedimentation and erosion cases, just aim to propagate and balance the heat after topography changed.

In heat transfer analysis, the thermal diffusivity is the thermal conductivity divided by density and specific heat capacity at constant pressure (Kadylak, et al., 2009). Here we used the diffusion rate of SiO_2 to indicate the rough diffusion rate of lithosphere (Holman, 2002) to derive the time period from following formula:

$$D = k/\rho c = L^2/T \quad \text{(Eq. 12)}$$

Where D is the thermal diffusivity rate = 8.3×10^{-7} (m^2/s); K is the thermal conductivity of rocks = 1.156 ($W/m^3 \cdot k$) (Shyu, 2006); ρ is the average density of lithosphere ~2700 (kg/m^3); c is the heat capacity = 516 (J/kgK). L is the diffusion depth in meters. Here we use the 300 mbsf (at the depth of BSR) as the sediment thickness to derive the transient period T in seconds:

$$T = (300)^2/(8.3\times10^{-7}) = 1.084\times10^{11}\,(s) = 3437\,(yrs) \quad \text{(Eq. 13)}$$

Then we found it need ~ 3400 years more to for restoring the temperature field at 300mbsf (the average subbottom depth of BSR offshore SW Taiwan). Such as that we need thirty more hundred years to balance the temperature field after the wave sediment waves occurred in lower Fangliao basin (Fig. 5-14b). But if there are some fluid contain in the sediments, the transient time might be longer than 3400 years because of the smaller thermal diffusivity rate.

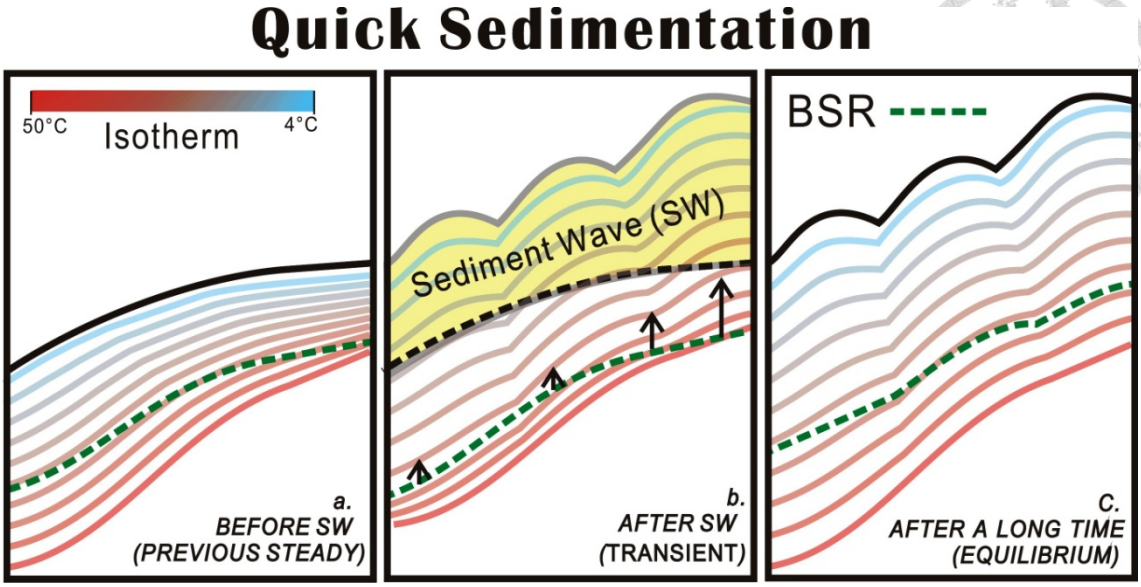

Figure 5-13 We used the isotherms evolution to show the influence of the temperature field during a quick sedimentation event (e.g. sedimentation wave; SW): (a) BSR-based temperatures are equilibrium to consistent with the model ones. (b) The rapid SW leaded the model temperatures change as the topography changed, but BSR-based temperatures are in transition period to show the heating effect at BSR depth. (c) The temperature field is restored to the equilibrium again.

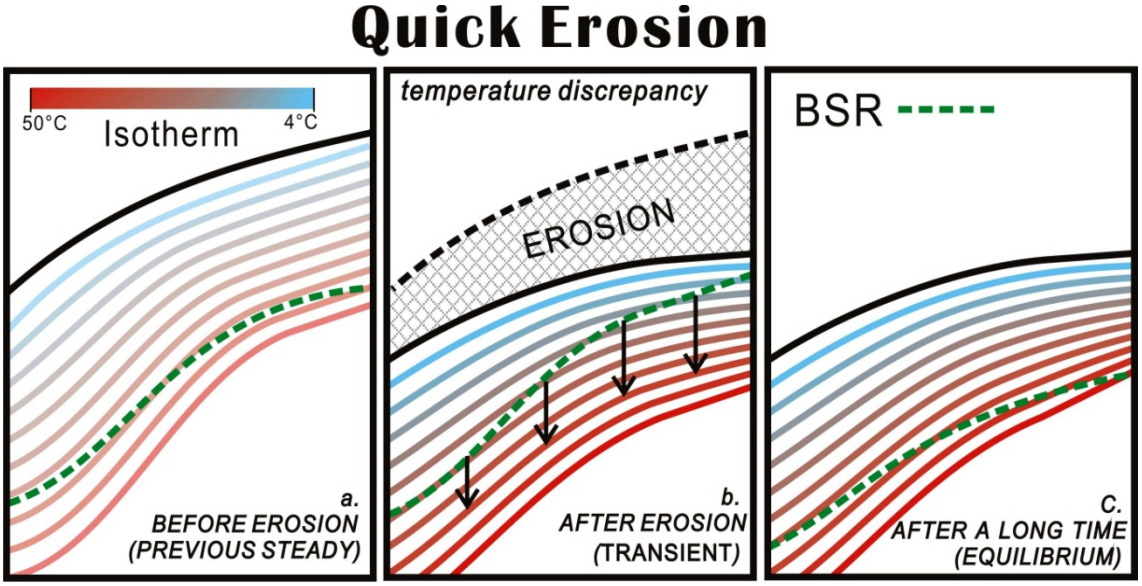

Figure 5-14 We used the isotherms evolution to show the influence of the temperature field during a quick erosion event (e.g. turbidity). (a) BSR-based temperatures are equilibrium to consistent with the model ones. (b) Quick erosion event leaded the model temperatures change as the topography changed, but BSR-based temperatures are in transition period to show cooling effect at BSR depth. (c) The temperature field is restored to the equilibrium again.

Chapter 6: Conclusion

In this study, we took advantages on BSR-based temperatures from the seismic data, to propose two special methods for analyzing the regional thermal patterns. This is the first time that applying the Péclet Number on BSR-based temperatures to derive regional 1-D fluid flow rates on different regions; and it's also the unprecedented examination that comparing BSR-based temperature fields with conductive temperature fields from Pecube to discuss the thermal structures in 2-D profiles and 3-D cubes.

After analyzing our study results, we derived several geological processes which are relating to the seafloor thermal structures offshore SW Taiwan, to interpret our observations on temperature fields:

(1) Regarding the regional topography effect, which is the most important effect of studying the thermal structures, in our study, we have successfully corrected them from considering the temperature discrepancies as the regional cooling and heating effects, instead of using the model or BSR-based temperature fields only.

(2) Along and near Manila Trench, there are higher fluid flow rates (24 cm/y) when the frontal thrust climbs onto the continental slope of the passive margin in the collision zone (Fig. 3-6). It might because the porosity changes dramatically after the incoming sediments incorporated into the active margin, then the fluid in the pore space physically upward migrate to the seafloor.

We then studied two 3-D temperature cubes for detail analysis: One is related to the MTD effect occurred in upper reach of the Penghu Canyon with the highest vertical fluid flow rate (~ 43 cm/y at J site), it cause the heating and cooling effects at the uphill and downhill respectively (Figs. 4-8 & 5-10); another one is in Frontal Ridge, which is discovered the possible extensive fluid migration from the thrust faulting pathways to cause the heating effect at the toe of the accretionary wedge (Figs. 4-11 & 5-7).

(3) From passive to active margin, the increasing of fluid flow rate (13 to 21 cm/y) might be related to active dewatering near the toe of the trench (Fig. 3-7). In the lower slope domain, such dewatering process is active, thus the slightly higher fluid flow rates (A, B, H, I sites of Fig. 3-8). However, in the upper slope domain, where the compactly dewatering process may decrease the porosity in sediments, as the reasons of the difficult imaged and penetrated sediments by seismic waves and samples in this region.

Moreover, from studying the 3-D cube in Yung-An Ridge of the lower slope domain, we found intermittent upward fluid migrations along the fault planes brought about the heating effects (Figs. 5-2 & 5-8); relatively, from studying the 3-D cube in lower Fangliao Canyon of the upper slope domain, we discovered the regional heating effect from the diapir was reduced 38 % by recent sedimentation (Fig. 5-9).

(4) Besides, from studying the 3-D cube in Formosa Ridge of the passive margin, we particularly proposed a 3-D thermal structure (Fig. 5-12b) to interpret the seismic

and geochemical discoveries recently. Our model supported that the cold seawater had been laterally siphoned into the ridge in the traverse direction (Figs. 4-24 & 5-11a), and diffused along the ridge strike to disturb the temperature fields (Fig. 4-25 & 5-11b).

However, the results from our simulation are still need to improved for better parameters control, we understand that our qualitative results will be updated to quantitative ones after obtaining more accurate physical parameters from drilling data, then we could modify our boundary conditions as well, that's also the reason why we tried to keep conservative on our temperature discrepancies. Therefore our contributions were more close to develop a preliminary simulation for better using our current data to analyze the approximate results on thermal structures offshore SW Taiwan.

In the future, we could improve our simulations for better modeling controls at smaller scales, such as deriving the thermal diffusion rate after acquiring the dating results of the MTD region, or estimating the fluid flux produced from the thrust faulting or diapir, then carry out the possible methane flux come along the regional structures, which is an important information for gas hydrate research. On the contrary, we could apply the technique on potential thermal structures in a large scale as well, then consider about the heat capacities or entropy to infer the possible stress accumulations, it might be help for predicting some possible natural disasters in specific regions. But anyhow, it's definitely necessary to have the preliminary studies as we've done in this study.

References

Anderson, K. E., Havenstein, G. B., and Brake, J., 1995. Effects of Strain and Rearin Dietary Regimenson Brown-Egg Pulled Growt and Strain, Rearing Dietary egimens: *Density and Feeder Space Effects on Subsequent Laying Performance*. **74**, 1079-1092

Ashi, J., and Taira, A., 1993. Thermal structure of the Nankai accretionary prism as inferred from the distribution of gas hydrate BSRs, in Underwood MB (Ed). Thermal evolution of the Tertiary Shimanto Belt, Southwest Japan: an example of ridge-trench interaction: *Special Paper - Geology Society of America*, **273**, 137–149

Baba, K., and Yamada, Y., BSRs and associated reflections as an indicator of gas hydrate and free gas accumulation: An example of accretionary prism and forearc basin system along the Nankai Trough, off central Japan, Resource Geology, **54(1)**, 11-24, 2004.

Bagirov, E., and Lerche, I., 1999. *Impact of natural hazards on oil and gas extraction: the South Caspian basin*. Springer, pp. 290.

Bathe, K. J., 1982. *Finite Element Procedures in Engineering Analysis*: 1st Edition. Prentice-Hall, Englewood Cliffs, NJ, pp. 735.

Beardsmore, G. R., and Cull, J. P., 2001. *Crustal Heat Flow: A Guide to Measurement and Modeling*: Cambridge University Press, pp. 324.

Braun, J., and Van Der Beek, P., 2004. Evolution of passive margin escarpments: What can we learn from low-temperature thermo chronology: *Journal of Geophysical Research*, **109(F4)**, F04009.

Braun, J., 2003. Pecube: A new finite-element code to solve the 3D heat transport equation including the effects of a time-varying: finite amplitude surface topography: *Computers & Geosciences*, **29(6)**, 787-794.

Bray, C. J., and Karig, D. E., 1985. Porosity of sediments in accretionary prisms and some implications for dewatering processes: *Journal of Geophysical Research*, **90**, 768-778.

Bredoehoeft, J. D., and Papadopulos, I. S., 1965. Rates of vertical groundwater movement estimated from the earth's thermal profile: *Water Resources Research*, **1**, 325-328.

Brown, K. M., Bangs, N. L., Froelich, N., Kvenvolden, K. A., 1996. The nature, distribution, and origin of gas hydrate in the Chile Triple Junction region: *Earth Planet Society Letter*, **139**, 471 483.

Brown, K. M., and Westbrook, G. K., 1988. Mud diapirism and subcretion in the Barbados Ridge accretionary complex: the role of fluids in accretionary processes, *Tectonics*, **7(3)**, 613-640.

Carslaw, H. S., and Jaeger, C. J., 1959. *Conduction of Heat in Solids*, 3rd Edition: Clarendon Press, Oxford, pp. 510.

Chang, H. I., Shyu, C. T., 2011. Compact high-resolution temperature loggers for measure the thermal gradients of marine sediments: *Marine Geophysical Research*, **32**, 465-478.

Chen, L., Chi, W. C., Lu, C, Y., 2011. Estimating 1D Vertical Fluid Migration Rates in Shallow Marine Sediments Using Bottom-Simulating Reflectors: *West Pacific Earth Science*, **11**, 103-114.

Chen, L., Chi, W. C., Liu. C. S., Shyu, C. T., Wang, Y. S., Wang, Lu, C. Y., 2012. Deriving Regional Vertical Fluid Migration Rates Offshore Southwestern Taiwan Using Bottom-Simulating Reflectors: *Marine Geophysical Research*, **33(4)**, 379-388.

Chen, L., Chi, W. C., We, S. K., Liu, C. S., Shyu, C. T., Wang, W. S., Lu, C. Y., 2014. Two dimensional fluid flow models at two gas hydrate sites offshore southwestern Taiwan: *Journal of Asian Earth Sciences* (in press).

Chen, S. C., Hsu, S. K., Wang, Y., Tsai, C. H., 2013. Active mud volcanoes and potential gas hydrate in the upper Kaoping slope offshore SW Taiwan (in Chinese with English abstract): *Mining & Metallurgy*, **219**, 73-88.

Chen, S. C., 2013a. Distribution of the mud diapirs, mud volcanoes and related seafloor features in the Kaoping slope off southwest Taiwan (in Chinese with English abstract) : *PhD dissertation of National Central University, Taiwan.* pp. 132.

Chi, W. C., Reed, D. L., Lundberg, N., and Liu, C. S., 1998. Distribution of the bottom simulating reflector in the offshore Taiwan collision zone: *Terrestrial, Atmospheric and Oceanic Sciences*, **9(4)**, 779-794.

Chi, W. C., Reed, D. L., and Tsai, C. C., 2006. Gas hydrate stability zone offshore southern Taiwan: Terrestrial, *Atmospheric and Oceanic Sciences*, **17(4)**, 829-843.

Chi, W. C., Reed, D. L., 2008. Evolution of shallow crustal thermal structure from subduction to collision: an example from Taiwan: Bulletin Geological Society of America, 120(5/6), 679-690Schnürle, P., Liu, C. S., 2011. Numerical modeling of gas hydrates emplacements in oceanic sediments: *Marine and Petroleum Geology*, **28(10)**, 1856-1869.

Chiang, C. S., Yu, H. S., and Chou, Y. W., 2004. Characteristics of the wedge-top depozone of the southern Taiwan foreland basin system: *Basin Research*, **16**, 65-78.

Chuang, C., Yang, T. F., Lin, S., Lee, H.F., Lan, T. F., Hong, W. L., Liu, C. S., Chen, J. C. and Wang, Y., 2006. Extremely high methane concentration in bottom water and cored samples from offshore southwestern Taiwan: *Terrestrial, Atmospheric and Oceanic Sciences*, **17(4)**, 903-920.

Cloetingh, S., Wess, J. D. v. et al., 2010. Lithosphere tectonics and thermo-mechanical

properties: An integrated modeling approach for Enhanced Geothermal Systems exploration in Europe: *Earth-Science Reviews*, **102 (3)**, 159-206.

Claypool, G. E., and Kaplan, I. R., 1974, the origin and distribute of methane in marine sediments: *Nature Gases in Marine Sediments*, 99-139.

Davis, E. E., Hyndman, R. D., Villinger, H., 1990. Rates of fluid expulsion across the northern Cascadia accretionary prism: constraints from new heat flow and multichannel seismic reflection data: *Journal of Geophysical Research*, **95**, 8869-8889.

Ganguly, N., Spence, G. D., Chapman, N. R., and Hyndman, R. D., 2000, Heat flow variations from bottom simulating reflectors on the Cascadia margin: *Marine Geology*, **164(1-2)**, 53-68.

Han, W. C., Liu, C. S., Lin, A. T., Lin, C. C., Hsu, H. H., Ko, C. C., Chen, S. C., Chung, S. H., Wang, Y. S., 2012. Structural Features and Gas Hydrate Distribution Across the Boundary of the Submarine Taiwan Accretionary Wedge and Passive China Continental Margin Offshore Southwestern Taiwan *in 2012 Fall Meeting AGU, San Francisco, Calf.* Abstract # OS34A-02.

Hirtzel, J, Chi, W. C., Reed, D., Chen, L. W., Liu, C. S., and Lundberg, N., 2009. Destruction of Luzon forearc basin from subduction to Taiwan arc-continent collision: *Tectonophysics*, **325**, 23-42.

Hornbach, M. J., Nathan L. Bangs, and Berndt, C., 2012. Detecting hydrate and fluid flow from bottom simulating reflector depth anomalies: *Geology*, **40(3)**, 227-230.

Horng, C. S., 2013. Investigation of Gas Hydrate Resource Potential: Seismic, Heat Flow and Geochemical Studies (2/4) – magnetic properties of sediments off southwestern Taiwan, the annual generation of research and microfossils: *Report of Central Geological Survey 2012*, **102-19-H**, pp. 71.

Huang, C. Y., Wu, W. Y., Chang, C. P., Tsao, S., Yuan, B., Lin, C. W., and Xia, K. Y., 1997. Tectonic evolution of accretionary prism in the arc-continent collision terrane of Taiwan: *Tectonophysics*, **281**, 31-51.

Huang, S. T., Yang, K. M., Hung, J. H., Wu, J. C., Ting, H. H., Mei, W. W., Hsu, S. H., Lee, M., 2004. Deformation front development at the northeast margin of the Tainan basin, Tainan-Kaohsiung area: Taiwan: *Marine Geophysical Research*, **25**, 139-156.

Holman, J. P., 2002. Heat Transfer (9th ed.): McGraw-Hill. ISBN 0070296391. 736p

Hyndman, R. D., Davis, E. E., 1992. A mechanism for the formation of methane hydrate and seafloor bottom simulating reflectors by vertical fluid expulsion: *Journal of Geophysical Research*, **97**, 910–924.

Hyndman, R. D., Davis, E. E., Wright, J. A., 1979. The measurement of marine geothermal heat flow by a multi-penetration probe with digital acoustic telemetry

and in situ thermal conductivity: *Marine Geophysical Research*, **4**, 181-205.

Kadylak, D, Peter, C., and Walter M., 2009. Effectiveness correlations for heat and mass transfer in membrane humidifiers. *International Journal of Heat and Mass Transfer*, **52 (5)**, 1504-1509.

Kaul, N., Rosenberger, A., and Villinger, H., 2000, Comparison of measured and BSR-derived heat flow values, Makran accretionary prism, Pakistan: *Marine Geology*, **164 (1-2)**, 37-51.

Kinoshita, M., Moore, G. F., and Kido, Y. N., 2011. Heat flow estimated from BSR and IODP borehole data: Implication of recent uplift and erosion of the imbricate thrust zone in the Nankai Trough off Kumano. *Geochemistry, Geophysics, Geosystems*, **12(9)**, 1-18.

Kvenvolden, K. A., and McMenamin, M. A., 1980. Hydrates of natural gas: A review of their geologic occurrence: *US Geological Survey Circular*, **825**, 1–11.

Lai, M. C., Ding J. Y., Wu, S. Y., Hung, C. C., Lai, S. J., Lin, S, Yang, T. F., 2009. Archaeal and bacterial diversity and distribution in methane seep of Yung-An Ridge, SW Taiwan: *Geochimica et Cosmochimica Acta*, **73(13)**, pp. 714.

Lai, M. C., 2011. New resource offshore southwestern Taiwan- natural gas hydrates resources survey and evaluation of geochemical research (4/4) - The investigations of geological microorganisms biodiversity (bacteria and Pacific Biological) and the gas hydrate formation and decomposition mechanisms: *Report of Central Geological Survey 2011*, **100-25-B**, pp. 88.

Lee, S. H., 2008. The Base of Gas Hydrate Stability Zone and the Anomalous Sediment Thermal Conductivity Offshore of SW Taiwan (in Chinese with English abstract). *Master thesis of National Taiwan University*, pp. 60.

Lin, S., Lim, Y., Liu, L.S, Yang, T.F., Chen, Y.G. Machiyama, H., Soh, H.W. Fujikura, K. Wang, Y. Chung, S., 2007. Formosa Ridge, A cold fluid flow with densely populated chemosynthetic community in the passive margin, southwest of Taiwan. *in Proceedings of the International Conference on Gas Hydrates: Energy, Climate and Environment, Taipei, Taiwan,* October 4-5, 2007.

Lin, A. T., Liu, C. S., Lin, C. C., Schnürle, P., Chen, G. Y., Liao, W. Z., Teng, L. S., Chuang, H. J., and Wu, M. S., 2008. Tectonic features associated with the overriding of an accretionary wedge on top of a rifted continental margin: an example from Taiwan: *Marine geology*, **255**, 186-203.

Lin, A. T., Yao, B., Hsu, S. K., Liu, C. S., Huang, C. Y., 2009. Tectonic features of the incipient arc-continent collision zone of Taiwan: Implications for seismicity: *Tectonophysics*, **479**, 28-42.

Lin, C. C., Lin, A. T. S., Liu, C. S., Chen, G. Y., Liao, W. Z., and Schnürle, P., 2009a, Geological controls on BSR occurrences in the incipient arc-continent collision

zone off southwest Taiwan: *Marine and Petroleum Geology*, **26**, 1118-1131.

Lin, S., 2011. New resource offshore southwestern Taiwan- natural gas hydrates resources survey and evaluation of geochemical research (4/4) – Geophysical survey and investigation: *Report of Central Geological Survey 2011*, **100-25**, pp. 138.

Lin, C. C., 2012. Geological controls of gas hydrate occurrences and gas hydrate resource assessment, offshore southwest Taiwan: *PhD dissertation of National Central University, Taiwan*. pp. 219.

Lin, L. F., Liu, C. S., Lin, C. C., Hsu, H. H., Chen, S. C., Chung, S. H., Wang, Y. S., 2012a. Gas hydrate potential in the Frontal Ridge Offshore SW Taiwan from 3D seismic investigation *in 2012 Fall Meeting AGU, San Francisco, Calf.* Abstract # OS34A-03.

Lin, C. C., Lin, A. T. S., Liu, C. S., Horng, C. S., Chen, G. Y., and Wang, Y., 2013. Canyon-infilling and gas hydrate occurrences in the frontal fold of the offshore accretionary wedge off southern Taiwan: *Marine Geophysical Research*, **35(1)**, 21-35.

Lister, C. R. B., 1979. The pulse-probe method of conductivity measurement: *Geophysics journal research abstract society*, **57,** 451–461.

Liu, C. S., Huang, I. L., and Teng, L. S., 1997. Structural features off southwestern Taiwan: *Marine Geology*, **137**, 305-319.

Liu, C. S., Schnürle, P., Wang, Y., Chung, S. H., Chen, S. C., and Hsiuan, T. H., 2006. Distribution and characters of gas hydrate offshore southwestern Taiwan: *Terrestrial, Atmospheric and Oceanic Sciences*, **17(4)**, 615-644.

Liu, C. S., 2009. New energy resource offshore southwest Taiwan – exploration and evaluation of gas hydrate resource: seismic and geotherm investigation (2/4): *Report of Central Geological Survey 2009*, **98-25-A**, pp. 100.

Liu, C. S., 2011. New energy resource offshore southwest Taiwan – exploration and evaluation of gas hydrate resource: seismic and geotherm investigation (4/4): *Report of Central Geological Survey 2011*, **100-24**, pp. 232.

Liu, C. S., 2012. Investigation of Gas Hydrate Resource Potential: Seismic, Heat Flow and Geochemical Studies (1/4) – reflection seismic and chirp sonar exploration study: *Report of Central Geological Survey 2012*, **101-22-A**, pp. 135.

Liu, C. S., Hsu, H. H., Morita, S., Tu, S. L., Ko, C. C., Lin, S, Machiyama, H., Soh, W., 2013, Seismic imaging of a cold seep site offshore southwestern Taiwan: *Journal of Asian Earth Sciences* (submitted).

Liu, C. S., 2013. Investigation of Gas Hydrate Resource Potential: Seismic, Heat Flow and Geochemical Studies (2/4) – reflection seismic and chirp sonar exploration study: *Report of Central Geological Survey 2013*, **102-19-A**, pp. 201.

McIntosh, K., Nakamura, Y., Wang, T. K., Shih, R. C., Chen, A., Liu, C. S., 2005. Crustal-scale seismic profiles across Taiwan and the western Philippine Sea: *Tectonophysics*, **401**, 23-54.

Minshull, T., White, R., 1989. Sediment compaction and fluid migration in the Makran accretionary prism: *Journal of Geophysical Research*, **94**, 7387–7402.

Moore, J. C., and Vrolijk, P., 1992. Fluids in accretionary prisms. *Reviews of Geophysics*, **30(2)**, 113-135.

Patankar, S. V., 1980. *Numerical heat transfer and fluid flow: Computational methods in mechanics and thermal science.* Washington DC, Hemisphere Publishing Corportion 1980, pp. 214.

Paul, C. K., Ussler, W. and Borowski, W. S., 1994. Sources of biogenic methane to form marine gas hydrates: *International Conference on Natural Gas Hydrates*, 392–409.

Peng, Y. S., 2012. The effect of heat flow on the base of gas hydrate stability zone in the Yung-An Ridge offshore southwestern Taiwan (in Chinese with English abstract): *Master thesis of National Taiwan University*, Taiwan, pp. 89.

Pfender, M., Villinger, H., 2002. Miniaturized data loggers for deep sea sediment temperature gradient measurements: *Marine Geology*, **186**, 557-570.

Reed, D. L., Lundberg, N., Liu, C. S., and Kuo, B.T., 1992. Structural relations along the margin of the offshore Taiwan accretionary wedge: Implications for accretion and crustal kinematics:. *Acta Oceanographica Taiwanica*, **30**, 105-122.

Reed, D. L., Lundberg, N., Liu, C. S., McIntosh, K. D., Lieske, J. H., and Kuo, B. Y., 1991, Strain domains, fluid/gas migration, and proto thrusting in the offshore Taiwan accretionary wedge: *Geological Society of America Abstracts with Programs*, **23**, pp. 365.

Schnürle, P., Liu, C. S., Hsiuan, T. H., and Wang, T. K., 2004. Characteristics of gas hydrate and free gas offshore southwestern Taiwan from a combined MCS/OBS data analysis: *Marine Geophysical Research*, **25**, 157-180.

Schnuerle, P., Liu, C. S., 2011. Numerical modeling of gas hydrate emplacements in oceanic sediments, *Marine and Petroleum Geology*, **28(10)**, 1856-1869.

Shipley, T. H., Houston, M. H., Buffler, R. T., Shaub, F. J., McMillen, K. J., Ladd, J. W., Worzel, J. L., 1979. Seismic evidence for widespread possible gas hydrate horizons on continental slopes and rises: *American Association of Petroleum Geologists*, **63**, 2204– 2213.

Shipley, T. H., Moore, G. F., Bangs, N. L., Moore, J. C, Stoffa, L., 1994. Seismically inferred dilatancy distribution, northern Barbados Ridge décollement: implications for fluid migration and fault strength: *Geology*, **22**, 411–414.

Shyu, C. T., Hsu, S. S., Liu, C. 1998. Heat flow off southwest Taiwan: measurements over mud diapirs and estimated from bottom simulating reflectors: *Terrestrial*,

Atmospheric and Oceanic Sciences, **9**, 795–812.

Shyu, C. T., Chang, H. I., 2005. Determination of seafloor temperature using data from high-resolution marine heat probes: *Terrestrial, Atmospheric and Oceanic Sciences*, **16**, 137–153.

Shyu, C. T., Chen, Y. J., Chiang, S. T., and Liu, C.S., 2006. Heat flow measurements over bottom simulating reflectors offshore southwestern Taiwan: *Terrestrial, Atmospheric and Oceanic Sciences*, **17**, 845-869.

Shyu, C. T., 2013. New energy resource offshore southwest Taiwan – exploration and evaluation of gas hydrate resource: seismic and geotherm investigation (2/4) – reflection seismic and chirp sonar exploration study: *Report of Central Geological Survey 2013,* **102-19-D**, pp. 75.

Suess, E. et al.,1988. Ocean Drilling Program Leg 112, Peru continental margin, Part 2, *sedimentary history and digenesis in a coastal upwelling environment: Geology*, **16**, 939-943.

Sun, S.C., Liu, C.S., 1993. Mud diapirs and submarine channel deposits in offshore Kaohsiung–Hengchun, southwest Taiwan: Petroleum Geology of Taiwan, 28, 1-14.

Townend, J., 1997. Estimates of conductive heat flow through bottom-simulating reflectors on the Hikurangi and southwest Fiordland continental margins: New Zealand: *Marine Geology*, **141**, 209–220.

Tsai, Y. T., 2010, Using P wave Velocity to Correct Geothermal Gradient and Base of Gas Hydrate Stability Zone (in Chinese with English abstract): *Master thesis of National Taiwan University*, pp. 85.

Tu, S. L., 2010, Using Pre-stack Depth Migration Technique to Analyze the Characteristics and Saturation of Gas Hydrate Offshore Southwestern Taiwan (in Chinese with English abstract). *Master thesis of National Taiwan University*, pp. 90.

Tucholke, B.E., Byran, G.M., and Ewing, J.I., 1977, Gas hydrate horizons detected in seismic-profiles data from the western Northern Atlantic: *The American Association of Petroleum Geologists Bulletin*, **61**, 698–707.

Villinger, H., Tréhu, A., and Grevemeyer, I., 2010. Seafloor Marine Heat Flux Measurements and Estimation of Heat Flux from Seismic Observations of Bottom Simulating Reflectors: Geophysical Characterization of Gas Hydrates, *Society of Exploration Geophysicists*, 279-300.

Vrolijk, P., Fisher, A., and Gieskes, A., 1991. Geochemica1 and Geothermal evidence for fluid migration in the Barbado asccretionary prism (ODP Leg 110), *Geophysical Resarch Letters*, **18**, 947-950.

Von Herzen, R. P., Cordery, M. J., Detrick, R. S., & Fang, C., 1989. Heat flow and the thermal origin of hot spot swells: The Hawaiian swell revisited. *Journal of*

Geophysical Research: Solid Earth, **94(B10)**, 13783-13799.

Von Herzen, R. P., Maxwell, A. E., 1959. The measurement of thermal conductivity of deep-sea sediments by a needle-probe method: *Journal of Geophysical Research*, **64**, 1557–1563.

Yamano, M., Uyeda, S., Aoki, Y., Shipley, T. H., 1982. Estimates of heat flow derived from gas hydrates: *Geology*, 10, 339-343.

Yan, P., Zhou, D., Liu, Z. S., 2001. A crustal structure profile across the northern continental margin of the South China Sea. Tectonophysics, 338, 1–21.

Yang, T. F., Yeh, G. H., Fu, C. C., Wang, C. C., Lan, T. F., Lee, H. F., Chen, C. H., Walia, and Sung, Q. C., 2004. Composition and exhalation flux of gases from mud volcanoes in Taiwan: *Environmental Geology*, **46**, 1003-1011.

Yang T. F., Chuang C., Lin, S., Chen, J. C., Wang, Y, Chung, S. H., 2006. Methane venting in gas hydrate potential area offshore of SW Taiwan: evidence of gas analysis of water column samples: *Terrestrial, Atmospheric and Oceanic Sciences*, **17**, 933-950.

Yang, T. F., 2011, New energy resource offshore southwest Taiwan - natural gas hydrates resources survey and evaluation of geochemical research (4/4) - reflection seismic and chirp sonar exploration study: *Report of Central Geological Survey 2011*, **101-22-F,** 113 pp.

Yang, T. F., 2012, Investigation of Gas Hydrate Resource Potential: Seismic, Heat Flow and Geochemical Studies (1/4) – gas composition of bottom water and sediments offshore southwest Taiwan: *Report of Central Geological Survey 2012*, **101-22-F**, 113 pp.

Yu H.S., 2004. An under-filled foreland basin in the northern South China Sea off Southwest Taiwan: incipient collision and foreland sedimentation. In: Clift P et al (eds.), Continent-Ocean Interactions within East Asian Marginal Seas, *Geophysical Monograph Series*, **149**: 348 pp.

Wang, T. K., Chen, M. K., Lee, C. S., Xia, K. Y., 2006. Seismic imaging of the transitional crust across the northeastern margin of the South China Sea: *Tectonophysics*, **412**, 237-254.

Zeitler, K., Herczig, A. L., McDougall, I., Honda, M., 1987. U–Th–He dating of apatite: a potential thermochronometer: **Geochemica et Cosmochemica Acta**, **51**, 2865–2868.

Zienkiewicz, O.C., 1977. The Finite Element Method, 3rd Edition: McGraw-Hill, *Maidenhead, England*, 787.

Zwart, G., and Moore, J. C., 1993. Variations in temperature gradient of the Oregon accretionary prism: *EOS*, **74**, 222.